

# Study on Laser Cleaving Mechanism of Brittle Materials

メタデータ	言語: eng 出版者: 公開日: 2017-10-05 キーワード (Ja): キーワード (En): 作成者: メールアドレス: 所属:
URL	<a href="http://hdl.handle.net/2297/42345">http://hdl.handle.net/2297/42345</a>

This work is licensed under a Creative Commons Attribution-NonCommercial-ShareAlike 3.0 International License.



Dissertation

**STUDY ON THE LASER CLEAVING MECHANISM OF  
BRITTLE MATERIALS**

レーザによる硬脆材料の割断メカニズムに関する研究

Graduate School of Natural Science & Technology  
Kanazawa University

Division of Innovative Technology and Science  
System Design and Planning

Student ID Number	: 1223122002
Name	: Alias bin Mohd Saman
Chief advisor	: Assoc. Prof. Tatsuaki Furumoto
Date of Submission	: March 2015

## TABLE OF CONTENT

CHAPTER 1 : INTRODUCTION.....	1
1.1 RESEARCH OBJECTIVES .....	5
1.2 THESIS OUTLINE .....	6
REFERENCES .....	7
CHAPTER 2 : OVERVIEW OF LASER CUTTING AND THERMAL-STRESS CLEAVING .....	9
2.1 INTRODUCTION .....	9
2.2 LASER CUTTING METHODS.....	10
2.2.1 Evaporative laser cutting.....	11
2.2.2 Laser melting and blow .....	12
2.2.4 Laser cleaving .....	12
2.3 SEPARATION METHODS OF WAFER (BRITTLE) MATERIALS .....	13
2.3.1 Mechanical dicing.....	13
2.3.2 Diamond scribing and snapping.....	15
2.3.3 Laser scribing and snapping.....	16
2.3.4 Laser full cut .....	16
2.3.5 Stealth dicing .....	17
2.3.6 Thermal stress cleaving.....	18
2.4 BASIC PRINCIPLES OF THERMAL-STRESS CLEAVING.....	19
2.5 PREVIOUS RESEARCH.....	21
2.6 CONCLUSIONS .....	25
REFERENCES .....	26
CHAPTER 3 : MICRO-GROOVE FABRICATION BY USING A MICRO-LENS.....	29
3.1 INTRODUCTION .....	29
3.2 DEVELOPMENT OF MICRO LENS.....	30
3.2.1 Micro-lens material.....	31
3.2.2 Optical properties.....	33
3.2.3 Micro-lens fabrication method.....	33
3.2.3 Micro lens shape .....	35
3.3 MICRO-GROOVE PROCESSING.....	36

## TABLE OF CONTENT

---

3.3.1	Experiment methodology .....	37
3.3.2	Results and discussion .....	40
3.4	CONCLUSIONS .....	43
	REFERENCES .....	44
CHAPTER 4 : BASIC PRINCIPLE AND CALIBRATION OF TWO-COLOR PYROMETER .....		45
4.1	INTRODUCTION .....	45
4.2	THERMAL RADIATION.....	46
4.3	FUNDAMENTAL OF TWO-COLOR PYROMETER.....	50
4.4	TWO-COLOR PYROMETER’S COMPONENTS .....	51
4.4.1	Optical fiber .....	51
4.4.2	Infrared detector.....	55
4.4.3	Amplifier.....	57
4.4.4	Condenser lens .....	59
4.4.5	Relative sensitivity of two-color pyrometer.....	59
4.5	CALIBRATION .....	61
4.6	CONCLUSIONS .....	64
	REFERENCES .....	65
CHAPTER 5 : INVESTIGATION OF THERMAL-STRESS CLEAVING WITH SINGLE- POINT LASER .....		66
5.1	INTRODUCTION .....	66
5.2	EXPERIMENTAL METHODOLOGY.....	67
5.2.1	Preparation of silicon-wafer specimen.....	67
5.2.2	Experimental procedure .....	68
5.3	EXPERIMENTAL RESULTS AND DISCUSSION .....	72
5.3.1	Output signal from the pyrometer and AE sensor .....	72
5.3.2	Temperature measurement.....	74
5.3.3	Cleaving time .....	77
5.3.4	The influence of laser position on fracture extension.....	79
5.4	FINITE-ELEMENT ANALYSIS .....	81
5.4.1	Absorption characteristic .....	81
5.4.2	Basic assumption on boundary conditions and material properties.....	82
5.4.3	FEM analysis result.....	87
5.5	CONCLUSIONS .....	95

---

## TABLE OF CONTENT

---

REFERENCES .....	96
CHAPTER 6 : INVESTIGATION OF THERMAL-STRESS CLEAVING WITH MOVING LASER.....	97
6.1 INTRODUCTION .....	97
6.2 EXPERIMENTAL METHODOLOGY.....	98
6.2.1 Silicon-wafer specimen.....	98
6.2.2 Experimental procedure .....	101
6.3 EXPERIMENTAL RESULTS AND DISCUSSION .....	104
6.3.1 Temperature measurement.....	103
6.3.2 Acoustic-emission (AE) signal measurement.....	107
6.3.3 Cleaving surface observation.....	110
6.3.4 Influence of groove length and depth .....	115
6.4 FINITE-ELEMENT ANALYSIS .....	117
6.4.1 Temperature and thermal-stress distributions.....	119
6.4.2 The influence of groove length .....	121
6.4.3 The influence of groove depth .....	123
6.5 STRESS INTENSITY FACTOR .....	125
6.5.1 Determining stress intensity factor using FEM .....	126
6.6 COMPARISON BETWEEN THE FRACTURE INITIATION TIMES OF FEM AND EXPERIMENTAL RESULTS.....	130
6.7 DETERMINATION OF FRACTURE TOUGHNESS .....	131
6.8 SEPARATING MECHANISM OF SILICON WAFER.....	135
6.9 CONCLUSIONS .....	137
REFERENCES .....	139
CHAPTER 7 : INVESTIGATION OF LASER CLEAVING OF SAPPHIRE WAFER BY CO2 LASER .....	140
7.1 INTRODUCTION .....	140
7.2 MATERIAL PROPERTIES .....	141
7.3 LASER ENERGY ABSORPTION CHARACTERISTIC .....	143
7.4 FINITE-ELEMENT ANALYSIS .....	146
7.4.1 Temperature distribution.....	148
7.4.2 Thermal-stress distribution .....	150
7.4.3 Stress intensity factor .....	155

---

## TABLE OF CONTENT

---

7.5	COMPARISON BETWEEN THE LASER CLEAVING MECHANISMS OF SAPPHIRE AND SILICON WAFER .....	158
7.6	CONCLUSIONS .....	160
	REFERENCES .....	161
CHAPTER 8 : CONCLUSIONS .....		162
LIST OF PUBLICATIONS .....		166
ACKNOWLEDGEMENTS .....		167

## ACKNOWLEDGEMENT

---

## CHAPTER 1 : INTRODUCTION

Laser cutting using a thermal-stress cleaving technique has great potential for separating brittle materials such as silicon and sapphire wafers. In this method, thermal stress is used to induce a crack that causes the material to split along the cutting path of the laser beam. As a non-contact process, the laser cleaving technique is becoming an essential solution for separating thin wafers, which are susceptible to unnecessary force exerted by cutting tools and clamping devices.

Thin silicon wafer is ideal for products that require mechanical flexibility, such as bendable smart cards, chips in paper, and contactless labels. It offers a variety of new possibilities in the micro-electronics, solar cell and micro-mechanical industries, such as three-dimensional integration of stacked dies, thin micro-electro-mechanical packages, and thin single-crystalline solar cells [1]. Demand for sapphire wafer is also increasing for products that require more advanced mechanical properties, such as transistors and diodes for power amplifier circuits, mobile phones and household appliances. The use of thinner wafer in silicon-based products has become common recently. The drive to succeed in today's silicon-based industry has led to significant reduction of silicon-wafer thickness down to 50 microns or less [2]. Therefore, the micro-machining of wafer materials has become a critical issue.

Conventionally, a diamond saw blade is used to separate a wafer. The use of diamond saw blade is reliable for cutting silicon substrates more than 300  $\mu\text{m}$  in thickness [3].



However, the saw dicing process has critical disadvantages, such as causing undesirable chipping and micro-cracks due to the nature of the mechanical force applied. Damage to parts during mechanical dicing is becoming a more significant issue as the thickness of wafers decreases. Due to the contact characteristics of the diamond-saw-blade mechanism, cutting speed must be sacrificed in order to avoid any increase in mechanical damage. Machining productivity is then compromised.

As the thickness of substrates decreases, wafer handling becomes very difficult. Due to the brittle properties of wafers, unnecessary force can easily cause breakage. To prevent such damage, non-contact tools are to be preferred. Several new wafer-separating techniques have been developed in recent years to meet these challenges, such as scribing and breaking [4], dicing before grinding [5], laser-assisted inert-gas cutting [6,7], and laser cleaving [8]. Wafer-separating methods using a laser beam can be remarkably efficient. As a non-contact method, the laser beam offers flexibility in the controllable micro-machining process compared to the diamond saw blade, and cutting speed is increased as wafer thickness decreases.

Thermal-stress cracking, or cleaving by laser-beam irradiation, is one prospective technique for separating thin substrates from brittle materials such as silicon, sapphire and glass [8]. A temperature differential is created within the substrate by the supplied laser energy, causing a hot area to expand, developing a stress force that leads to fracture. The process has the advantages of eliminating the contamination of coolant and chips; tool wear and machining kerf are also avoided. As a non-contact process, it is also easy to fix the work piece on the machining table. Moreover, an extremely smooth surface can be produced, compared with poor surface finish and critical material deformation caused by conventional mechanical cutting. Furthermore, it has been reported that the strength of the brittle material produced by mechanical cutting decreases to 60% on average in mechanical glass cutting [9].

It is therefore important to understand the laser cleaving mechanism; astonishingly, however, little attention has been paid to the laser cleaving of silicon and sapphire wafer, as compared to glass cleaving [4,5,10,11,12,13,14]. Therefore, there is a need to consider laser cleaving in these contexts, as demand for these materials in the semiconductor industry grows.

The main concerns in laser cleaving are separating-surface quality and cleaving productivity. The thermal-stress cleaving process depends mainly on the heat energy supplied by the laser beam. The temperature at the area irradiated by the laser beam has been found to be an important factor for controlling crack propagation during the cleaving process and the cleaving-surface quality [8]. It is very difficult to measure the temperature at the point of laser irradiation because the beam size is very small and the temperature is changing rapidly. In this research, temperature during laser irradiation was measured by using a two-color pyrometer with an optical fiber, developed by Ueda et al. [15]. This pyrometer makes it possible to measure the temperature during laser irradiation with a wide bandwidth.

The separation of brittle material by laser cleaving was first developed by Lumley [16]. In this technique, the input energy provided by laser-beam irradiation produces a thermal gradient in a localized area of the work piece that causes the thermal stress to separate the material along the path of the laser beam. The material separation is similar to crack extension and is performed below the material transition temperature. The process uses less energy and enables high cutting speeds compared to laser evaporative cutting and laser scribing. However, Lumley's method required an initial groove or flaw to facilitate and control the fracture during laser-beam irradiation. In this study, a new method of preparing an initial groove is proposed. The micro-groove was first created by focusing a series of pulse laser beams onto a silicon wafer substrate through a micro-lens (Ishikawa et al. [17]). The introduction of the micro-groove was an essential step to overcome the problems of micro-

cracks, secondary cracks and processing accuracy of initial crack – produced by indenters in previous research. Therefore, it is essential to investigate the mechanism of micro-groove processing by controlling various parameters and process conditions.

The use of the initial groove or crack at the edge of the wafer substrate aims to accelerate and control the material separation during the laser cleaving process. The fracture is initiated from the groove or the crack, and then propagates in the direction of the laser spot. Different shapes of initial groove or crack will affect cleaving processing parameters such as temperature, fracture initiation time and quality of separating surface. For these reasons, the relationship between laser power, laser-spot temperature, cleaving initiation time and separating surface quality are investigated in this research.

Previous studies have concentrated on the laser cleaving performance, the thermal damage and the influence of the crystal orientation of the material [8,18,19]. However, study of the processing mechanism in the laser cleaving of brittle materials such as silicon or sapphire has been limited. The relationships between laser power, temperature, fracture initiation, crack propagation, cleaved-surface features and groove parameters can be recognized by investigating the experimental analysis, but such analysis is unable to explain the thermal-stress condition during the process. Therefore, the temperature and thermal-stress distribution during the cleaving process is analyzed here by the finite-element method (FEM).

### 1.1 RESEARCH OBJECTIVES

Thermal-stress cleaving by laser-beam irradiation has vast potential for separating thin substrates from brittle materials such as silicon and sapphire wafers. This method possesses many advantages over mechanical dicing and conventional laser cutting. It is therefore important to consider the mechanism of laser cleaving of brittle materials to take advantage of this prospective process. In addition, the demand for these materials is steadily increasing, but the mechanism of laser cleaving of these materials is still not well understood. Therefore, the main objective of this research is to study the laser-cleaving mechanism of brittle materials by using experimental and computational analysis. The relationships amongst laser power, temperature, fracture initiation, crack propagation, cleaved-surface features and groove parameters are established by using the experimental research, and the thermal-stress state during the irradiation process is also clarified by using the finite-element method (FEM). In this study, the use of micro-groove is introduced to facilitate the cleaving process while the influence of laser absorption on different materials is also examined.

### 1.2 DISSERTATION OUTLINE

The following is an outline of the contents of each chapter of this dissertation.

In Chapter 2, the application of lasers in material cutting is discussed briefly. Methods of wafer material separation are compared. In addition, the principle of thermal-stress cleaving is explained.

In Chapter 3, the fabrication of micro-groove by using a cylindrical micro-lens is discussed. The principle of the formation of micro-lens and micro-groove and the preparation method are explained. The results of micro-groove fabrication using a micro-lens are described.

In Chapter 4, the concepts of thermal radiation and temperature are discussed. The basic principle and the characteristics of the two-color pyrometer used in this research are discussed.

In Chapter 5, the investigation on thermal-stress cleaving is performed using a single-point laser. The influence of different types of initial cracks in laser cleaving is examined. The temperature and the AE signal are measured to observe the cleaving temperature and cleaving time. Computational analysis via the finite-element method (FEM) is used to investigate the thermal-stress condition inside the wafer.

In Chapter 6, the silicon-wafer separating mechanism with a moving laser beam using the thermal-stress cleaving method is examined experimentally and computationally using FEM. The effect of laser energy on the cleaving mechanism is analyzed, and the influence of the groove parameters, such as groove length and depth, are also studied. In addition, the

fracture toughness of the silicon wafer is measured and the stress intensity factor of material is analyzed.

In Chapter 7, the thermal-stress conditions during CO<sub>2</sub> laser-beam irradiation on a sapphire wafer are analyzed by using the finite-element method (FEM). Absorption of lasers is explained, and the thermal-stress condition with regard to absorption is described.

The final chapter (Chapter 8) summarizes the conclusions of this research.

## REFERENCES

- [1] J. Lawrence, J. Pou, D. K. Y. Low and E. Toyserkani, *Advances in Laser Materials Processing*, Woodhead Publishing, UK 2010.
- [2] C. Paydenkar, A. Poddar, K. Chandra and S. Harada, "Wafer Sawing Process Characterization for Thin Die (75 micron) Application," *2004 IEEE-SEMI Int'l. Electronics Manufacturing Technology Symposium*, pp. 74-77, 2004.
- [3] R. F. Toftness, A. Boyle and D. Gillen, "Laser technology for wafer dicing and microvia drilling for next generation wafers," *Proceedings of SPIE*, 5713, pp. 54-56, 2005.
- [4] O. Sibaily and B. Risherzhagen, "Laser dicing of Silicon and Composite Semiconductor Materials," *Proceedings of SPIE*, 5339, pp. 394-397, 2004.
- [5] T. Lieberenz and D. Martin, "Dicing before Grinding for Wafer Thinning," *Chipsale Rev.*, 10(4), pp. 51-55, 2006.
- [6] K. Venkatakrishnan and B. Tan, "Thin Silicon Wafer Dicing with a dual focused laser beam," *J. Micromech. Microeng.*, 17, pp. 2505-2515, 2007.
- [7] A. Boyle, *Laser Machining using an Active Gas*, US Patent US2006/0249480A1.
- [8] T. Ueda, K. Yamada, K. Oiso, A. Hosokawa, "Thermal Stress Cleaving of Brittle Materials by Laser Beam," *CIRP Ann. - Manuf. Technol.*, (51-1), pp.149-152, 2002

- [9] S. Nisar, S. Safdar, M A Sheikh and L. Li, "Evaluation of Minimum Distance for Split Rectangular Beam for Glass Cutting," *Proceedings of the 35th International MATADOR Conference*, pp. 143-146, 2007.
- [10] K. Shimizu, K. Takahashi, H. Morikasu, N. Ogoshi, K. Takeyama, Y. Wakayama and T. Obara, "Laser ablation of silicon wafer with a water microdrop," *J. of Laser applications*, 18(2), pp. 127-123, 2006.
- [11] M. S. Acker, "The Backend Process: step11- scribe and break," *Advanced Packaging*, 10(11), 2001.
- [12] S. Schoenfelder, M. Ebert, C. Landesberger, K. Bock and J. Bagdahn, "Investigations of the influence of dicing technique on the strength propertied of thin silicon," *Microelectronic Reliability*, 47, pp. 168-178, 2007.
- [13] S. Nisar, M. Sheikh, L. Li and S. Safdar, "Effect of thermal stresses on chip-free diode laser cutting of glass," *Optics & Laser Technology*, 41(3), pp. 318-327, 2009.
- [14] S. Nisar, M. Sheikh, L. Li and S. Safdar, "The effect of material thickness, laser power and cutting speed on cut path deviation in high-power diode laser chip-free cutting of glass," *Optics & Laser Technology*, 42(6), pp. 1022-1031, 2010.
- [15] T. Ueda, K. Yamada, and K. Nakayama, "Temperature of Work Materials Irradiated with CO<sub>2</sub> Laser," *CIRP Ann. - Manuf. Technol.*, vol. 46, no. 1, pp. 117-122, 1997.
- [16] R. M. Lumley, Controlled Separation of Brittle Materials Using a Laser, *The American Ceramic Society Bulletin*, vol. 48, no. 9, pp. 850-854, 1969.
- [17] T. Ishikawa, T. Ueda, T. Furumoto, A. Hosokawa and R. Tanaka, "Pre-Groove Development for Laser Cleaving of Brittle Materials by Using Micro-Lens," *Journal of Advanced Mechanical Design, Systems, and Manufacturing*, 6(6), pp. 841-848, 2012.
- [18] K. Yamada, T. Ueda, A. Hosokawa, Y. Yamane, K. Sekiya, "Thermal damage of silicon wafer in thermal cleaving process with pulsed laser and CW laser," *Proc. SPIE Laser-based Micro packaging*, 6107, pp. 61070H-61070H-10, 2006.
- [19] R. Takeda, T. Ueda, T. Furumoto, A. Hosokawa, R. Tanaka, "Study on Cleaving Mechanism of Silicon Wafer by Laser Beam Irradiation," *Proc. Leading Edge Manufacturing in 21st Century* (5), The Japan Society of Mechanical Engineers, pp. 589-592, 2009.

## **CHAPTER 2 : OVERVIEW OF LASER CUTTING AND THERMAL-STRESS CLEAVING**

### **2.1 INTRODUCTION**

Laser cutting nowadays is typically used in industrial manufacturing applications. Laser cutting is performed by directing laser-beam irradiation at the material, and commonly involves motion control by a computer system. The laser beam is focused on the material, which then either burns, melts, vaporizes or is blown away by a gas, leaving a cut edge with a high-quality surface. A laser beam is also able to separate brittle materials by applying localized heating to induce thermal stress.

Laser cutting is a preferred process presently due to its characteristics of high-speed processing, repeatability, and reliability for a wide variety of material types and thicknesses. The process has the ability to produce very clean cuts of very narrow widths. The process is particularly suitable for automatic cutting processes in high-volume production. One of the first industrial applications of laser cutting was to produce the slots in die boards. Nowadays, lasers are used to cut a wide variety of metallic materials, such as steel, super alloy, copper, aluminum and brass, as well as non-metallic materials such as ceramic, quartz, plastic, rubber, wood and cloth [1]. Some general advantages of laser cutting over conventional machining processes are summarized below [2]:



1. **Non-contact process.** The work piece is not required to be clamped on specific fixtures as in conventional machining.
2. **Ease of automation.** Most laser-cutting processes are computer (CNC)-controlled, giving accurate dimension control.
3. **High cutting speeds.** Laser cutting is a fast process compared with conventional cutting.
4. **Fine and precise cutting dimensions.** Laser cutting can perform fine and profile cutting.
5. **Better quality of cuts.** The desired area of the work piece can be processed with no effect on neighboring areas.
6. **Flexible process.** Laser cutting can be used in a wide range of materials from metallic to non-metallic.

## 2.2 LASER CUTTING METHODS

Lasers can be used in material cutting in several methods based on the interaction between the laser beam and the work piece, with the use of gas to assist in removing material. The three main methods of cutting materials by laser-beam irradiation are evaporative laser cutting, laser melting and blow, and laser cleaving/cracking. The selection of cutting method and cutting conditions depends on the type of laser employed, the work-piece thickness, and the thermo-physical properties of the material, such as conductivity, ductility and melting

temperature. Table 2-1 presents the summary of laser cutting methods, mechanisms, relative laser energy required and applications for the various materials.

### 2.2.1 Evaporative laser cutting

In evaporative laser cutting, the focused beam heats the surface of the material until the temperature reaches boiling point, vaporizes and generates a keyhole. The energy required for evaporation is high. In general, it is estimated that the energy required for the evaporative method is two times that needed for laser fusion cutting [2]. This method is suitable for processing a wide range of materials, particularly organic materials such as cloth, paper and polymer. The process has also been reported to be suitable for processing metals and ceramics. Furthermore, extensive studies have been carried out to study the formation of a deep groove by evaporation during laser cutting [1]. The nonreactive gas jet has been used to reduce the burning of the materials [3].

Table 2-1 Summary of laser cutting methods [1]

	Vaporization	Melting and blow		Laser cleaving
		Fusion	Reactive	
Mechanism	Material is vaporized as a result of high intensity of laser radiation	Material is melted as a result of laser radiation, and the melt is blown by pressurized gas jet	Material is melted as a result of laser radiation and exothermic energy, the melt is blown by pressurized gas jet	Material is separated as the result of thermally induced stress
Relative laser energy required	40	20	10	1
Gas type	Inert gas or no gas	Inert gas	Chemically reactive gas	Inert gas or no gas
Workpiece materials	Metals, ceramics, polymers	Metals, polymers, glasses, ceramics, composites	Metals, polymers	Ceramics

### **2.2.2 Laser melting and blow**

In this process, the surface of the work piece is heated and melted by a laser beam and forms an erosion, or layer of molten material, that extends throughout the thickness of the work piece. It is subsequently blown away by a pressurized gas jet. The process is classed as 'laser fusion cutting' or 'reactive laser cutting' based on the type of gases used during the operation.

In the case of laser fusion cutting, an inert gas such as argon and nitrogen is used. Since the transformation phase is melting, the energy required is lower than for evaporative laser cutting. Material cut with this process is usually metal.

In reactive laser cutting, a chemically reactive gas, such as oxygen, is used. The material is heated to the point where an exothermic reaction with an oxidizing coaxial gas jet is triggered, thus adding another source of heat to the process. This method is mostly used to cut thick sections of stainless steel, titanium and titanium alloy.

### **2.2.3 Laser cleaving**

This process is also known as thermal-stress cracking or a controlled fracture technique. The heat from a laser beam produces thermal stress in a localized area of the work piece, and the thermal stress force causes the material to separate along the path of the laser beam. The material separation is obtained by the crack extension. Since the material separation does not occur through the evaporating or the melting, the laser energy required is much lower than for the conventional evaporative laser cutting or the laser melting and blow process. This method has been reported to be successful with brittle materials such as glass and alumina ceramic [4]. The application of water-jet cooling in the laser cleaving process enables higher cutting

speed [5,6], while the utilization of a dual laser beam enables thicker work pieces to be separated by laser cleaving [7,8].

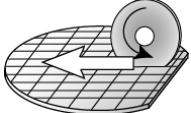
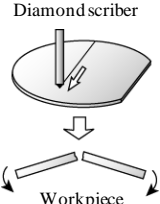

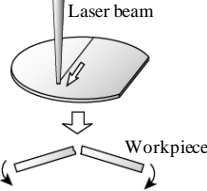
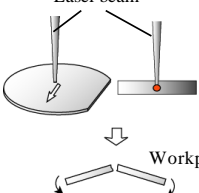
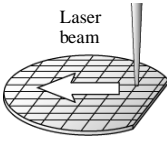
### **2.3 SEPARATION METHODS OF WAFER (BRITTLE) MATERIALS**

Micro-scale devices are often produced in large quantities from a single wafer through ‘clean room’ processes. A few hundred devices can be produced from a single wafer, depending on the size of the devices. In general, processing methods for wafer materials can be divided into two types: mechanical machining and laser processing. The processes for wafer separation and comparisons are summarized in Table 2-2.

#### **2.3.1 Mechanical dicing**

Over the past three decades, mechanical-blade dicing has been the main method for wafer dicing [9]. A diamond saw blade is used to cut a wafer with high-speed rotation. The machining accuracy is acceptable for thick wafer. However, the process generates physical stress on the material. The cutting creates a large amount of heat due to the contact friction, so cooling water is required. Furthermore, the process suffers from problems such as micro-cracks and chipping on the top and bottom edges of the substrate. Additionally, the cutting blade produces a cutting kerf and a feeding rate which needs to be minimized in order to control the damage on the wafer [10]. Fig. 2-1 shows an illustration of mechanical-blade dicing.

Table 2-2 Wafer-separating methods and comparisons

Cutting method	Process	Illustration	Cross section accuracy	Cost of equipment
Mechanical	Dicing	<p>Diamond blade</p>  <p>Workpiece</p>	△	○
	Scribing and snap	<p>Diamond scriber</p>  <p>Workpiece</p>	△	○
Laser	Laser full cut	<p>Laser beam</p> <p>Assist gas</p>  <p>Workpiece</p>	△	△
	Laser scribing and snap	<p>Laser beam</p>  <p>Workpiece</p>	○	△
	Stealth dicing	<p>Laser beam</p>  <p>Workpiece</p>	○	×
	Thermal stress cleaving	<p>Laser beam</p>  <p>Workpiece</p>	◎	△

◎ Excellent    ○ Good    × Notgood    △ Worst

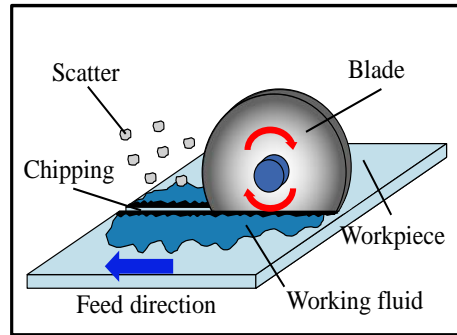


Fig. 2-1 Illustration of mechanical-blade dicing

### 2.3.2 Diamond scribing and snapping

In the diamond scribing and snapping method, the process typically uses crystal cleavage planes so that less physical cutting is needed and therefore less damage occurs to the wafer. A partial scribing is made, either with a special scribing tool or with a mechanical saw, which weakens the material surface. The purpose of the scribing is to generate the crack for the snapping along the desired cleavage plane by the application of mechanical bending.

Although the method is relatively simple, it results in the weakening of material edges by up to 60% due to the formation of micro-cracks and the generation of residual stresses [11]. To reduce these defects the material can be polished and heat treated, but these techniques only recover up to 30% of the material strength [11]. Fig. 2-2 illustrates the diamond scribing and snapping process.

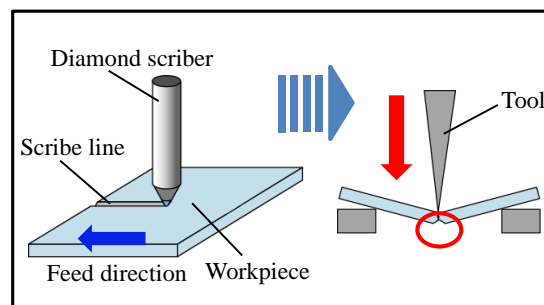


Fig. 2-2 Illustration of diamond scribing and snapping process

### **2.3.3 Laser scribing and snapping**

Laser scribing and snapping is a two-stage process and is quite similar to traditional mechanical scribing and snapping. In this method, a groove is scribed by laser-beam irradiation by means of heating and evaporating the material. The material surface is radiated by a laser beam to form the micro-grooves along the cleavage plane of the material.

Separation takes place by applying a mechanical force, normally with the help of vacuum chucks or crack rollers [12]. Several studies have sought to improve this method and the cutting quality [13,14]. The process is capable of performing the separation at high-speed, and offers better accuracy than the diamond scribing. However, micro-cracks and broken pieces are generated when the work piece is divided by applying mechanical stress. Therefore, finishing processes are required, which add extra costs to the manufacturer.

### **2.3.4 Laser full cut**

Laser full cut is a method that cuts the wafer only through a laser process. This method is effective for thin silicon, compound semiconductor, wafer with backside metal film, high-brightness LED substrate, and metal (Cu, molybdenum). The material is divided by the evaporative laser cutting procedures with an option to be assisted by inert gas. The cutting process is normally performed by irradiating a laser beam for several passes on the material surface [15].

However, this process requires very high laser power in order to completely melt and evaporate the material in the depth direction, and the accuracy of the machined surface is poor. Cracks also occur due to the thermal effects and the residual stress [16]. Therefore, grinding and polishing at the end of the process become inevitable. Fig. 2.3 illustrates the removal principle for evaporation in laser full cut.

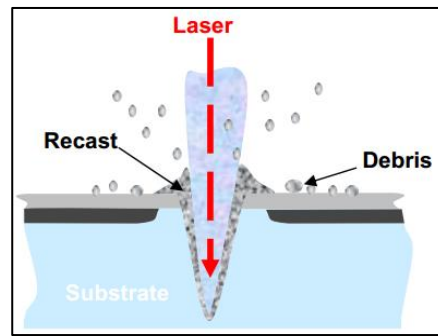


Fig. 2.3 Removal principle for evaporation in laser full cut

### 2.3.5 Stealth dicing

Stealth dicing is a non-evaporative technique which is based on internal modification of silicon wafer, as proposed by Hamamatsu Photonics K.K., Japan [17, 18]. The stealth dicing process consists of two steps. The silicon wafer is radiated by a laser beam and then separated by applying an external force such as a tape expander. A nanosecond-pulsed infrared laser beam is applied to the surface of the wafer, and is sharply focused inside the material. The laser beam does not damage the surface, but the modified region and cracks are generated in the intermediate plane inside the material. Debris pollution and thermal effects do not occur, unlike with the conventional laser full cut. Fig. 2.4 shows the illustration of laser irradiation in the stealth dicing method [19].

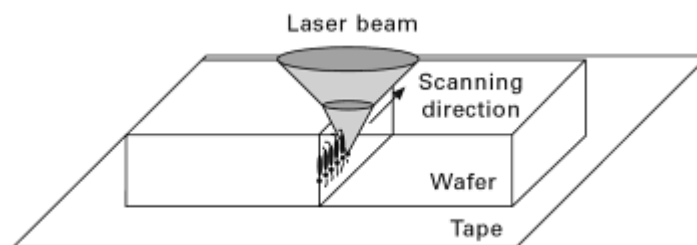


Fig. 2.4 Illustration of the laser irradiation in the stealth dicing process



However, the melting trace from the laser-beam irradiation remains inside the material. Moreover, because the modified layer produced is very small, multiple modified layers are necessary to achieve good wafer separation. Additionally, the stealth dicing process is usually difficult to be implemented because the equipment cost is expensive compared to other laser-processing machines.

### **2.3.6 Thermal-stress cleaving**

In thermal-stress cleaving, materials can be separated by applying the thermal-stress effect without removing the substrate materials. This process is based on the fracture mechanism of the brittle substrate caused by a large temperature gradient. By using a focused laser beam to generate a steep temperature gradient around the heating zone, the thermal stress spreads to coincide with the laser beam's path in a controllable way [20]. The material separation is due to the propagation of the crack. The fast crack propagation characteristics of brittle material enable high cutting speed compared with other conventional wafer separation methods. The separation quality is good because the edges are free from chipping and micro-cracks, so no additional finishing is required of the edges. In addition, the crack propagation progresses to follow the laser beam, which enables curve fracturing. These features have attracted much attention and this is considered an important prospective method for processing hard and brittle materials.

### 2.4 BASIC PRINCIPLES OF THERMAL-STRESS CLEAVING

Thermal-stress cleaving is a process which is used to separate a brittle material by irradiating a laser beam onto a small area on the substrate. The material separation is performed by generating thermal stress at the local area of the groove or the initial crack, and the fracture propagates along the laser path.

Fig. 2.5 shows the material substrate with the initial crack when the laser beam is irradiated onto the substrate. A rapid temperature rise at the irradiation area causes a thermal expansion of the material. The heated region is confined in a low-temperature area around the irradiation unit. Therefore, compressive stress is generated on the laser-spot area while tensile stress is generated around it. The tensile stress acts in the circumferential direction around the irradiation unit. When the stress magnitude reaches the fracture strength of the material, a fracture will be initiated in the tensile stress area and propagates toward the laser irradiation spot. As the laser beam moves, the fracture will propagate along the laser path, resulting in the separation of the wafer.

Since the material separation process is similar to crack extension, there is a need for preparation of the crack starting point. The separation technique of thermal-stress cleaving offers great advantages over the other processes. This technique has the capability to produce an extremely smooth surface. The contamination of coolant and chips can be eliminated, tool wear does not occur and machining kerf can be avoided. Furthermore, as a non-contact process it is also possible to fix the work piece on the machining table using a simple method. Therefore, it is worth devoting attention to establishing an effective method for preparing the initial crack.

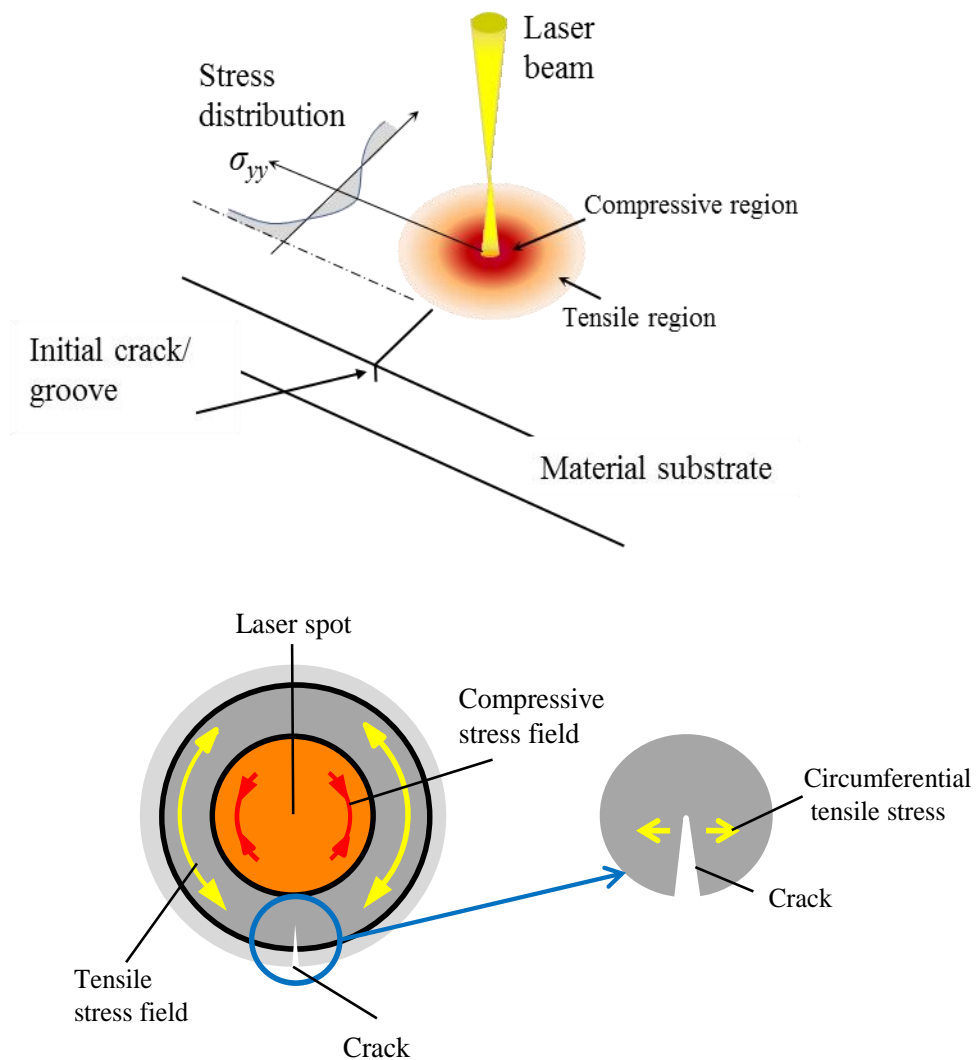


Fig. 2.5 The principle of thermal-stress cleaving

## 2.5 PREVIOUS RESEARCH

The first application of a laser in separating brittle material was to scribe grooves along the desired path before breaking by ultrasonic energy [21]. A laser is used to scribe the wafer along the desired separation line, and then the scribed wafers are immersed in an ultrasonic cell and broken along the scribed lines by ultrasonic energy. It is necessary to concentrate the laser energy on a narrow line with the work piece placed on the focal plane. The scribed substrates are broken along the scribed line by applying a mechanical force induced from the cracking roller.

Lumley proposed an important laser cutting process that has high potential for separating brittle materials such as alumina ceramic and glass by using a controlled fracture technique [4]. This procedure uses less laser power than conventional laser evaporative cutting and laser scribing, and enables high cutting speeds. The applied laser energy produces a mechanical stress that causes the material to separate along the path of the laser beam. The material separation is similar to a crack extension and the fracture growth is controllable. In order to ensure accurate splitting, it is essential that the stress field must be symmetrical with the crack [22]. However, for most cutting conditions the cutting path is not symmetrical, so the crack extension trajectory will deviate from the desired cutting path.

Later, the laser cutting process was developed to separate glass by using two lasers [23]. The first laser beam was used to create a shallow groove via heating and vaporizing procedures to produce a 0.2-mm-deep groove-crack. The second laser beam generated thermal stress at the groove tip to separate the material controllably. The cutting thickness can be greater than 5 mm for vitreous or glass material.

A laser breaking LCD glass substrate with the use of diamond scribing has also been investigated [24]. A groove-crack was created along the cutting path using a scoring tool before being separated with thermal-stress cleaving by applying a defocused CO<sub>2</sub> laser beam.

The application of a single laser has been reported on for laser separating of alumina with a controlled fracture technique [20]. A shallow groove was created by using an evaporative procedure, and heat produced from the laser beam generated a time-dependent thermal stress along the moving path. The cutting process was divided into three stages. In the first stage, fracture initiates due to tensile stresses. Stable crack growth is observed in the second stage, and in the third stage, the crack extends unstably due to complete domination of tensile stresses.

A similar method to the controlled fracture technique has been proposed for cutting glass [25]. In this technique, a small scratch is formed at the start of the cut, which helps in initiating the crack and leads to the separation of the glass. The controlled fracture technique has been improved upon by introducing a water-air mixture along the cutting path to generate tensile stresses and to maintain the temperature below the glass transition temperature [25]. However, the coolant adds extra cost and complexity to the process.

Further investigation has been performed on the use of lower-power lasers to separate non-metallic materials, specifically glass, where an additional water-jet coolant is applied to produce tensile stress along the cutting path [26,27]. The surface of a glass plate is heated by a CO<sub>2</sub> laser and the heated zone is subjected to local cooling to form a blind crack. The cooling is in the form of a mixture of water and air. The method can increase the cutting speed and accuracy, and can also control the depth, shape and angle of the cut face formed by the crack. However, again, use of a coolant adds extra cost and complexity to the process.

Several studies have been performed on the thermal-cleaving process of a silicon wafer. The influence of irradiating conditions of a laser beam on cleaving accuracy and thermal damage to work materials was investigated experimentally [28]. Temperature at the area irradiated with a laser was recognized as an important factor in controlling the propagation of the crack and in achieving high cleaving accuracy with low thermal damage.

To minimize the thermal damage, a cleaving process with pulsed laser irradiation and the application of a refrigerating chuck for cleaving with a continuous-wave (CW) laser were recommended [29]. Pulsed laser cleaving can be performed without thermal damage under the condition that the laser-spot temperature is higher than the critical temperature, i.e., where the temperature that produces the thermal stress is high enough to induced the material separation. Meanwhile, the relationship between crack propagation and cleavage plane has been investigated experimentally [30]. It was found that separation in the same direction of the wafer cleavage plane can be achieved at lower laser energy, furthermore improving the cleaving surface.

Temperature distribution inside the material is a critical importance in laser cleaving. The thermal gradient's distribution can be altered by laser parameters such as laser power, scanning speed, and beam spot size [31]. The heat generated from the laser beam during laser irradiation produces thermal stress gradients in the material substrate. Therefore, it is important to know the temperature during cleaving process.

It is difficult to measure the temperature of the laser spot during the thermal cleaving process because the laser beam is moving and its size is very small. The measurement of pulsed laser on metallic material using two silicon photo diodes has previously been reported [32]. Surface temperature of ceramic materials during laser-beam irradiation has also been carried out in real time using an infrared-radiation pyrometer with a fused fiber coupler [33].

Recently, a pyrometer composed of an optical fiber and InAs and InSb infrared detectors has been used to observe the temperature during laser consolidation of metal powder [34]. In this experiment, the temperature during laser irradiation was measured using a two-color pyrometer with different infrared detectors, namely InSb and MCT, and NSEG chalcogenide optical fiber.

Recently, the use of a micro-groove to facilitate the fracture initiation during the thermal-stress cleaving process has been introduced to overcome the problems that occur in the preparation of initial crack by using the Vickers indenter impressions [35]. Unnecessary crack and damage were eliminated during the initial crack preparation, subsequently improving the quality of the material specimen.

Experimental analysis established the relationships between laser cleaving parameters such as laser power, temperature, and groove dimensions and process performances such as fracture achievement and cleaved-surface finish. However, the thermal-stress condition during the process is yet to be explained. For this reason, thermal-stress distribution during the cleaving process is analyzed by the finite-element method (FEM).

The mechanism of crack propagation for a two-point pulsed Nd:YAG laser cutting silicon wafer has been investigated using the FEM method [36]. The numerical results show that the thermal stress is affected by laser power, and the cutting speed can be increased by controlling the distance between the laser beams. The thermal stress when machining a glass material was compared between single and dual CO<sub>2</sub> laser beams by FEM [37]. In dual CO<sub>2</sub> laser beams, an off-focus laser beam was used to preheat the glass, in addition to a focused CO<sub>2</sub> laser beam that was used to cut the material. The thermal stress was reduced by means of the dual-laser-beam method.

An analysis of the cut deviation problem of glass was conducted by examining the stress fields via FEM during diode-laser cutting of soda-lime glass sheets [38,39]. It was found that the cut deviation was due to the difference in stresses magnitudes at the leading and the trailing edges of the specimen compared to stress in the center of the material. When cutting at constant speed and laser power, smaller cut-path deviation occurs on thicker glass sheets. An increase in the cutting speed with constant power and a given thickness results in smaller cut-path deviations at the leading and trailing edges of the glass. The laser-beam geometry also has a recognized influence on the thermal stress generated during laser scanning [40].

## 2.6 CONCLUSIONS

The application of lasers in materials cutting has been introduced. Separation methods for brittle wafer materials have been discussed and compared. The basic principle of the thermal-stress technique in laser-beam irradiation is also explained. Thermal-stress cleaving possesses many advantages over other processing methods. This prospective technique offers high quality of the separation surface, high cutting speed and lower laser energy. As this technique attracts researchers and industries due to the advantages offered, it is important to understand the process mechanism, as proposed in this study.



## REFERENCES

- [1] J. P. Davim, *Nontraditional Machining Process*, Springer, Verlag London 2013.
- [2] N. B. Dahotre and S. Harimkar, *Laser Fabrication and Machining of Materials*, Springer, 2007.
- [3] J. E. Ready, *Industrial Applications*, Academic Press, 1978.
- [4] R. M. Lumley, "Controlled Separation of Brittle Materials Using a Laser," *The American Ceramic Society Bulletin*, vol.48, no. 9, pp. 850-854, 1969.
- [5] D. Kalyanasundaram, P. Shrotriya, P. Molian, "Fracture mechanics-based analysis for hybrid laser/water jet (LWJ) machining of yttria-partially stabilized zirconia (Y-PSZ)," *Intl. J. Mach. Tool Manufacturing*, 50, pp. 97-105, 2010.
- [6] C. Barnes, P. Shrotriya, P. Molian, "Water-assisted laser thermal shock machining of alumina," *Int. J. Mach. Tool Manuf.*, 47, pp. 1864-1874, 2007.
- [7] A. E. Segall, G. Cai, R. Akarapu, A. Romasco, B. Q. Li, "Fracture control of unsupported ceramics during laser machining using a simultaneous prescore," *J. Laser Appl.*, 17, pp. 57-62, 2005.
- [8] C. H. Tsai, H. W. Chen, "Laser cutting of thick ceramic substrates by controlled fracture technique," *J. Materials Processing Technology*, 136, pp.166-173, 2003.
- [9] V. Lindroos, M. Tilli, A. Lehto and T. Motooka, *Handbook of Silicon Based MEMS Materials and Technologies*, first edition, Elsevier, pp. 601-606, 2010.
- [10] T. Proulx, *Experimental and Applied Mechanics*, vol. 6, Springer, pp. 383-392, 2011.
- [11] A. B. Zhimalov, V. F. Solinov, V. S. Kondratenko, and T. V. Kaplina, "Laser cutting of float glass during production," *Glas. Ceram.* vol. 63, nos. 9-10, pp. 319-321, 2006.
- [12] C. H. Tsai, C. S. Liou, "Fracture mechanism of laser cutting with controlled fracture," *Trans. ASME, J. Manuf. Sci. Eng.*, vol. 125, pp. 519-528, 2003.
- [13] F. Ahmed, M. S. Lee, H. Sekita, T. Sumiyoshi, and M. Kamata, "Display glass cutting by femtosecond laser induced single shot periodic void array," *Appl. Phys. A*, vol. 93, no. 1, pp. 189-192, June 2008.
- [14] K. Du and P. Shi, "Subsurface precision processing of glass substrates by innovative lasers," *Glas. Sci. Technol.*, vol. 76, no. 2, pp. 95-98, 2003.
- [15] Disco Corporation, *Laser Application*, 2014. [Online] Available: <http://www.disco.co.jp/eg/products/catalog/pdf/laser.pdf>. [Accessed: 06 October 2014]

- [16] A. Kazuno, "Machinery and Tools," *Japan Industry Publication*, vol. 44, no. 5, pp. 59-63, 2000. (In Japanese.)
- [17] J. Lawrence, J. Pou, D. K. Y. Low and E. Toyserkani, *Advances in Laser Materials Processing*, Woodhead Publishing, 2010.
- [18] T. Sakamoto, K. Fukumitsu, *Laser Processing Method And Semiconductor Chip*, United States Patent Application 20070290299, 2007.
- [19] M. Kumagai, T. Sakamoto, E. Ohmura, "Laser Processing of Doped silicon wafer by the Stealth Dicing," *ISSM 2007: International Symposium on Semiconductor Manufacturing*, pp. 1-4, 2007.
- [20] C. H. Tsai, C. S. Liou, "Fracture mechanism of laser cutting with controlled fracture," *Trans. ASME, J. Manuf. Sci. Eng.*, vol. 125, pp. 519-528, 2003.
- [21] D. J. Garibotti, *Dicing of Micro-semiconductors*, U.S. Patent No.3,112,850, 1963.
- [22] F. J. Grove, D. C. Wright and F. M. Hamer, Cutting of glass with a laser beam, *U.S. Patent No. 3543979*, 1970.
- [23] E. Lambert, J. L. Lambert, B. D. Longueville, *Severing of a glass or vitrocrySTALLINE bodies*, U.S Patent No. 3935419, 1976.
- [24] C. H. Tsai, B. W. Huang, "Diamond scribing and laser breaking for LCD glass substrates," *Journal of Materials Processing Technology*, 198 (1-3), 350-358, 2008.
- [25] J. N. Dekker, and M. H. Zonneveld, "Thermal Severing. The cutting of brittle materials by thermally induced fracture advances in fracture research," *Proceedings of the Seventh International Conference on Fracture*, Pergamon, Houston, TX, pp. 2825-2834, 1989.
- [26] V. S. Kondratenko, *Method of splitting non-metallic materials*, US Patent 5609284, 1997.
- [27] U. Unger, W. Wittenbecher, "The cutting edge of laser technology," *Glass*, 75, 101-102, 1998.
- [28] T. Ueda, K. Yamada, K. Oiso, A. Hosokawa, "Thermal Stress Cleaving of Brittle Materials by Laser Beam," *CIRP Annals - Manufacturing Technology*, 51(1), 149-152, 2002.
- [29] K. Yamada, T. Ueda, A. Hosokawa, Y. Yamane, K. Sekiya, "Thermal damage of silicon wafer in thermal cleaving process with pulsed laser and CW laser," *Proc. SPIE Laser-based Micro packaging*, 6107, pp. 61070H-61070H-10, 2006.
- [30] R. Takeda, T. Ueda, T. Furumoto, A. Hosokawa, R. Tanaka, "Study on Cleaving Mechanism of Silicon Wafer by Laser Beam Irradiation," *Proc. Leading Edge*

- Manufacturing in 21st Century* (5), The Japan Society of Mechanical Engineers, pp. 589-592, 2009.
- [31] S. Nisar, M. a. Sheikh, L. Li, A. J. Pinkerton, and S. Safdar, "The Effect of Laser Beam Geometry on Cut Path Deviation in Diode Laser Chip-Free Cutting of Glass," *J. Manuf. Sci. Eng.*, vol. 132, no. 1, p. 011002, 2010.
  - [32] M. B. Ignatiev, I. Y. Smurov, G. Flamant, V. N. Senchenko, "Surface temperature measurement during pulsed laser action on metallic and ceramic materials," *Applied Surface Science*, vol. 96, no. 98, pp. 505-512, 1996.
  - [33] T. Ueda, K. Yamada, K. Nakayama, "Temperature of work materials irradiated with CO<sub>2</sub> laser," *CIRP Annals - Manufacturing Technology*, vol. 46, no. 1, pp. 117-122T, 1997.
  - [34] T. Furumoto, T. Ueda, N. Kobayashi, A. Yassin, A. Hosokawa, S. Abe, "Study on laser consolidation of metal powder with Yb: fiber laser – Evaluation of line consolidation structure," *Journal of Materials Processing Technology*, vol. 209, nos. 18-19, pp. 5973-5980, 2009.
  - [35] T. Ishikawa, T. Ueda, T. Furumoto, Hosokawa, A., Tanaka, R., "Pre-Groove Development for Laser Cleaving of Brittle Materials by Using Micro-Lens," *Journal of Advanced Mechanical Design, Systems, and Manufacturing*, vol. 6, no. 6, pp. 841-848, 2012.
  - [36] L. Jian, L. Jian, N. Xiaowu, D. Gang, Z. Liang, C. Yanbei, "Numerical study on thermal stress cutting of silicon wafer using two-point pulsed laser," *Optica Applicata*, vol. XLI, no. 1, pp. 247-255, 2011.
  - [37] J. Jiao and X. Wang, "A numerical simulation of machining glass by dual CO<sub>2</sub>-laser beams," *Opt. Laser Technol.*, vol. 40, no. 2, pp. 297-301, Mar. 2008.
  - [38] S. Nisar, M. Sheikh, L. Li, and S. Safdar, "Effect of thermal stresses on chip-free diode laser cutting of glass," *Opt. Laser Technol.*, vol. 41, no. 3, pp. 318-327, Apr. 2009.
  - [39] S. Nisar, M. A. Sheikh, L. Li, A. J. Pinkerton, and S. Safdar, "The Effect of Laser Beam Geometry on Cut Path Deviation in Diode Laser Chip-Free Cutting of Glass," *J. Manuf. Sci. Eng.*, vol. 132, no. 1, p. 011002, 2010.
  - [40] S. Nisar, M. A. Sheikh, L. Li, and S. Safdar, "The effect of material thickness, laser power and cutting speed on cut path deviation in high-power diode laser chip-free cutting of glass," *Opt. & Laser Technol.*, vol. 42, no. 6, pp. 1022-1031, 2010.

## **CHAPTER 3 : MICRO-GROOVE FABRICATION BY USING A MICRO-LENS**

### **3.1 INTRODUCTION**

In the laser cleaving process, the separation of brittle materials takes place due to the thermal stress generated in the material. The laser energy absorbed in the local area produces a mechanical stress that causes the material to separate along the path of the laser beam. The separation is similar to a crack extension [1]. The procedure uses less laser power and enables higher cutting speeds compared to conventional laser cutting methods. However, the process requires an initial crack or groove to facilitate and control the fracture during laser irradiation.

The first application of a laser beam in fabricating a groove for separating semiconductor material was proposed by Garibotti [2]. A laser was used to scribe the grooves along the desired line before breaking by ultrasonic energy. Later, use of two laser beams was developed to enable the laser cutting process to separate glass material [3]: the first laser beam was used to create a shallow groove via heating and vaporizing procedures, and the second was used to generate thermal stress at the groove tip to separate the material. The laser cutting of alumina material by using a single laser beam was investigated [4]. A shallow groove was created by using an evaporative procedure, and heat produced from the laser beam generated a time-dependent thermal stress along the moving path. Use of diamond

scribing and laser breaking for LCD glass substrate was studied [5]. A groove-crack was created along the cutting path using a scoring tool before separating by applying a defocused CO<sub>2</sub> laser beam.

Several studies have been performed on the thermal cleaving process of a silicon wafer with preparation of the initial crack using an indenter [6,7,8]. However, these impressions create damages at the indentation area and a lateral crack in the direction perpendicular to the cleaving path. As an alternative to the micro-crack produced by an indenter, fabrication of a micro-groove by a laser has been proposed for initial crack preparation. The introduction of the micro-groove is essential to overcoming the problems of micro-cracks, secondary cracks and processing accuracy that have been reported in previous research [9].

In this chapter, the details of micro-lens development, including material properties, processing technique and process principles, is explained. The micro-lens is used as an optical focusing system in the making of a micro-groove on a silicon wafer specimen. The processing of micro-grooves is also discussed by emphasizing the processing parameters and resulting features.

### **3.2 DEVELOPMENT OF MICRO-LENS**

The micro-lens was formed using the thermal expansion technique, whereby the acrylic resin plate was irradiated with an Er:YAG laser beam. The heat from the laser increased the temperature up to the glass transition temperature; this is a reversible transition temperature where the material properties are changed from a hard and relatively brittle state into a molten or rubber-like state.

The principle elements of micro-lens fabrication are illustrated in Fig. 3-1. Due to the heat supplied by the laser beam, the heat portion of the acrylic material is expanded and transformed into the rubber-like state. At this time, when the portion of the rubber-elastic-state material solidifies to a stable shape, a curved lens shape results on the surface of the specimen.

Limiting the heating is possible by using a heat source of a laser beam with a short pulse width corresponding to the heating time. The transition between the glassy state and rubber elastic state can be made instantly by applying alternate heating and cooling using the short pulse laser. The expansion portion is small and the shape is stable while remaining in the rubber-elastic state. The fabrication of a micro-lens with convex hemispherical shape is thus realized.

### **3.2.1 Micro-lens material**

The micro-lens in this study was fabricated using an acrylic material (Acrylite EX) as a substrate, supplied by Mitsubishi Rayon, Japan. Acrylic resins feature excellent optical characteristics and durability and are used in a broad range of applications for consumer items, from lenses to industrial products like molding materials, coatings and adhesives. Table 3.1 and Table 3.2 display the specifications and the physical properties of the acrylic resin used in this study.

The main component of the acrylic resin is a methyl methacrylate and acrylic ester. Acrylic is a thermo-reversible material. The material transforms to a rubber-elastic state at about 100°C and returns to the glassy state (solid) with stable shape when the temperature

decreases. Deformation of the molecule in the rubber-elastic state secures its shape then solidifies to form a lens.

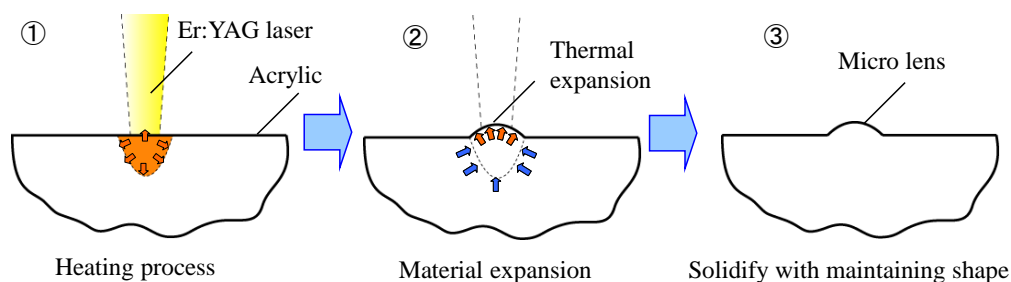


Fig. 3-1 The principle of micro lens making

Table 3-1 Specifications of Acrylite EX

Product name	Acrylite EX	
Chemical component	Methyl methacrylate	Acrylic ester
Content	Over 90 %	Under 10%
Structural formula	$(C_5H_8O_2)_x$	$(C_4H_6O_2)_y (C_7H_{12}O_2)_z$
Manufacturing process	Continuous extrusion molding	

Table 3-2 Physical properties of Acrylite EX

Acrylite EX		units
Tensile strength, $TS$	74	MPa
Bend strength, $BS$	120	MPa
Refractive index, $n$	1.49	
Specific heat capacity, $C$	$1.5 \times 10^3$	J/kg · K
Specific gravity, $SG$	1.19	
Thermal expansion coef., $\alpha$	$7 \times 10^{-5}$	K <sup>-1</sup>

### 3.2.2 Optical properties

Fig. 3-2 shows the spectral transmittance of the acrylic specimen with thickness of 3 mm. At wavelength below about 1100 nm, the spectral transmittance is 90%, but the transmittance reduces gradually as the wavelength is increased. In this study, the laser used was Er:YAG, with a wavelength of 2940 nm. At this wavelength the laser energy is absorbed into the acrylic EX, where the transmittance is only about five percent. Therefore, the Er:YAG laser is suitable for the production of the lens.

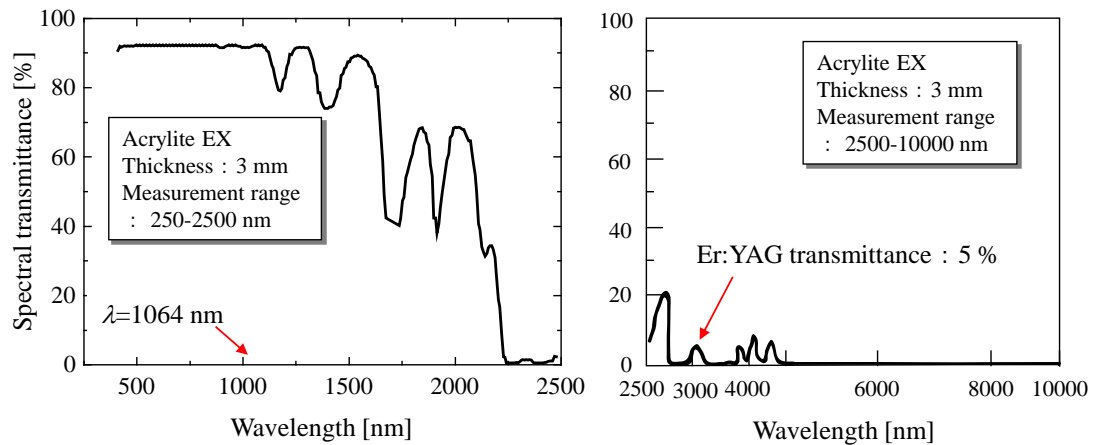


Fig. 3-2 Spectral transmittance of the Acrylite EX

### 3.2.3 Micro-lens fabrication method

Fig. 3-3 illustrates the experimental apparatus for the micro-lens fabrication. The acrylic specimen plate is fixed horizontally on the X-Y stage (moving table). The specimen is irradiated with an Er:YAG laser as above. A sapphire condenser lens with a focal length of 100 mm was used in this study. The X-Y stage moves during the laser irradiation so that a semi-cylindrical micro-lens forms on the acrylic plate.



The experimental conditions of micro-lens fabrication are shown in Table 3-3, and the details of laser irradiation are illustrated in Fig. 3-4. The specimen was irradiated with pulse irradiation mode of the Er:YAG laser with a wavelength of 2940 nm. Defocus length was set at 4 mm, where the laser-spot diameter on the specimen surface was 0.4 mm. Laser power was set to 32 mW with pulse width of 0.2 ms, while the X-Y stage was moving at a constant speed of 4  $\mu\text{m/s}$ .

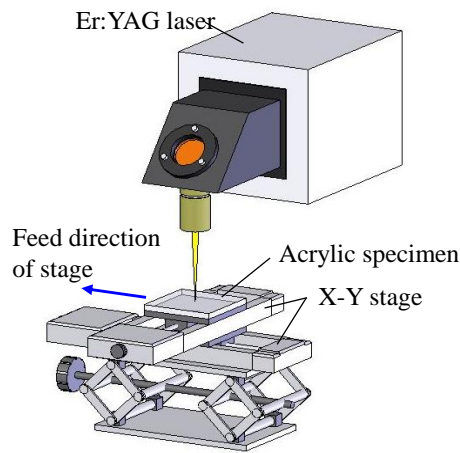


Fig. 3-3 Experimental apparatus of micro lens fabrication

Table 3-3 Experimental condition of micro lens fabrication

Er:YAG laser		units
Wavelength, $\lambda$	2940	nm
Irradiation mode	Pulse	
Pulse width, $\tau$	0.2	ms
Defocus, $df$	4	mm
Beam diameter, $D$	0.4	mm
Frequency, $f$	4	Hz
Scan speed, $v$	4	$\mu\text{m/s}$
Laser power, $P$	32	mW
Workpiece	Acrylic board	
Size	50×50×3	mm

### 3.2.4 Micro-lens shape

A three-dimensional profile of the micro-lens fabricated is shown in Fig. 3-5, while a two-dimensional profile is displayed in Fig. 3-6 [10]. Profile measurement has been performed by using SURFCOM 2000-DX2 surface-texture and contour integrated measuring instruments by Tokyo Seimitsu Ltd. The radius of the circle shown in Fig. 3-6(a) represents the curve shape of the micro-lens obtained by thermal expansion. The radius of this curvature is related to the focal length of the lens. The overall dimensions of the micro-lens are 20  $\mu\text{m}$  in height and 150  $\mu\text{m}$  in width.

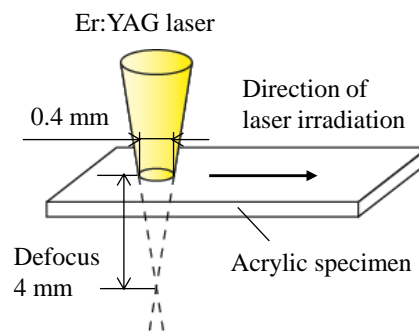


Fig. 3-4 Illustration of laser irradiation condition

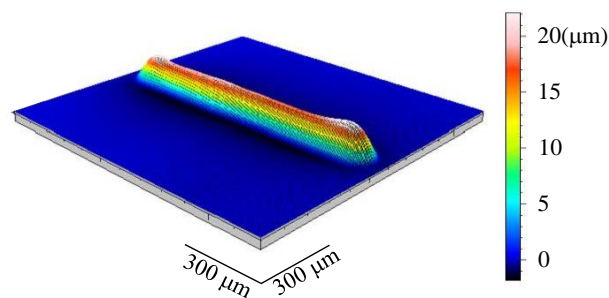


Fig. 3-5 3D profile of the micro lens [10]

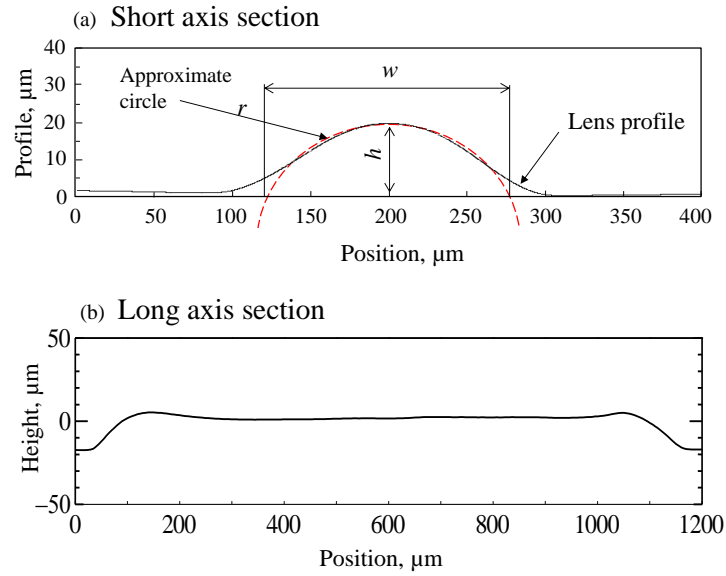


Fig. 3-6 2D profile of the micro lens

### 3.3 MICRO-GROOVE PROCESSING

In common groove manufacture by laser processing, the laser-beam irradiation moves along the groove line at the same time as the material is removed from the material surface. However, in this study a fine groove is created by focusing a static laser beam into a line by using a semi-cylindrical shaped micro-lens, as produced in the previous section.

The principle of micro-groove processing is illustrated in Fig. 3-7. The removal process is achieved through melting and vaporizing of the material due to the high energy density at the specimen surface. The pulsed laser beam is focused by the micro-lens. A portion of the material on the surface is melted and vaporized after further heating by the laser beam. Material removal progresses in the depth direction, away from the focal point of the micro

lens. The energy density of the laser beam is decreasing; hence, the molten region of the material is reduced. Thus, the narrowed groove is produced.

In this study, the processing conditions of the micro-groove are established so that a fine groove with optimum parameters can be fabricated. The relationships between laser power, irradiation pulse number and groove parameters are discussed. The influences of the micro-groove on laser cleaving processes are investigated in the next chapters.

### 3.3.1 Experiment methodology

In this experiment, the laser used was a second-harmonic-generation (SHG) Nd:YAG laser with a wavelength of 532 nm. As shown in Fig. 3-8, the laser processing equipment is composed of a laser oscillator unit, a power supply unit with the control panel, and the laser filtering instrument, a Separation package from Surflite™ (Continuum, Inc.). The Separation package unit does not include a condenser lens, so a non-focusing laser beam is emitted.

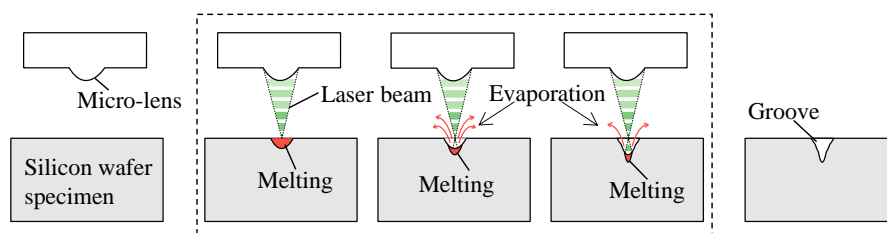


Fig. 3-7 The principle of micro-groove processing

Fig. 3-9 illustrates the arrangement of the experimental apparatus for making the micro-groove, while Fig. 3-10 shows the details of the laser focusing area. The laser beam is emitted horizontally from the Nd:YAG (SHG) laser machine and condensed through the micro-lens. The specimen is exposed to a focused laser beam, which starts the melting and vaporizing processes. The laser beam is irradiated on the specimen in the water, where the lens substrate is attached to the acrylic resin container. Since the specimen is attached on a jig with a micrometer head, position adjustment in three directions is possible.

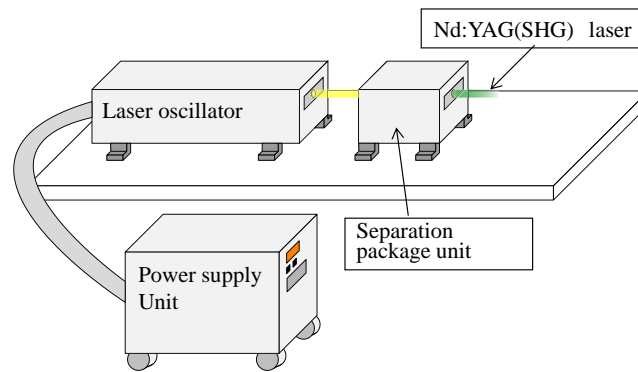


Fig. 3-8 The laser processing equipment

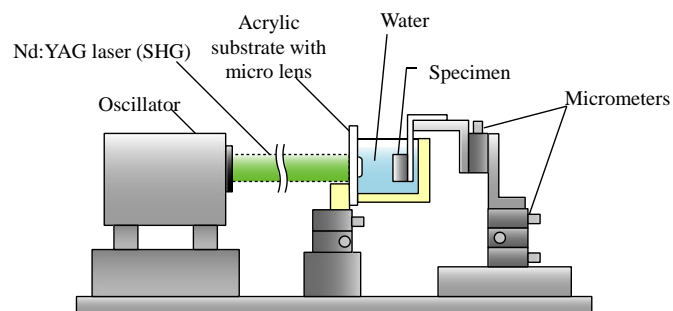


Fig. 3-9 The experimental apparatus arrangement in micro-groove fabrication

Table 3-4 displays the laser irradiation conditions for micro-groove fabrication. The laser used was Nd:YAG (SHG) with a wavelength of 532 nm. The beam diameter before focusing through the micro-lens was 5 mm, while the laser frequency was set at 10 Hz. Laser power ranged from 55 to 390 mW and irradiation pulses varied between 100 and 1000 in number. The work distance was fixed at 0.8 mm.

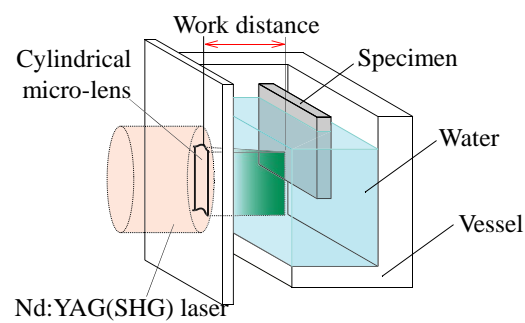


Fig. 3-10 Details of micro-groove fabrication

Table 3-4 Laser irradiation conditions

Nd:YAG(SHG) laser	532	units
Wavelength, $\lambda$	532	nm
Irradiation mode	Pulse wave	
Pulse width, $\tau$	4.8	ns
Beam diameter, $D$	5	mm
Frequency, $f$	10	Hz
Laser power, $P$	55-390	mW
Number of pulse, $N$	100	pulse
Work distance, $d_w$	0.8	mm
Workpiece	Silicon wafer	
Size [ $\text{mm}^3$ ]	10×20×0.5	$\text{mm}^3$

### 3.3.2 Results and discussion

#### (a) Relationship between laser power and groove width

In these experiments, the laser irradiation pulse was set constant at 100 pulses. Observation of the micro-groove images on the silicon-wafer surfaces was performed using a scanning electron microscope (SEM). Images of the observed micro-grooves are shown in Fig. 3-11. The results show that a fine groove was successfully produced by using the micro-lens. The groove width was enlarged as the laser power increased. For instance, at laser powers of 55 mW and 390 mW, the observed groove widths were 1.9  $\mu\text{m}$  and 8.6  $\mu\text{m}$ , respectively. However, heat damage was also found to increase proportionately with the laser power. The relationship between the laser power and groove width is shown in Fig. 3-12.

#### (b) Relationship between laser irradiation pulse and groove depth

In this experiment, the effect of the laser irradiation pulse on the groove depth was examined. The irradiation pulse number varied between 100 and 1000, while laser power was changed between 55 to 280 mW. SEM images of the groove cross-section are shown in Fig. 3-13. The results indicate that groove depth increased with increases in the number of irradiation pulses and laser power. At the smallest laser power of 55 mW, and irradiation pulse number of 100, groove depth was found to be 16.5  $\mu\text{m}$ . At the highest laser power of 280 mW, and irradiation with 1000 pulses, a groove depth of 100  $\mu\text{m}$  resulted. The groove was large on the surface and narrowed in the depth direction. The relationships between the groove depth and irradiation pulse number for laser powers of 55, 175 and 280 mW are shown in Fig. 3-14.

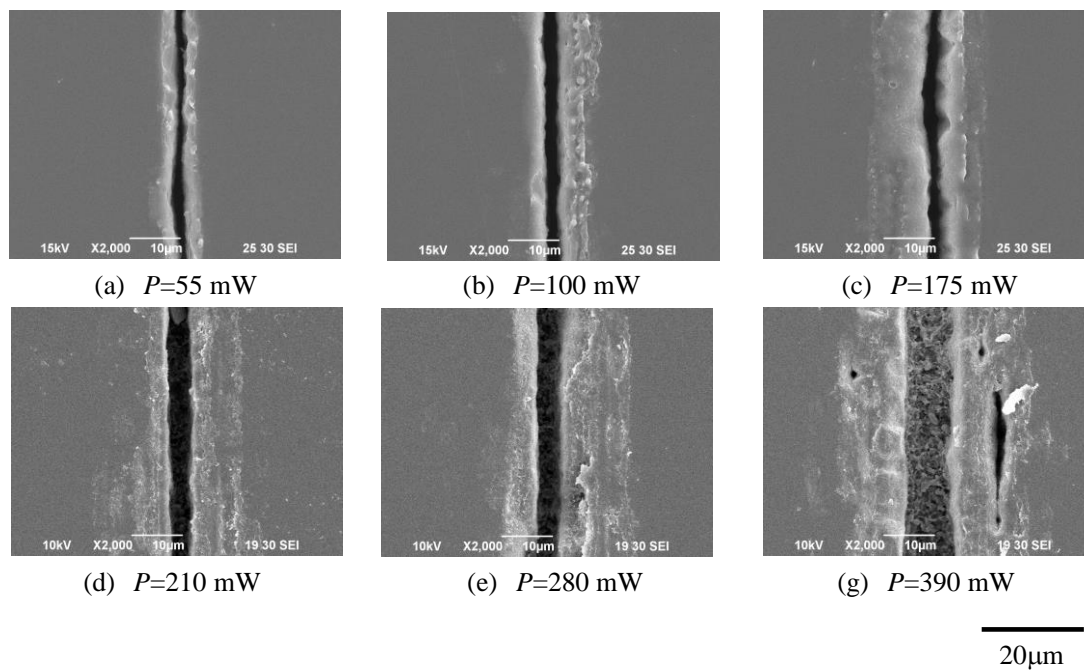


Fig. 3-11 SEM images of micro-grooves observed on the surface of silicon wafer

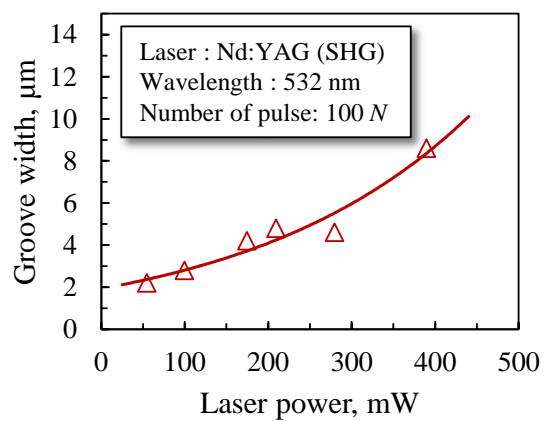


Fig. 3-12 The relationship between laser power and groove width



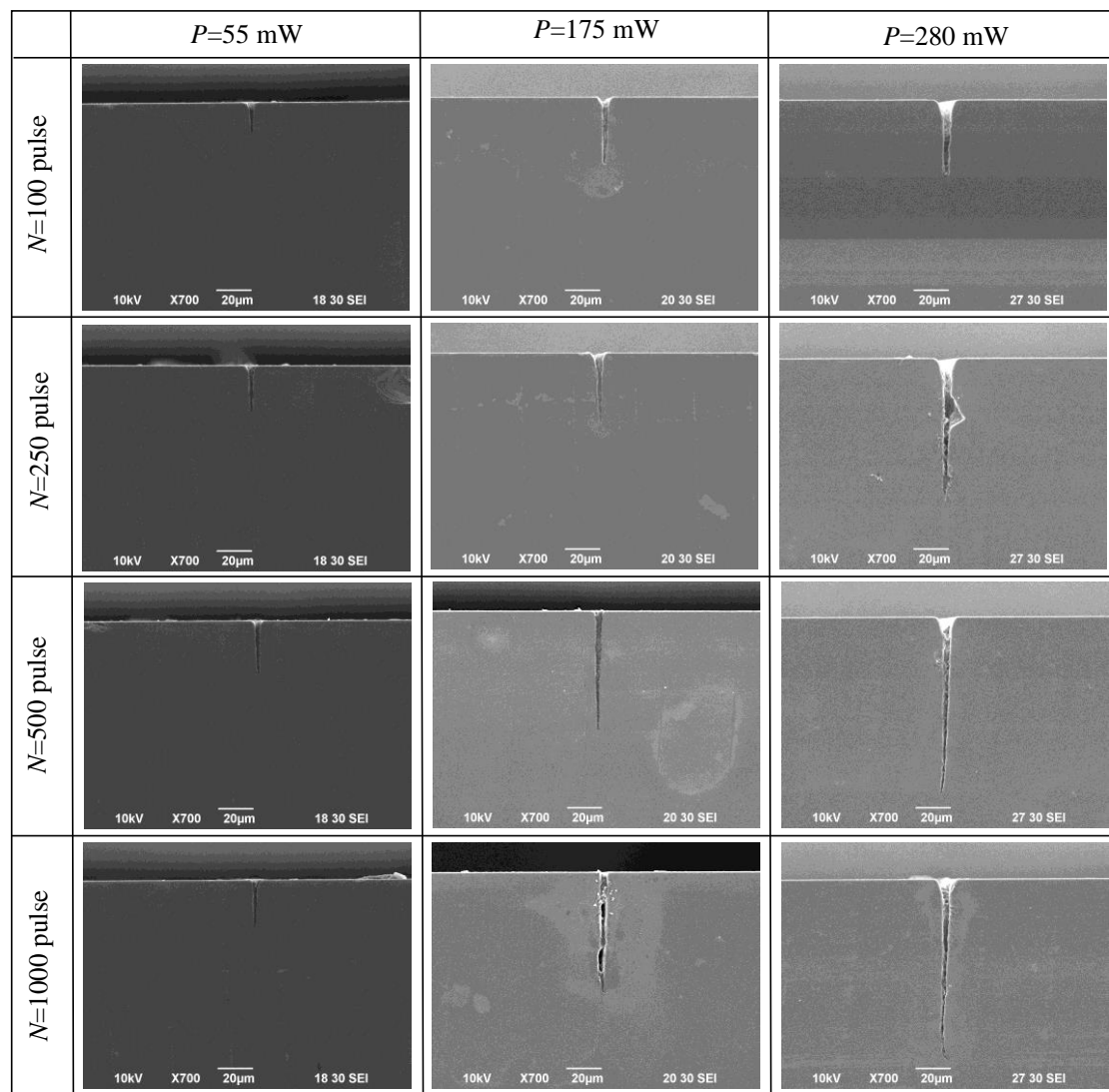

 50  $\mu\text{m}$ 

Fig. 3-13 SEM images of the groove cross-section

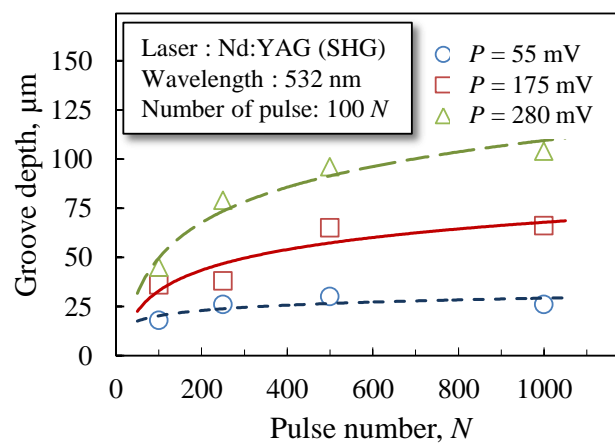


Fig. 3-14 Relationship between the groove depth and irradiation pulse number

### 3.8 CONCLUSIONS

The fabrication of a micro-groove using a semi-cylindrical micro-lens has been discussed. The development of the micro-lens, including process principles, material properties and processing technique, has been explained. This micro-lens was used effectively for focusing the laser beam on the silicon-wafer surface during micro-groove fabrication. The material was heated and vaporized, and consequently a groove was formed.

The processing of the micro-groove was mainly influenced by two parameters: laser power and irradiation pulse number. The width of the micro-groove increased with increased in laser power, while the depth increased with increased laser irradiation pulse. These results are essential for the preparing of the micro-groove on the specimen for the experiment presented in the next chapters.

## REFERENCES

- [1] C. H. Tsai, H. W. Chen, "Laser cutting of thick ceramic substrates by controlled fracture technique," *J. Mater. Process. Technol.*, vol. 136, no. 1-3, pp. 166-173, May 2003.
- [2] D. J. Garibotti, *Dicing of Micro-semiconductors*, U.S. Patent No.3112850A, 1963.
- [3] E. Lambert, J. L. Lambert, B. D. Longueville, *Severing of a glass or vitrocrySTALLine bodies*, U.S Patent No. 3935419 A, 1976.
- [4] C. H. Tsai, C. S. Liou, "Fracture Mechanism of Laser Cutting With Controlled Fracture," *Journal of Manufacturing Science and Engineering*, ASME, 125(3), pp. 519-528, 2003.
- [5] C. H. Tsai, B. W. Huang, Diamond scribing and laser breaking for LCD glass substrates, *Journal of Materials Processing Technology*, 198 (1-3), 350–358, 2008.
- [6] T. Ueda, K. Yamada, K. Oiso, and A. Hosokawa, "Thermal Stress Cleaving of Brittle Materials by Laser Beam," *CIRP Ann. - Manuf. Technol.*, vol. 51, no. 1, pp. 149-152, 2002.
- [7] K. Yamada, T. Ueda, A. Hosokawa, Y. Yamane, and K. Sekiya, "Thermal damage of silicon wafer in thermal stress cleaving process with pulsed and CW laser," *Proc. SPIE Laser-based Micro packaging*, vol. 6107, pp. 61070H-61070H-10, 2006.
- [8] R. Takeda, T. Ueda, T. Furumoto, A. Hosokawa, R. Tanaka, N. Science, P. The, A. Corp, I. Laser, and Y. Kuo, "Study on Cleaving Mechanism of Silicon Wafer by Laser Beam Irradiation," *Proc. Leading Edge Manufacturing in 21st Century*, The Japan Society of Mechanical Engineers, vol. 5, no. 100, pp. 589-592, 2009.
- [9] T. Ishikawa, T. Ueda, T. Furumoto, A. Hosokawa, and R. Tanaka, "Pre-Groove Development for Laser Cleaving of Brittle Materials by Using Micro-Lens," *J. Adv. Mech. Des. Syst. Manuf.*, vol. 6, no. 6, pp. 841-848, 2012.
- [10] H. Kato, Laser micro machining: *Utilization of the micro lens fabrication*, Master Dissertation, Kanazawa University, 2013.

## **CHAPTER 4 : BASIC PRINCIPLES AND CALIBRA- TION OF TWO-COLOR PYROMETER**

### **4.1 INTRODUCTION**

In the thermal-stress cleaving process, it is understood that the separation of brittle materials is subjected to the thermal-stress generation in the material. The magnitude of the thermal stress is dependent on the temperature distribution in the material. Therefore, the measurement of the temperature at the laser irradiation area is very important in laser cleaving. The excessive heat generated is one of the main causes of material damage; however, insufficient heat could interrupt the achievement of material separation. Measurements of the temperature at the laser spot area are very difficult to obtain because the area irradiated with the laser beam is very small, the laser-beam diameter is about a few hundred micrometers. Furthermore, the temperature changes very rapidly. Efforts have been made to measure the temperature during laser irradiation using a ‘thermocouple’ technique, placing a constantan wire on the opposite side of the irradiated surface [1]. In this study, the temperature in the irradiated region was estimated from the experimental results. However, calibration of the thermocouple was difficult, especially at high temperatures. Moreover, the technique was not able to respond to rapid changes of temperature. Temperature measurement of a moving laser beam also proved impossible.

Therefore, a non-contact instrument with an optical fiber was applied in the research presented here. The temperature measurement utilized thermal radiation principles. Energy in the form of electromagnetic radiation is emitted from a heated surface and is detected by the sensor in the thermal radiation measuring system, namely an infrared radiation pyrometer. During temperature measurement using the pyrometer, there is no need for direct contact with the measured object; the pyrometer can also respond to rapid changes of temperature because of its high response speed. This facilitates measurement of the moving target, and the flexibility of the optical fiber enables the measuring of temperature in a tiny space of the working area.

In this chapter, the concepts of thermal radiation and temperature are discussed. The two-color pyrometer and its components are introduced and the basic principles of the pyrometer and its calibration are explained.

## **4.2 THERMAL RADIATION**

Energy that is propagated through a vacuum or a material medium in the form of electromagnetic waves is known as electromagnetic radiation. Electromagnetic radiation is continuously emitted from substances because of the molecular and atomic agitation associated with their internal energy. Electromagnetic radiation covers a wide range of wavelengths, from  $10^{-10}$   $\mu\text{m}$  for cosmic rays to  $10^{10}$   $\mu\text{m}$  for electrical power waves. The interest in this study is thermal radiation. Thermal radiation waves form a narrow band on the electromagnetic wave spectrum. Thermal radiation is emitted as a result of energy transitions

of the molecules, atoms, and electrons of a substance. Temperature is a measure of the strength of these activities at microscopic level.

Fig. 4-1 illustrates the wavelength and frequency domains of thermal radiation in a vacuum, and their position on the electromagnetic spectrum. With reference to wavelength, the thermal radiation is located between approximately 0.1 and 100  $\mu\text{m}$ . The thermal radiation domain can be divided into the three following sub-areas: the ultraviolet range, the visible range, and the infrared range.

The range of thermal radiation visible to the naked eye is found roughly from 0.4 to 0.7  $\mu\text{m}$ . The infrared range extends from the visible region to about  $\lambda = 1000 \mu\text{m}$ , and the ultraviolet range is generally below  $\lambda = 0.4 \mu\text{m}$ .

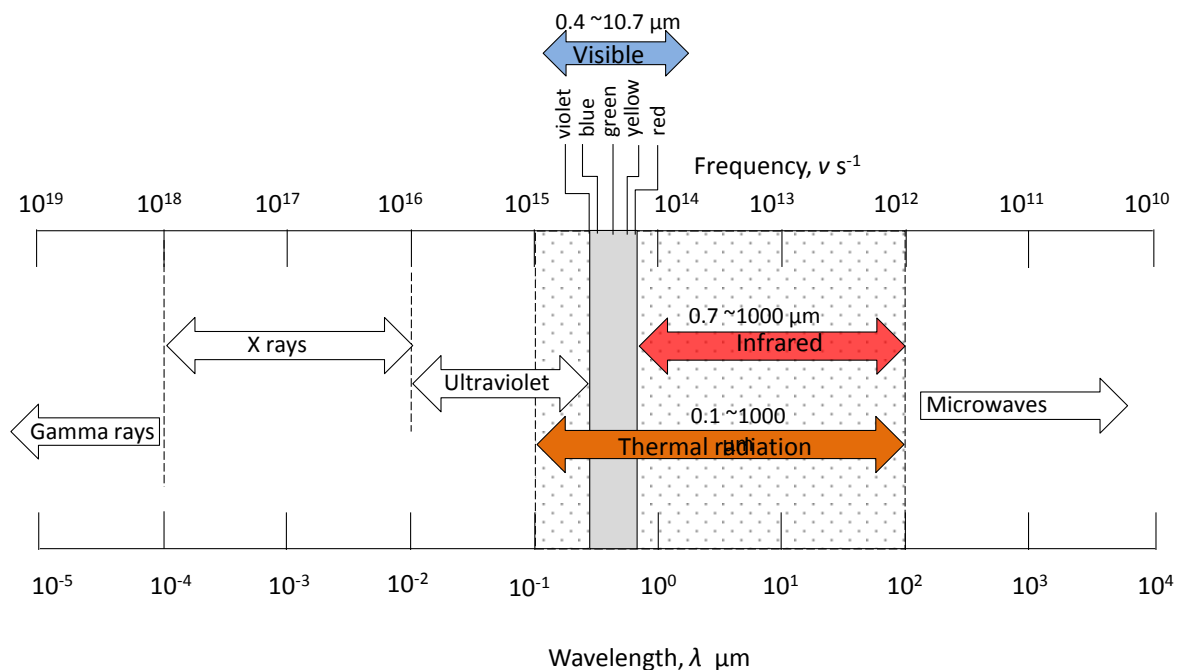


Fig. 4-1 Wavelength and frequency domains of thermal radiation and positions on the electromagnetic spectrum.

It was shown by the quantum arguments of Planck [2] and verified experimentally that for a blackbody the spectral distributions of hemispherical emissive power and radiant intensity in a vacuum are given as a function of the wavelength,  $\lambda$ , and the blackbody's absolute temperature,  $T$ , as follows:

$$E_{b\lambda}(\lambda, T) = \pi I_{b\lambda}(\lambda, T) = \frac{C_1}{\lambda^5 \{\exp(C_2 / \lambda T) - 1\}} \dots\dots\dots (1)$$

where  $I_{b\lambda}$  represents the intensity of blackbody thermal radiation;  $C_1 = 2\pi hc^2 = 3.742 \times 10^{-16}$  [W.m<sup>2</sup>],  $C_2 = hc/k = 1.439 \times 10^{-2}$  [m.K] where  $k$  is Boltzmann's constant ( $1.38 \times 10^{-23}$  J/K),  $h$  is Planck constant ( $6.625 \times 10^{-34}$  J.s), and  $c$  is speed of light in vacuum ( $3 \times 10^8$  m/s). The units of  $E_{b\lambda}$ , are W/m<sup>3</sup>; in other words, the energy per unit of time, wavelength and surface area.

Fig. 4-2 shows the hemispherical emissive power as a function of wavelength for several absolute temperatures. Total radiated energy at all wavelengths increases with temperature. Wien's displacement law states that the spectral radiance of blackbody radiation per unit wavelength [3], peaks at the wavelength  $\lambda_{max}$  given by

$$\lambda_{max} = b/T \dots\dots\dots (2)$$

where  $T$  is the absolute temperature in degrees Kelvin and  $b$  is a Wien's displacement constant, equal to  $2.898 \times 10^{-3}$  m K. It describes the locus of the  $E_{b\lambda}$  maximum, which on the logarithmic field of Fig. 4-2 is represented by a straight line. As the temperature increases, the bulk of the energy emitted by a blackbody shifts to progressively shorter wavelengths.

Total monochromatic emissive power  $E_{b\lambda}$  represents the heat flux that leaves a surface

area along all the rays per unit of wavelength interval. The total hemispherical emissive power of blackbody  $E_b$  is obtained by using the Stefan Boltzmann law [4], as below:

$$E_b(T) = \int_{\lambda} E_{b\lambda}(\lambda, T) d\lambda = \sigma T^4 \quad \dots\dots\dots (3)$$

where  $\sigma = 5.6697 \times 10^{-8} \text{ W}/(\text{m}^2 \cdot \text{K}^4)$  is the Stefan Boltzmann constant.

From equations (1) and (3), it can be seen that the total energy radiated from a surface depends closely on the temperature of that surface. By measuring the total energy radiated from the surface of an object, the temperature can be determined. The infrared radiation pyrometer functions based on this principle. A blackbody is an idealized physical body. A real object's surface normally emits power less than that of a blackbody. The emissive power is highly affected by the emissivity of the surface. The emissivity is defined as a ratio of the total emissive power of the surface to that of a blackbody at the same temperature. In the present study, the two-color pyrometer used is able to eliminate the influence of the emissivity of the object.

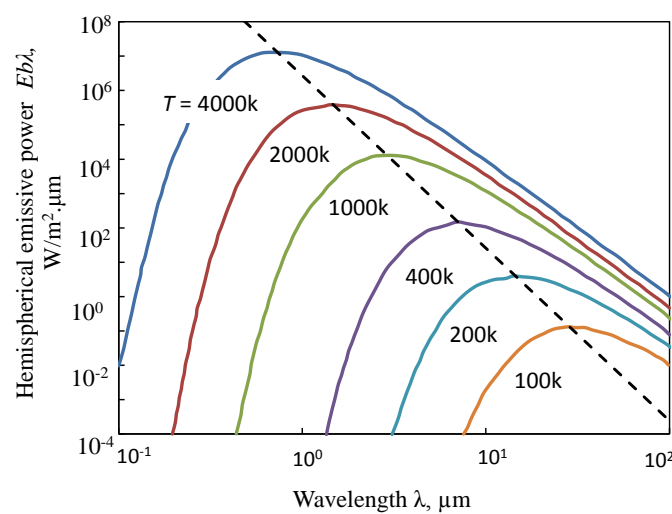


Fig. 4-2 Radiant energy of blackbody



### 4.3 FUNDAMENTALS OF THE TWO-COLOR PYROMETER

In this study, a two-color pyrometer with an optical fiber is used, as illustrated in Fig. 4-3. The infrared energy is transmitted through a chalcogenide optical fiber to the InSb and MCT detectors, which have different spectral sensitivities. The detectors are mounted in a sandwich configuration and kept at a temperature of about 77 K by using liquid nitrogen in order to maintain high sensitivity. The infrared energy is transformed to an electric signal by the detector and amplified by the amplifier circuits. The signal is observed and recorded by the use of a digital oscilloscope. The temperature is obtained by calculating the output voltage ratio from the detector cells.

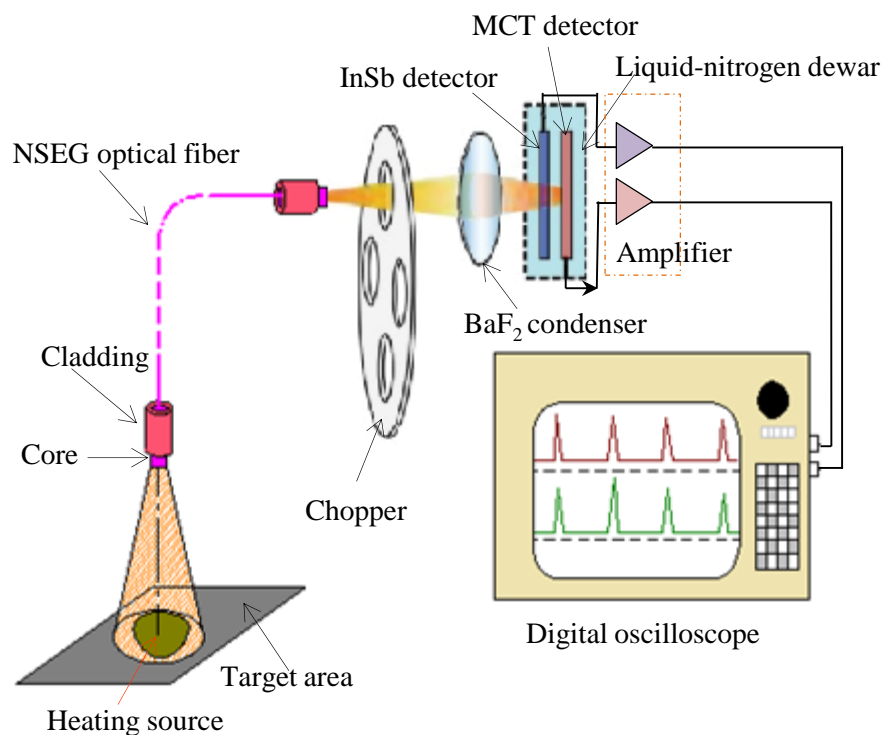


Fig. 4-3 Schematic diagram of two-color pyrometer with optical fiber [5]

## 4.4 TWO-COLOR PYROMETER COMPONENTS

The main components of the two-color pyrometer are: optical fiber, infrared detectors, amplifier, and condenser lens. The proper selection of optical fiber, infrared detector, and other components of the pyrometer is important, since these will directly affect the accuracy of the pyrometer.

### 4.4.1 Optical fiber

In this pyrometer system, the fiber type used is a multi-mode step-index NSEG chalcogenide optical fiber. Fig. 4-4 shows the structure of the step-index-type optical fiber. Because the core's index of refraction  $n_1$  is higher than the cladding's index of refraction  $n_2$ , the rays entering at less than the critical angle are guided along the fiber. The critical angle (minimum angle for total internal reflection) is determined by the difference in index of refraction between the core and cladding materials, and defined as follows:

$$\sin \phi_c = \frac{n_2}{n_1} \dots\dots\dots (4)$$

From the law of Snell, we get

$$n_0 \sin \zeta_m = n_1 \sin \left( \frac{\pi}{2} - \phi_c \right) \dots\dots\dots (5)$$

Rays that meet the boundary at a low angle are refracted from the core into the cladding, and do not convey light along the fiber. The critical angle determines the acceptance angle of the fiber, often reported as a numerical aperture. Numerical aperture (NA) is defined as follows, deriving from equations (4) and (5):

$$n_0 \sin \zeta_m = n_1 \left\{ 1 - \left( \frac{n_2}{n_1} \right)^2 \right\}^{\frac{1}{2}} = \sqrt{n_1^2 - n_2^2} = NA \quad \dots\dots\dots (6)$$

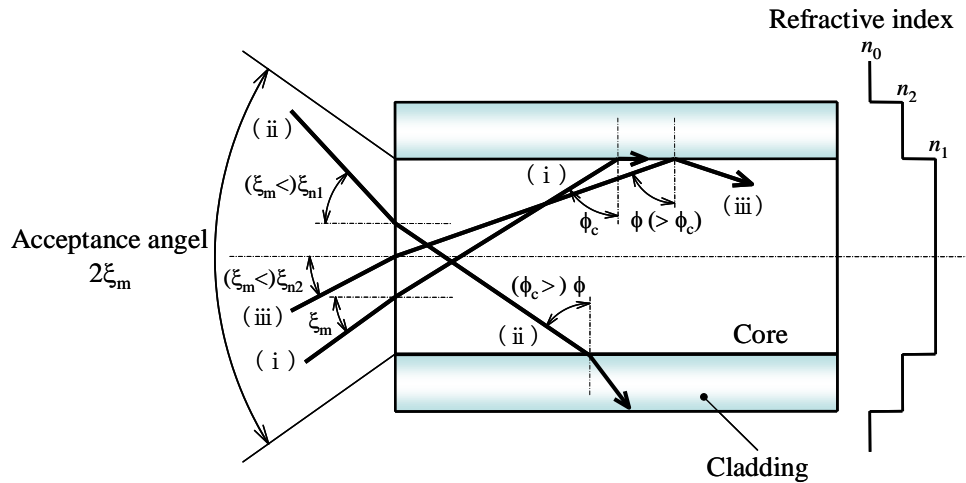


Fig. 4-4 Structure of step-type optical fiber

A high numerical aperture allows light to propagate down the fiber in rays both close to the axis and at various angles, allowing efficient coupling of light into the fiber. However, this high numerical aperture increases the amount of dispersion, as rays at different angles have different path lengths and therefore take different times to traverse the fiber. The ratio of

the change in the refractive index of the core and cladding is called a ‘relative refractive index difference’; it is given by the following equation:

$$\Delta = \left( \frac{n_1 - n_2}{n_1} \right) \dots\dots\dots (7)$$

The refractive index for the atmosphere is  $n_0=1$ ; therefore the maximum acceptance angle  $\xi_m$  of the optical fiber can be found as follows:

$$\xi_m = \sin^{-1}(NA) \dots\dots\dots (8)$$

Transmission loss often occurs during transfer of the infrared radiation signals. Factors generating transmission loss include fiber properties such as structural and chemical imperfections and fiber density fluctuations [6]. The physical conditions of the fiber also contribute to transmission loss, such as non-uniformity at the core-cladding boundary, curvature of the fiber paths, and surface condition at both ends of the optical fiber. Therefore, in this study the edge of the fiber is polished with #3000 abrasive papers to minimize the loss. Fig. 4-5 shows a wide range of wavelength of the NSEG chalcogenide optical fiber. Table 4-1 gives the characteristics of the NSEG chalcogenide glass fiber.

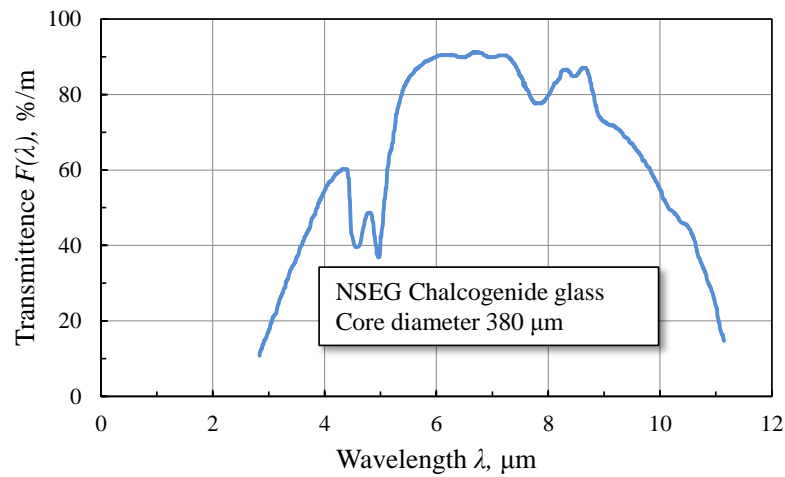


Fig. 4-5 Spectral transmittance of NSEG chalcogenide glass fiber

Table 4-1 Characteristics of NSEG optical fiber

Fiber type	NSEG
Core diameter, $d_c$	380 $\mu\text{m}$
Acceptance angle, $\xi_m$	30 $^\circ$
Numerical Aperture, $NA$	0.5
Wavelength range, $\lambda$	3 ~ 11 $\mu\text{m}$

Fig. 4-6 illustrates the measuring area at the incidence face of the optical fiber. The fiber is placed at a distance of  $t$  from the object;  $d_s$  is the diameter of the target area. Increasing the measuring distance will increase the diameter of the target area, as shown in Fig. 4-7. However, Ueda et al. [7] reported that the two-color pyrometer is not influenced by the measuring distance. In this study, the optical fiber was set at an angle of 45 degrees, since the laser is directed vertically from the top. Measuring distances were fixed at 3 mm, which

gave a diameter of the target area of approximately 4 mm (calculated vertically according to Fig. 4-6).

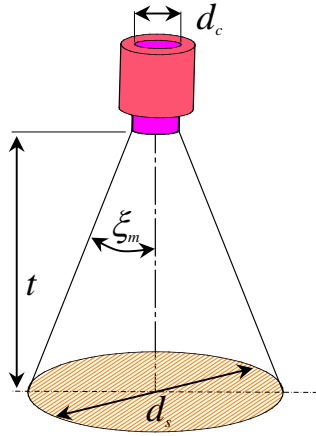


Fig. 4-6 Schematic illustration of measuring area

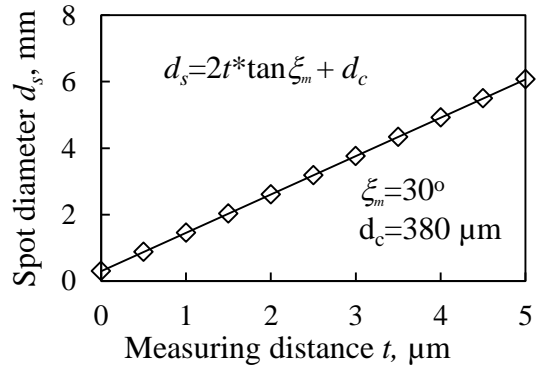


Fig. 4-7 Relationship between measuring diameter and spot diameter for NSEG optical fiber

#### 4.4.2 Infrared detector

In general, there are two main types of infrared detector available on the market: thermal detectors and photon detectors [8]. Thermal detectors convert radiated power into a more readily measured parameter, while photon detectors generally respond to incident radiation on an electronic level. The two-color pyrometer in this study uses the photon-type detectors.

The infrared detectors used in this study are Indium Antimode (InSb) and Mercury Cadmium Telluride (MCT) (Hamamatsu Photonics Co. Ltd). These detectors are mounted in

a sandwich configuration. The specifications of these detectors are shown in Table 4-2, and the spectral variation of specific detectivity,  $D^*$ , is shown in Fig.4-8.

Specific detectivity,  $D^*$ , is defined as a signal-to-noise ratio.  $D^*$  is given by

$$D^* = \frac{R\sqrt{A_D}}{N/\Delta f} = \frac{S\sqrt{\Delta f}}{N \cdot E_i \sqrt{A_D}} \dots\dots\dots (9)$$

where  $R$  is the responsivity, which is the ratio between the output signal and the radiant input, and  $A_D$  is the detector's active area ( $\text{mm}^2$ );  $N$  is the noise,  $\Delta f$  is the bandwidth frequency of the noise  $N$ ,  $S$  is the signal output (usually in electrical current, Amp), and  $E_i$  is the radiant input energy ( $\text{W}/\text{cm}^2$ ). The unit for  $D^*$  is  $\text{Hz}^{1/2}/\text{W}$ . A large  $D^*$  value is good, and for a given environment all good detectors should have about the same  $D^*$ .

As shown in Table 4-2, InSb and MCT have a spectral response range of 3.1~5.5  $\mu\text{m}$ , and 5.5~13.8  $\mu\text{m}$ , respectively. These cells are mounted in a sandwich configuration, with the InSb cell placed in the front of MCT. According to Planck's law, as the temperature of the source increases, the wavelength of infrared radiation, which gives off most of the energy, decreases.

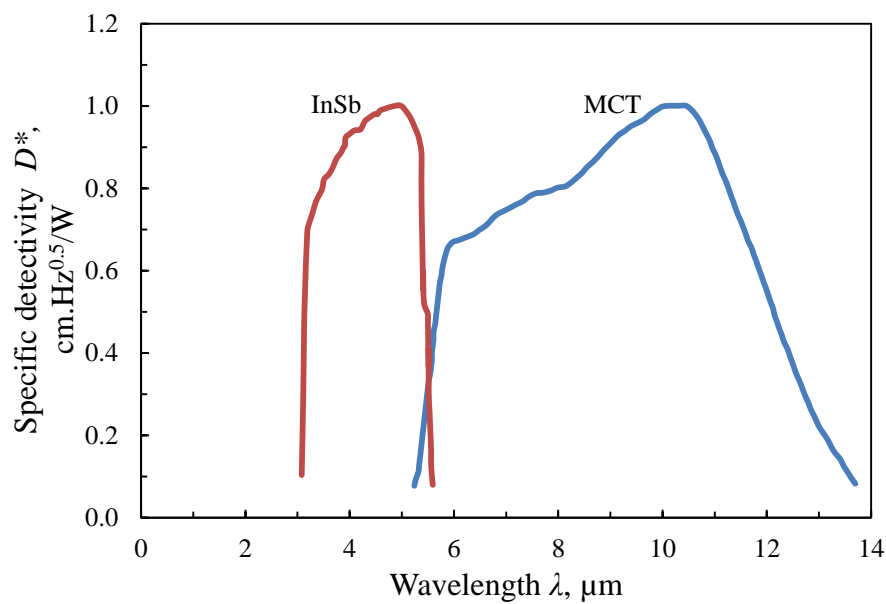


Fig. 4-8 Specific detectivity of InSb-MCT detector cell

Table 4-2 Specifications of detector cells

Detector cell	InSb	MCT	
Spectral response range*	3.1~5.5	5.5~13.8	$\mu\text{m}$
Peak detectivity wavelength	5.1	10	$\mu\text{m}$
Operating temperature	77	77	K
Specific detectivity $D^*$	$4 \times 10^{11}$	$2 \times 10^{10}$	$\text{cm.Hz}^{1/2}/\text{W}$

\*as photocell mounted in sandwich configuration,

### 4.4.3 Amplifier

This pyrometer uses the high response speed of the infrared detector to measure the laser-beam spot temperature. Therefore, the response performance of the conversion amplification circuit should be better than the response speed of the infrared detectors. The output current of the InSb detector (photovoltaic cells) is converted into voltage and amplified with the conversion amplification circuit, as shown in Fig. 4-9. Because the MCT



detector cell is a photoconductor cell, the resistance of the MCT cell is amplified using the amplifier, as shown in Fig. 4-10.

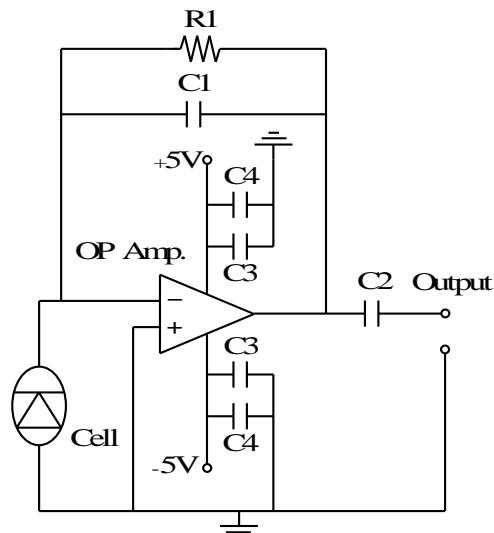


Fig. 4-9 Circuit diagram of amplifier for InSb cell [5]

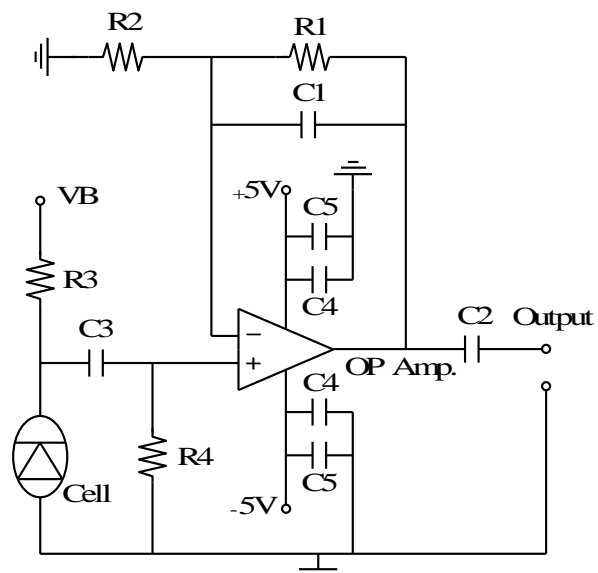


Fig. 4-10 Circuit diagram of amplifier for MCT cell [5]

#### 4.4.4 Condenser lens

A BaF<sub>2</sub> lens is used to condense the infrared radiation rays from the optical fiber into the infrared detector. The sensitivity wavelength ranges of InSb and MCT are 3.1~5.5  $\mu\text{m}$  and 5.5~13.8  $\mu\text{m}$ , respectively; for the optical fiber the transmission wavelength is between 3.5 and 11.5  $\mu\text{m}$ . Therefore, the BaF<sub>2</sub> lens is suitable in this pyrometer because it has a constant permeability at wavelength of 0.5~14.0  $\mu\text{m}$ , as shown in Fig. 4-11.

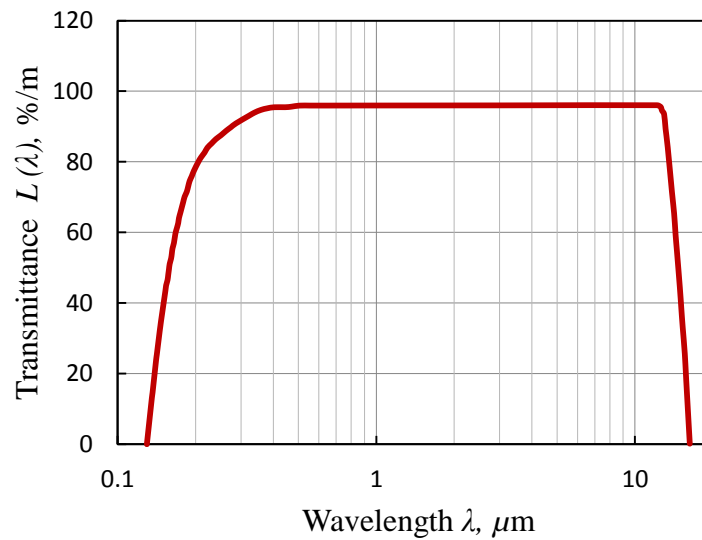


Fig. 4-11 Spectral transmittance of BaF<sub>2</sub> condenser lens

#### 4.4.5 Relative sensitivity of two-color pyrometer

The sensitivity of the two-color pyrometer is expressed theoretically by using the relative sensitivity of the InSb cell  $\Lambda_{\text{InSb}}$ , and MCT cell  $\Lambda_{\text{MCT}}$ . Relative sensitivity between InSb and MCT is defined as follows:

$$\Lambda_{InSb/MCT} = \frac{\Lambda_{InSb}}{\Lambda_{MCT}} = \frac{\int_{\lambda_2}^{\lambda_1} \omega_1 \varepsilon_1(\lambda, T) E_{b\lambda}(\lambda, T) F(\lambda) L(\lambda) D_{InSb}(\lambda) d\lambda}{\int_{\lambda_4}^{\lambda_3} \omega_2 \varepsilon_2(\lambda, T) E_{b\lambda}(\lambda, T) F(\lambda) L(\lambda) D_{MCT}(\lambda) d\lambda} \dots\dots\dots (10)$$

$E_{bl}(l, T)$  is spectral emissive power of a blackbody;  $E_1(l, T)$  and  $E_2(l, T)$  are the emissivity of the object;  $w_1$  and  $w_2$  are constants;  $F(\lambda)$  is the spectral transmittance of the optical fiber;  $L(\lambda)$  is the spectral transmittance of the condenser;  $D_{InSb}(\lambda)$  and  $D_{MCT}(\lambda)$  are spectral transmittance values of the detector cell; and  $\lambda_1$ - $\lambda_2$  and  $\lambda_3$ - $\lambda_4$  are measurable ranges in the pyrometer wavelength. The emissivity of the objects  $\varepsilon_1(\lambda, T)$  and  $\varepsilon_2(\lambda, T)$  are assumed to be equal, since the measurable wavelength range of the pyrometer is not very wide. Therefore, as verified experimentally in [9], the influence of the object's emissivity on the relative sensitivity of the two-color pyrometer can be ignored. The sensitivity of the pyrometer in practice is lower than in the ideal case, as indicated by Equation 10. This is due to the smaller radiant energy from the object compared to a blackbody, and the losses of incident energy transmitted by the fiber. By obtaining the information discussed above, the relative sensitivity curve of this pyrometer can be obtained.

A theoretically relative sensitivity curve of the two-color pyrometer can be obtained numerically by multiplying the values as described below, and integrated within the wavelength for each detector cell. This relative sensitivity curve will be used in making a calibration curve, which will be discussed in the following section.

- a) Blackbody radiation energy  $E_{bl}(\lambda, T)$  can be obtained from Planck's equation (1);

- b) Spectral transmittance of the NSEG chalcogenide optical fiber can be obtained from Fig. 5;
- c) Relative detectivity of InSb cell  $D_{InSb}(\lambda)$  and MCT cell  $D_{MCT}(\lambda)$  can be found from Fig. 8;
- d) Permeability of the BaF<sub>2</sub> lens condenser is obtained from Fig. 4-11.

## 4.5 CALIBRATION

The relationship between the relative sensitivity and temperature has been defined qualitatively by equation 10. In order to convert the output voltage ratio of the pyrometer into temperature, calibration curve should be obtained.

The experimental arrangement for calibration is illustrated schematically in Fig. 4-12. The specimen is heated by the electric current through the Kanthal wire (FeCrAl alloys). The specimen used in the calibration is silicon wafer, as the material used in this study. In order to measure the temperature of the specimen during the calibration, thermocouple (JIS-K type) wire is fixed on the specimen. A monolithic refractory (ISOTAP F-12) consisting of ceramic fiber and insulating aggregate is used to cover the specimen and Kanthal wire to prevent heat loss. The measuring distance is fixed at 5 mm. The infrared rays emitted from the specimen and accepted by the optical fiber lead to the detector cells. A chopper is used since the infrared rays radiated from the sample are almost constant. The infrared rays are then converted to electric signals by the detector, and afterward amplified before being observed and recorded using a digital oscilloscope.

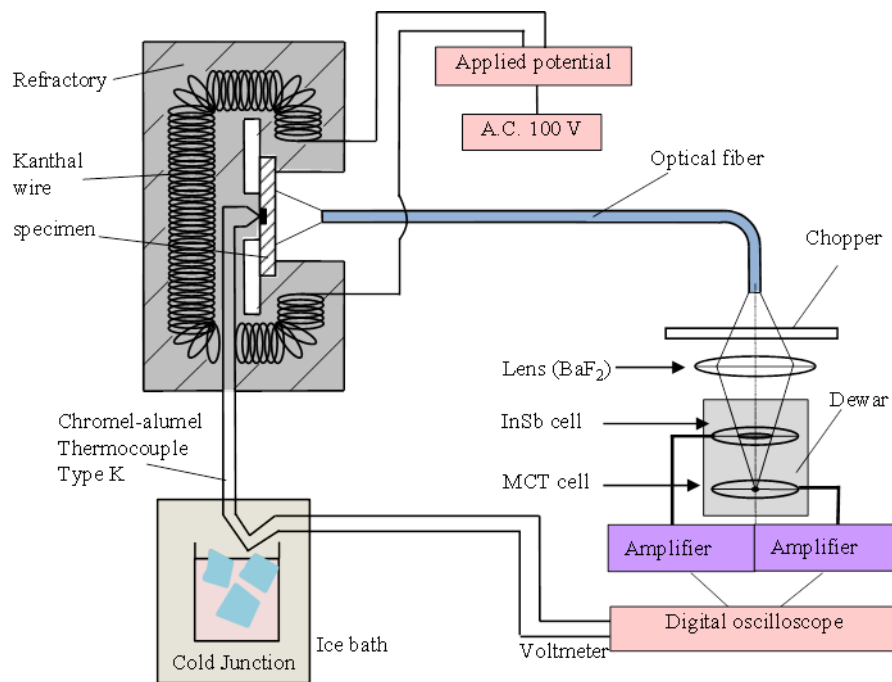


Fig. 4-12 Schematic illustration of temperature calibration

The relationship between the output voltages of the InSb and MCT detector cells is presented in Fig. 4-13. Fig. 4-14 shows the calibration curve between temperature and the output voltage ratio of InSb/MCT. The theoretical curves are the relative sensitivity calculated from equation 10. From these figures, it can be seen that the experimental points coincide well with the calculated theoretical curves. Hence, the calibration curve is suitable for temperature measurement. Furthermore, the pyrometer is capable of measuring temperatures from 150°C to 700°C.

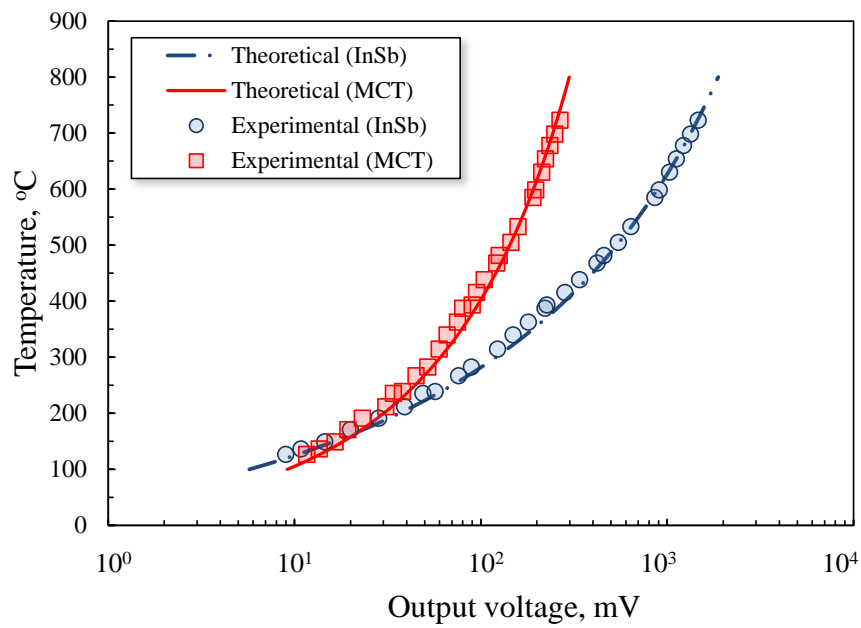


Fig. 4-13 Relationship between output voltage from pyrometer and temperature

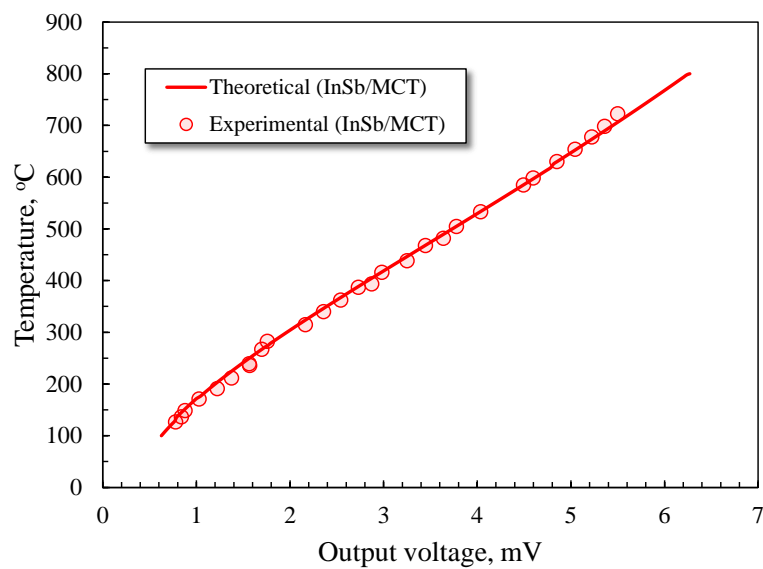


Fig. 4-14 Relationship between temperature and output voltage ratio from pyrometer

## 4.6 CONCLUSIONS

In this chapter, the two-color pyrometer system and its basic principle have been introduced. This pyrometer uses the advantages of NSEG chalcogenide optical fiber in accepting infrared radiation from the heated area, and then transferred it to the InSb and MCT detectors. Temperatures are obtained by calculating the ratio of the output voltage from these detectors. An accurate calibration curve of the pyrometer is obtained, and is available for a quantitative measurement of temperature. The influence of the object's emissivity can be neglected, as the temperature is obtained from the output voltage ratio. Calibration curves show that the two-color pyrometer has a good degree of accuracy in measuring temperature.

## REFERENCES

- [1] W. J. Yang, N. Zhang, B.-X. Wang, J. Yang, "A Study on Metal Melting Process by Laser Heating," *Heat and Mass Transfer in Materials Processing* (edited by Tanasawa, L. and Lior, N.), Hemisphere Publishing Corporation, New York, pp. 53-63, 1992.
- [2] M. Planck, "Distribution of energy in the spectrum," *Ann. Phys.*, 4(3): 553-563, 1901.
- [3] W. Wien, "Temperatur und Entropie der Strahlung," *Ann. Phys.*, 52(2): 132-165, 1894.
- [4] L. Boltzmann, "Ableitung des stefan'schen Gesetzes betreffend der Abhangigkeit der Waermestrahlung von der Temperatur aus der electromagnetischen Lichttheorie," *Ann. Phys.*, 22(3): 291-294, 1884.
- [5] A. Yassin, *Experimental study on machinability of laser-sintered material in ball end milling*, PhD Dissertation, Kanazawa University, 2008.
- [6] T. Okoshi, *Optical fiber*, New York: Academic Press, 1982.
- [7] T. Ueda, A. Hosokawa, K. Oda, and K. Yamada, "Temperature on flank face of cutting tool in high speed milling," *CIRP Annals - Manufacturing Technology*, 50(1): 37, 2001.
- [8] J. D. Vincent, *Fundamental of infrared detector operation and testing*, New York: John Wiley & Sons, 1989.
- [9] T. Ueda, M. Sato, and T. Sugita, "Measurement of tool-workpiece interface temperature by two-color pyrometer," *Seimitsu Kogaku Kaishi/Journal of the Japan Society for Precision Engineering*, 61(10): 1448, 1995.



## **CHAPTER 5: INVESTIGATION OF THERMAL-STRESS CLEAVING WITH SINGLE-POINT LASER**

### **5.1 INTRODUCTION**

This chapter reports on the use of a single-point laser beam to generate thermal stress on a silicon-wafer specimen to cause a fracture leading to separation. Separation performance was determined by measuring the laser irradiation temperature and fracture occurrences through experimental works. A computational analysis by the finite-element method (FEM) was used to investigate the thermal-stress condition inside the wafer.

A silicon wafer with different types of initial crack was evaluated in terms of separation performance by observing the temperature at which separation occurred, i.e., cleaving temperature and cleaving time. The silicon-wafer specimens were prepared with two different kinds of initial crack, namely micro-crack and micro-groove. These initial cracks were made on the leading edge of the specimens. The temperature of the laser spot was measured by using a two-color pyrometer with an optical fiber, and the AE signal was assessed to observe the time taken for fracture occurrences. Additionally, the influences of laser distances on the initial crack were investigated.

During the laser irradiation, thermal stress was induced in the silicon-wafer material. The finite-element method (FEM) was applied using the ANSYS simulation software to seek to understand the thermal-stress condition inside the wafer. The analysis was performed in two stages: transient temperature analysis was performed to simulate the laser irradiation on the silicon wafer; then, steady-state stress analysis was performed using the temperature distribution results at a particular point in time.

## **5.2 EXPERIMENTAL METHODOLOGY**

### **5.2.1 Preparation of silicon-wafer specimen**

In this experiment, a single-crystal silicon wafer with crystal (100) orientation and thickness of 0.5 mm was used. Fig. 5-1 shows the image of the crystal (100) orientation silicon wafer with a diameter of 125 mm and a thickness of 0.5 mm. The specimen was cut away from the wafer with diamond scribing and mechanical snapping to the required dimensions referring to a flat orientation surface. The specimen size used in the experiment was 20 mm x 10 mm x 0.5 mm. The specifications of the silicon wafer used in this analysis are summarized in Table 5-1.

The wafer specimens were prepared with two types of initial crack on the edge of the silicon wafer, namely micro-crack and micro-groove. The micro-crack was produced by applying Vickers indenter impressions, whereas the micro-groove was created by focusing the pulsed laser beam through the micro-lens [1]. The SEM images of micro-crack and

micro-groove are shown in Fig. 5-2 and Fig. 5-3, respectively. A blunt notch was generated on the micro-groove, and a sharp end was produced at the micro-crack.

### 5.2.2 Experimental procedure

Fig. 5.4 shows the experimental set-up for the thermal-stress cleaving using laser-beam irradiation. A continuous-wave Nd:YAG laser was irradiated at a distance of 1.5 mm from the edge. The oval beam spot with major axis length of 0.25 mm and minor axis length of 0.19 mm was defocused on the wafer's surface. Irradiation time was set constant at 250 ms, and laser power was varied between 50 W and 70 W. A summary of the experimental conditions is shown in Table 5-2.

Temperature of the laser spot was measured using a two-color pyrometer with an optical fiber, developed by Ueda et al. [2]. The NSEG chalcogenide optical fiber was set at a distance of 3 mm from the laser spot and at an angle of 45° from the optical axis. The infrared energy radiated from the object was captured by the fiber and transmitted to a two-color pyrometer consisting of InSb and MCT detectors. This optical fiber can transmit infrared wavelength from 3  $\mu\text{m}$  to 11  $\mu\text{m}$ , so the 1.06  $\mu\text{m}$  wavelength from YAG laser was filtered. The infrared energy was converted to an amplified electric signal. By calculating the ratio of output voltages from these two detectors, the temperature of an object can be obtained using the calibration curve. Fracture initiation was monitored by an acoustic emission (AE) sensor mounted on the wafer surface. An AE sensor was fixed on the wafer's surface at a distance of 5 mm from the micro-groove. Details of the AE signal measurement system are summarized in Table 5-3.

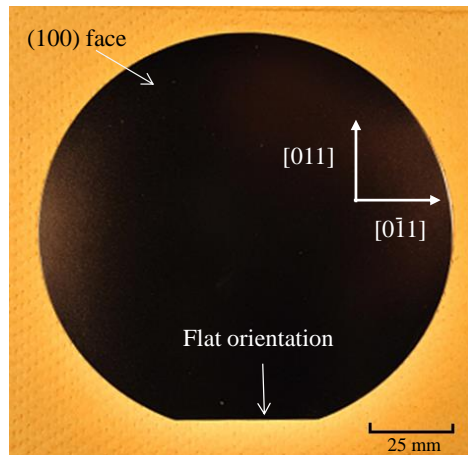


Fig. 5-1 Silicon wafer with (100)-crystal plane

Table 5-1 Specifications of silicon wafer

Silicon wafer	P-type polished wafer	Units
Crystal plane	(100)	
Manufacturing method	Czochralski process	
Manufacturer	SUMCO	
Diameter, $D$	125	mm
Thickness, $t$	0.5	mm
Thermal conductivity, $K$	156	W/m·K
Specific heat, $C$	761	J/kg·K
Density, $\rho$	2340	kg/m <sup>3</sup>
Thermal expansion coef., $\alpha$	$2.62 \times 10^{-6}$	K <sup>-1</sup>
Young modulus, $E$	169	GPa
Poisson ratio, $\nu$	0.262	

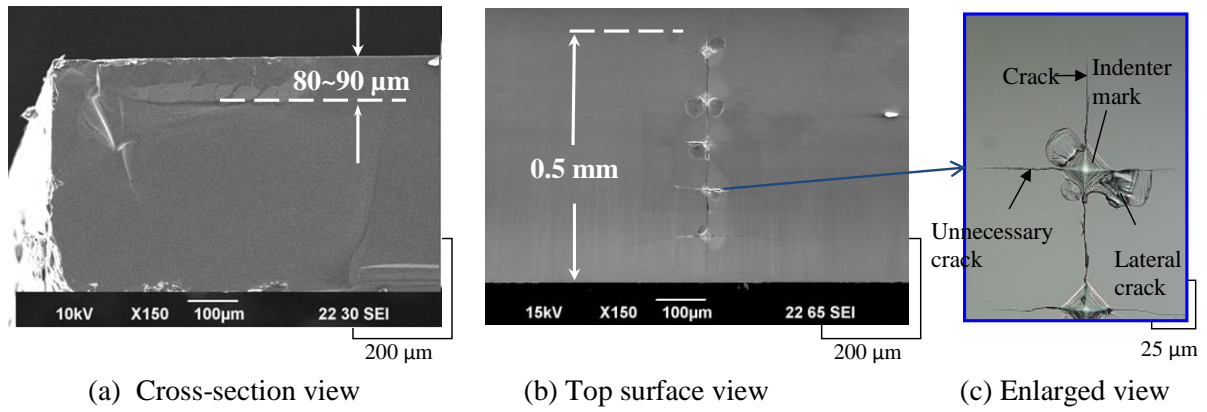


Fig. 5-2 Micro-crack on edge of wafer specimen produced by Vickers indenter

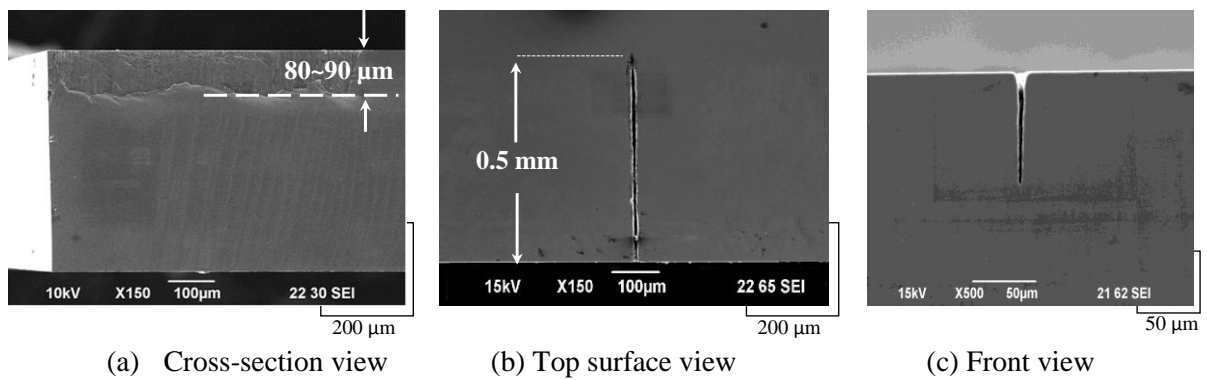


Fig. 5-3 Micro-groove on edge of wafer specimen produced by laser evaporative

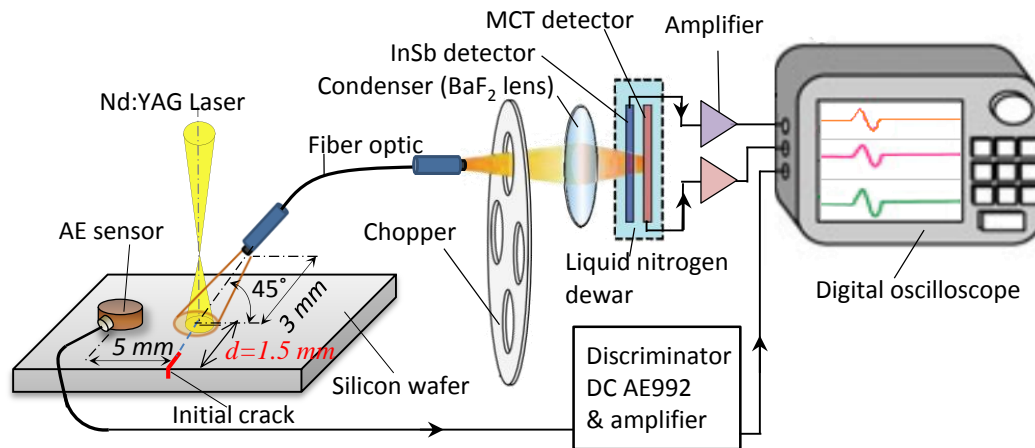


Fig. 5-4 Schematic illustration of experimental set-up with fundamental structure of two-color pyrometer and AE sensor

Table 5-2 Experimental conditions

Laser	Nd:YAG	Units
Wavelength, $\lambda$	1064	
Irradiation mode	Continuous wave	
Laser power, $P$	50 ~ 70	W
Laser beam diameter, $D$	0.25x0.19	mm <sup>2</sup>
Laser beam position, $d$	1.5	mm
Irradiation time, $t$	0.25	s
Work piece	Silicon wafer	
Size	10x20x0.5	mm <sup>3</sup>
Initial fracture	Micro crack, Micro-groove	
Crack length	0.5	mm
Pyrometer	Two-color	
Optical fiber	NSEG Ø380 $\mu$ m	
Detector	InSb/ MCT	

Table 5-3 Measuring system of AE signal

Acoustis Emission (AE) sensor		Units
Size	Ø5 x 3.2	mm
Frequency band (-10dB)	1 ~ 4	MHz
PreAmplifier		
Gain	40	dB
Frequency band (-10dB)	0.1 ~ 20	MHz

## 5.3 EXPERIMENTAL RESULTS AND DISCUSSION

### 5.3.1 Output signal from the pyrometer and the AE sensor

The typical output signals from the pyrometer and AE sensor and the temperature history of the experiment with laser power of  $P=70$  W are shown in Fig. 5-5. Fig. 5-5(a) and Fig. 5-5(b) represent the output voltages of the InSb and MCT detectors, while Fig. 5-5(c) displays the temperature history of the laser spot. Fig. 5-5(d) shows the signal from the AE sensor. The temperature was obtained by calculating the voltage ratio of the InSb/MCT detectors. When a laser beam was irradiated onto the wafer surface, the temperature increased gradually up to the end of the radiation time at 250 ms before decreasing rapidly.

As the fracture was initiated in the wafer material, AE signal appeared on the digital oscilloscope as shown in Fig. 5-5(d). Cleaving time was measured from the start of laser irradiation. Cleaving temperature was determined at the time of fracture occurrence, while maximum temperature was calculated at the end of laser irradiation,  $t=250$  ms.

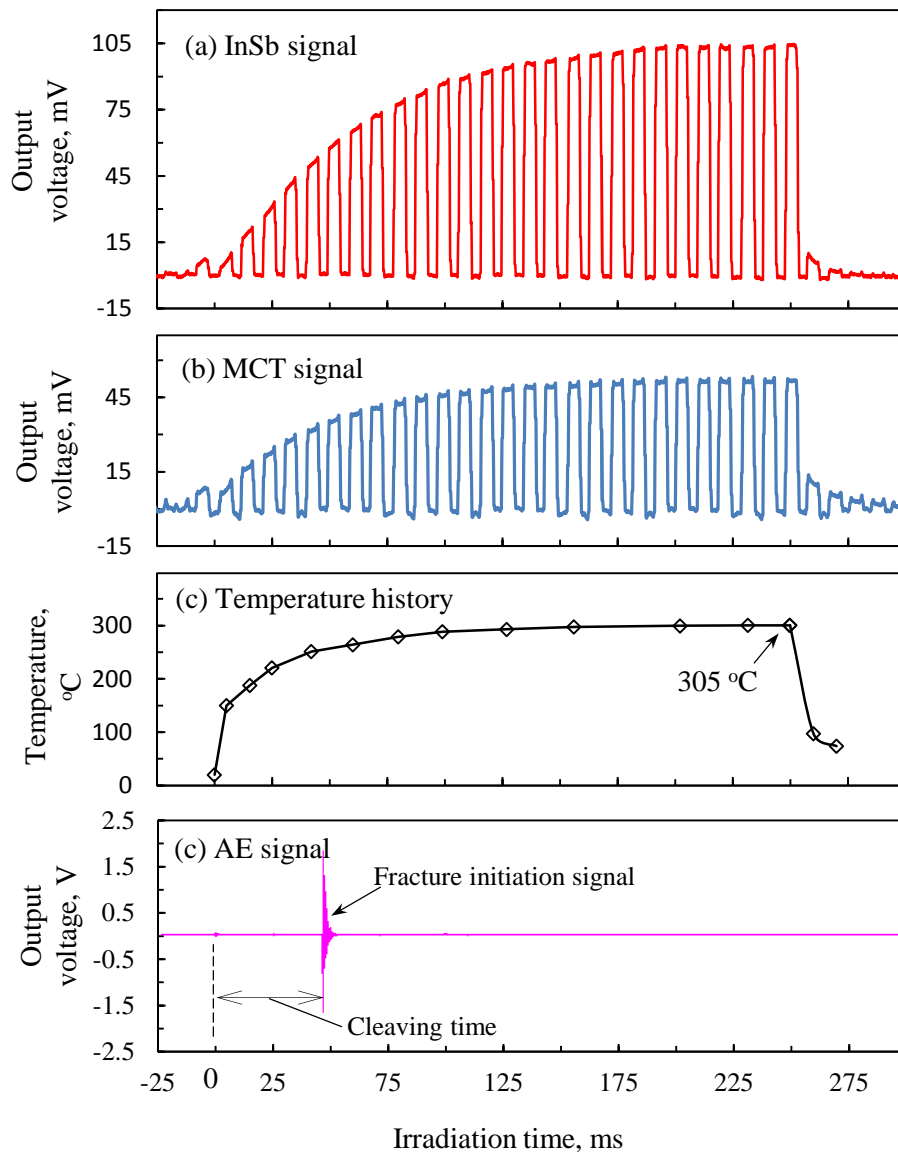


Fig. 5-5 Output signal of pyrometer detectors, temperature history and AE sensor ( $P=70$  W)



### 5.3.2 Temperature measurement

The temperature has been analyzed in two situations: first at the maximum temperature at the end of irradiation,  $t=250$  ms, and second at the time of cleaving or fracture occurrence by observing the AE occasion. The relationships between the temperatures at the laser spot and the laser power for the specimens with micro-crack and micro-groove are shown in Fig. 5-6 and Fig. 5-7, respectively.

From Fig. 5-6, we can see that, for the specimen with the micro-crack, the maximum temperature at the end of laser irradiation time,  $t=250$  ms, had increased proportionally to the laser power. For instance, the maximum temperature obtained at the laser powers of 55 W and 70 W were about 240°C and 305°C, respectively. However, the cleaving temperature, which was measured at time of fracture, was constant. The average cleaving temperature obtained was about 210°C.

Meanwhile, the maximum temperature attained for the specimen with the micro-groove, shown in Fig. 5-7, shows a similar trend to the results displayed in Fig. 5-6. For instance, the maximum temperature at a laser power of 70 W was about 300°C, while for laser power of 55 W the temperature was about 240°C. However, the average cleaving temperature was higher, approximately 230°C.

The results indicate that the maximum temperature reached at the end of irradiation was almost the same for both cases. This is because the sizes of the micro-crack and micro-groove were small and did not affect the temperature distribution during the laser-beam irradiation. Furthermore, the laser beam remained in the fixed position throughout the irradiation time.

In the meantime, fracture initiation occurred at a constant temperature. The critical temperatures for fracture initiation in the specimens with micro-crack and micro-groove were found to be approximately 210°C and 230°C, respectively. At these temperatures, the thermal stress generated at the initial crack tip was high enough to lead the fracture. However, if the laser power is too low, the critical temperature for cleaving is not achieved. Therefore, the fracture initiation cannot succeed.

The results show that the critical temperature for the micro-groove was higher compared to the micro-crack. Temperature induced via laser energy generates the thermal stress. During laser-beam irradiation at the same laser power, greater stress concentration resulted on the sharper crack tip [3]. However, as the micro-groove had a blunt tip/notch, in contrast to the sharp end of the micro-crack, higher temperature was required for fracture.

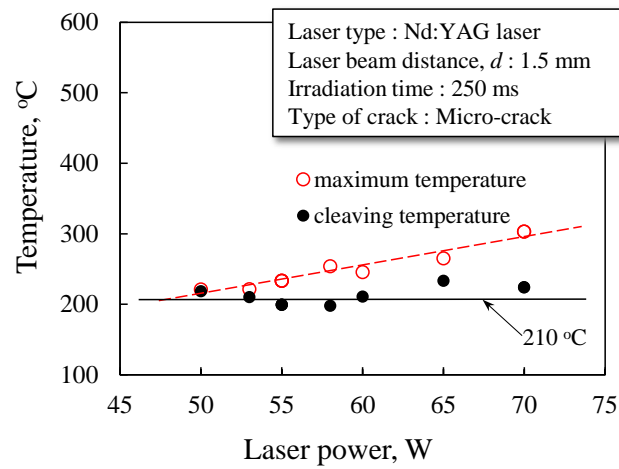


Fig. 5-6 Relationships between temperature and laser power for the specimen with micro-crack

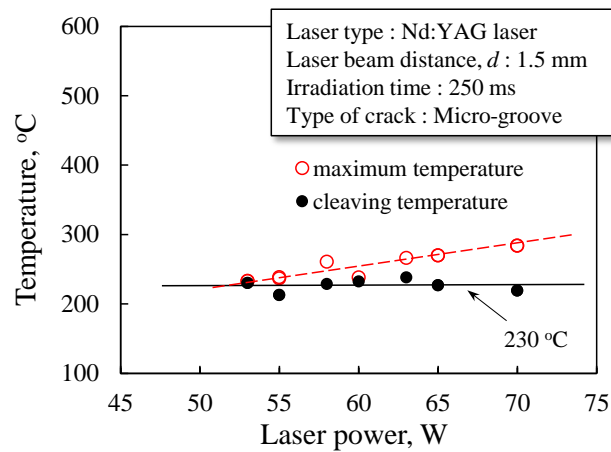


Fig. 5-7 Relationships between temperature and laser power for the specimen with micro-groove

### 5.3.3 Cleaving time

Fig. 5-8 shows the relationships between cleaving time and laser power for the specimen with micro-crack. The result shows that the time for a fracture to initiate is shortened as the irradiated laser power is increased. For instance, the cleaving times attained for laser powers of 55 W and 70 W were approximately 40 ms and 25 ms, respectively. Moreover, at the lower laser power of 50 W, the cleaving was successfully achieved at 220 ms.

Fig. 5-9 shows the relationships between cleaving time and laser power for the specimen with micro-groove. The results are similar to those for micro-crack, where the cleaving time is shortened as the irradiated laser power is increased. However, the cleaving times attained were longer in comparison with those achieved with micro-crack. For example, the cleaving times attained for laser powers of 55 W and 70 W were about 80 ms and 50 ms, respectively. Furthermore, fracture was not successful at a laser power of 50 W.

Thermal stress was generated by heat induced via laser energy. During laser-beam irradiation, temperature was gradually increased. The results shown in Fig. 5-6 and Fig. 5-7 reveal that critical cleaving temperature for the specimen with micro-groove was higher than for the specimen with micro-crack. Therefore, the cleaving time was longer for the specimen with micro-groove. At the laser power of 50 W, the critical cleaving temperature was not achieved at all, and fracture did not occur.

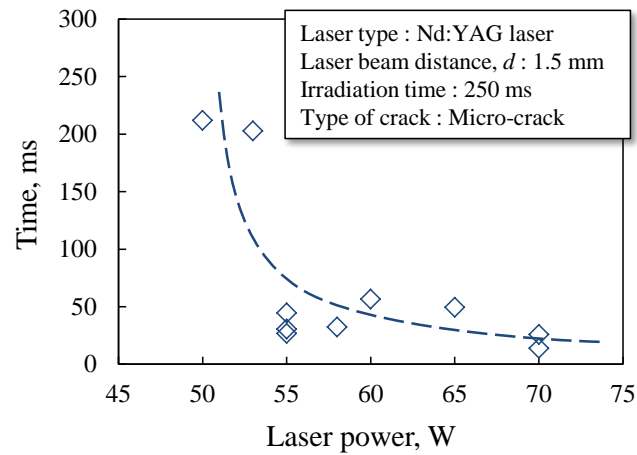


Fig. 5-8 Relationships between cleaving time and laser power for the specimen with micro-crack

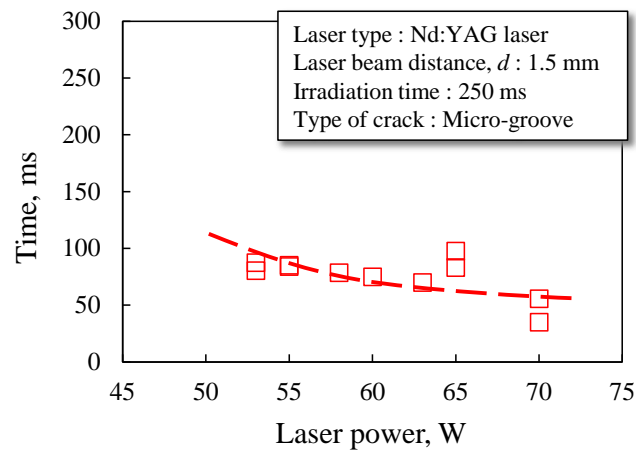


Fig. 5-9 Relationships between cleaving time and laser power for the specimen with micro-groove

#### 5.3.4 The influence of laser position on fracture extension

In this section, the influence of laser-beam positions on fracture extension is investigated. As shown in Fig. 5-4, the distance of the laser beam from the leading edge of the wafer is described as  $d$ . The positions of the beam were varied between 1 mm, 1.5 mm and 1.75 mm. The Nd:YAG laser was irradiated for 250 ms. After the irradiation had been completed, the specimens were divided by mechanical breaking. The separating surfaces were observed using a scanning electron microscope (SEM).

Fig. 5-10 shows the separating surface of the specimens. It is found that the extent of the cleaving surface increases in proportion to the laser distance,  $d$ , as summarized in Fig. 5-11. The result demonstrates that fracture occurrence created a separating (cleaving) surface and stopped at a distance from the laser-beam position.

During laser-beam irradiation, the heat generates thermal stress inside the wafer material. The thermal stress on the cleaving plane was divided into two regions, compressive and tensile. The fracture was started from the leading edge (groove tip) of the wafer and extended to the end of the tensile region on the cleaving plane. The fracture extension separated the wafer and created a cleaving surface. The tensile region increased with increased laser-beam position. The cleaving-surface occurrences shown in Fig. 5-10 are consistent with the results of the FEM analysis, shown in the next section.

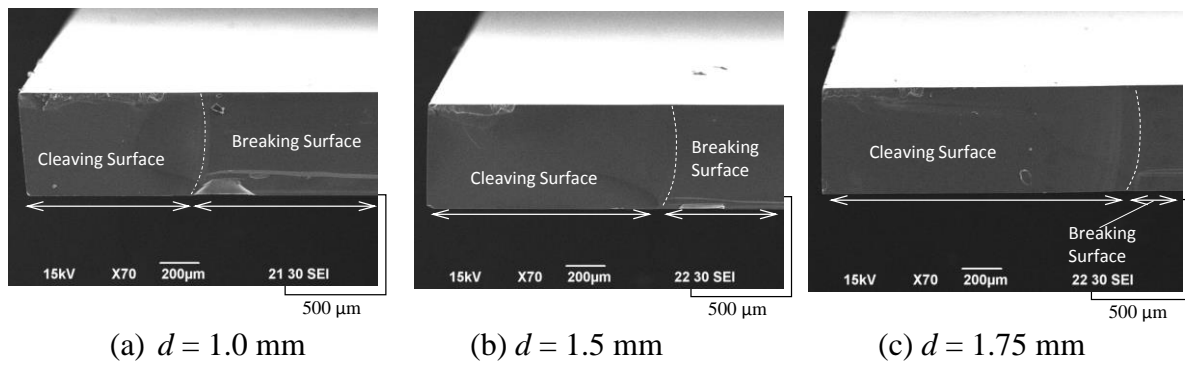


Fig. 5-10 Separating surface of the specimens at different laser positions,  $d$

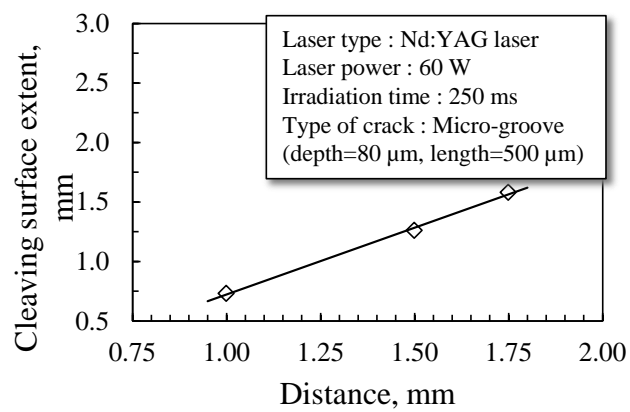


Fig. 5-11 Relationship between cleaving surface and laser-beam position

## 5.4 FINITE-ELEMENT ANALYSIS

In this section, computational analysis was performed to understand the actual phenomenon of thermal stress during laser irradiation. The temperature and AE signal of fracture behavior have been monitored before in experimental work. However, the mechanisms of fracture were not recognized and there is therefore a need to study the thermal-stress distribution with application of computer analysis.

A finite-element software, ANSYS, was used to analyze the behavior of thermal-stress cleaving during laser irradiation by considering the finite-boundary effect. The temperature and thermal-stress distribution around the laser spot diverged along the thickness direction of the substrate. Therefore, the finite-element model should be considered as a three-dimensional problem.

The specimen size used in this study was 20 mm x 10 mm x 0.5 mm. The half-part of the specimen with a coordinate system is shown in Fig. 5.12. The micro-groove, with dimensions of 80  $\mu\text{m}$  in depth and 500  $\mu\text{m}$  in length, was located at the position  $x=0$ ,  $y=0$ ,  $z=0$ ; while the volumetric laser-beam model in this analysis was fixed at  $x=1.5$  mm,  $y=0$ .

### 5.4.1 Absorption characteristic

The most common form of laser absorbing can be divided into surface absorption and volumetric absorption. Typical surface absorption occurs when the laser transmittance through the medium is almost zero; volumetric absorption occurs when some of the laser intensity is transmitted through the medium. The spectral transmittance correlates to the wavelength of the laser and the medium material. Fig. 5-13 shows the spectral transmittance



of the silicon wafer (100) measured by using Spectrum One DTS-Perkin Almer. Measurement of the spectral transmittance indicated that 23% of the laser intensity was transmitted through the silicon wafer. The reflection percentage of the laser energy on the material surface was assumed to be about 34%. The laser beam used was a Nd:YAG laser with a wavelength of 1.064  $\mu\text{m}$ ; the material used was a silicon wafer with (100)-crystal orientation, 0.5 mm in thickness.

Absorption of the Nd:YAG laser was determined by making use of a derivation of the Beer-Lambert law, which indicated that the laser intensity varied exponentially as it propagated in the medium. The absorption is represented by the Beer-Lambert equation below [4]:

$$\beta = \frac{-\ln T}{x} \quad (1)$$

where  $T$  is the spectral transmittance,  $\beta$  is the absorption coefficient and  $x$  is the thickness of the wafer. By using the above equation, the laser energy absorption relative to the thickness of the material can be found. Fig. 5-14 illustrates the absorption of laser energy while Fig. 5-15 shows the variation of laser energy absorption along the thickness direction of the material.

#### 5.4.2 Basic assumption on boundary conditions and material properties

Finite-element analysis (FEA) is a method to simulate heat source and boundary conditions in the model and determine the model's response to those conditions. The specimen from the experiment is modeled using discrete elements and nodes. Each element is composed of approximate equations that describe the element's response to a loading of the

heat source. The response of all the elements in the model provides the total response of the specimen in the real situation.

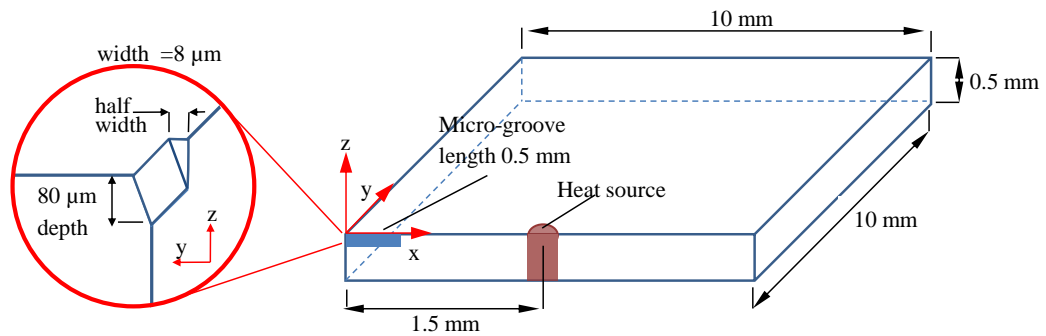


Fig. 5-12 Cross-section of the specimen with a coordinate

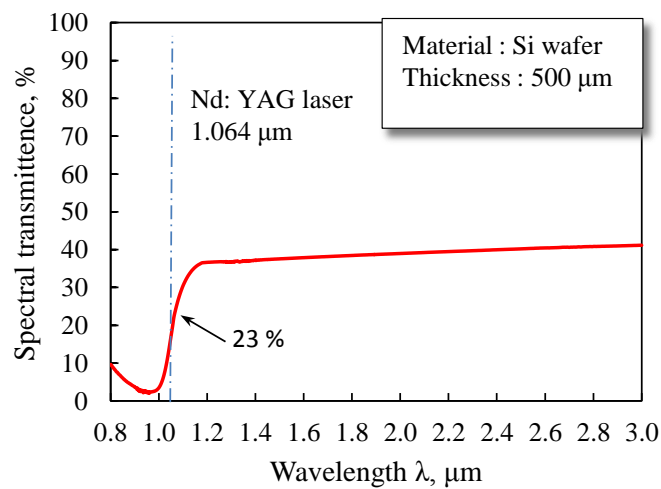


Fig. 5-13 Spectral transmittance of silicon wafer (100) with a thickness of 0.5 mm

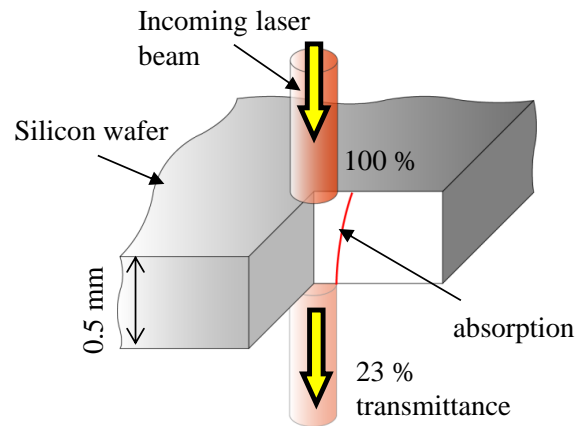


Fig. 5-14 Absorption characteristic of laser energy

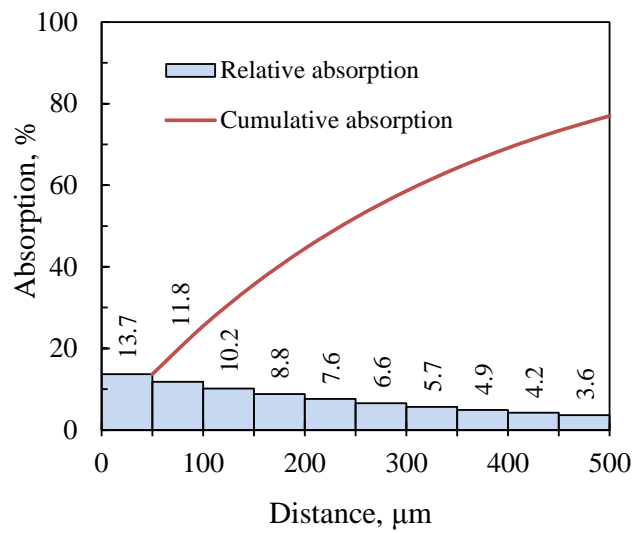


Fig. 5-15 Relationship between laser energy absorption and distance from the irradiation surface

Thermal-stress analysis was performed to investigate the effect of laser irradiation on the wafer. The analysis was divided into two stages. Transient thermal analysis was done to analyze temperature distribution on the wafer, and static structural analysis was performed to analyze stress distribution based on the loading from the thermal analysis. Because the temperature ranges in this study are small, the material properties are assumed to be constant and not dependent on temperature. The stress-strain relationship of the silicon wafer is considered perfectly elastic. Table 5-4 shows the thermal physical properties of the silicon wafer.

The temperature field  $T(x,y,z,t)$  is calculated by using the transient solution procedure. The governing equation in terms of temperature can be expressed by the heat diffusion equation [5]:

$$k\left(\frac{\partial^2 T}{\partial x^2} + \frac{\partial^2 T}{\partial y^2} + \frac{\partial^2 T}{\partial z^2}\right) + Q = \rho c \frac{\partial T}{\partial t}, \quad \dots (2)$$

where  $k$  is the thermal conductivity,  $\rho$  is the density,  $c$  is the specific heat, and  $Q$  is the laser power generation per unit volume. The initial condition is assumed to be uniform everywhere in the substrate, as described in equation 3. Convection conditions are considered to exist on all boundaries except the surface  $x$ - $z$  plane ( $y=0$ ). This surface is considered to be in adiabatic condition, which means no occurrence of heat transfer across the surface. Equations 4 and 5 describe the boundary conditions for the adiabatic conditions on the  $x$ - $z$  plane and the other convection boundaries, respectively.

Table 5-4 Thermal physical properties of silicon wafer (100)

Silicon wafer properties		units
Thermal conductivity, $K$	156	W/m.K
Specific heat, $C$	761	J/kg.K
Thermal expansion coef., $\alpha$	$2.62 \times 10^{-6}$	$K^{-1}$
Young modulus, $E$	169	GPa
Poisson ratio, $\nu$	0.262	
Density, $\rho$	2340	$kg/m^3$

$$T(x, y, z, 0) = T_0, \quad \dots (3)$$

$$k \frac{\partial T}{\partial n} = 0, \quad \dots (4)$$

$$k \frac{\partial T}{\partial n} + h(T - T_\infty) = 0 \quad \dots (5)$$

where  $h$  is the convection heat-transfer coefficient and  $n$  is the direction cosine of the boundary. The natural convection heat-transfer coefficient was set as  $8 \text{ W/m}^2\text{K}$  for all boundaries. During the process of laser cleaving, rapid heating induces thermal stress. The thermal stress  $\sigma_{therm}$  caused by the different temperature,  $\Delta T$ , is given by [6]:

$$\sigma_{therm} = \frac{E\beta\Delta T}{1 - \nu} \quad \dots (5)$$

where  $E$  is the Young's modulus, and  $\beta$  and  $\nu$  are the coefficient of linear expansion and Poisson ratio, respectively. The boundary of the stress analysis is traction-force free at all surfaces except the  $x$ - $z$  surface, which is set to a fixed plane where the displacement in the  $y$ -direction is zero.

### 5.4.3 FEM analysis result

In this analysis, the finite-element model was prepared with the micro-groove with the dimensions 0.5 mm in length, 80  $\mu\text{m}$  in depth and 7  $\mu\text{m}$  in width. The laser beam as the heat source was set at a position 1.5 mm from the wafer's leading edge. Laser power used was 70 W and the irradiation time was set at 0.25 seconds. Initial temperature and convection heat transfer were set at 20°C and 8 W/m<sup>2</sup>K, respectively. The dimension and coordinate system of the model followed Fig. 5.12. A summary of analysis conditions is shown in Table 5.5.

Fig. 5.16 shows the finite-element model with meshing element of 21,900 nodes in total. The meshing model used SOLID90 tetrahedron elements for thermal analysis. For structural analysis, the element type was changed to SOLID87. During structural analysis the structural displacement was set as equal to zero on the surface on the  $x$ - $z$  plane as an indication of a symmetric model.

#### (a) Temperature analysis result

Fig. 5.17 shows the result of temperature distribution from the ANSYS analysis with irradiation time of 50 ms. The maximum temperature at the laser-spot area was 305°C. Temperature history of the laser spot for the irradiation time of 0.25 s is shown in Fig. 5.18. The temperature was measured on the surface of the material. The temperature increased rapidly for a few milliseconds after the irradiation started, converged at about 305°C and was maintained until the end of irradiation. The temperature dropped quickly to the ambient temperature after the irradiation ended. This corresponds to the temperature results shown in Fig. 5-5.

Table 5-5 Summary of the analysis conditions

Analysis conditions		Units
Type of element	Solid 90 / Solid87	
Workpiece size, $(a \times b \times d)$	20×10×0.5	mm <sup>3</sup>
Laser beam diameter (oval) $(D_1 \times D_2)$	0.25 x 0.19	mm
Heat transfer coefficient, $h$	8	Wm <sup>-2</sup> K <sup>-1</sup>
Initial temperature, $T_0$	20	C
Irradiation time, $t$	0.25	s
Laser power, $P$	70	W

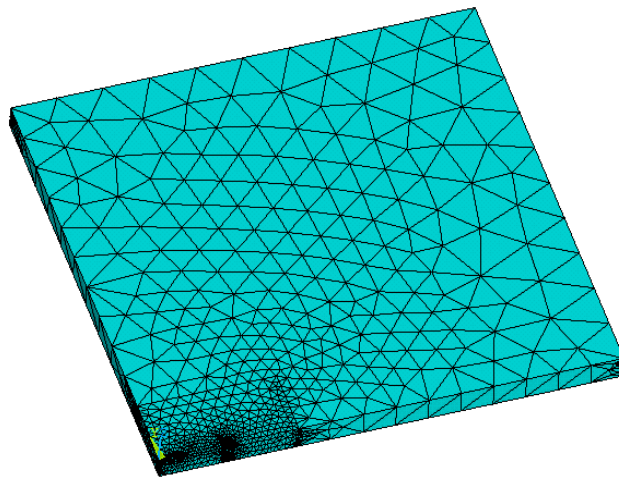


Fig. 5.16 Finite-element model with meshing element of 21,900 nodes

Fig. 5.19 shows the temperature distribution on the  $x$ - $z$  plane from position  $x=0$  mm to  $x=1.5$  mm at the irradiation times 1 ms, 10 ms, and 50 ms. The temperature gradient was generated along the  $x$ -axis direction. A higher temperature region was generated at the area close to the laser spot with the maximum temperature resulting on the top surface of the specimen. The temperature distribution along the vertical direction ( $z$ -axis) was almost constant except for the area of the laser spot. This phenomenon occurred because of the high thermal conductivity of the silicon wafer. The heat was disseminated from the laser spot in a short time. Furthermore, the silicon wafer is very thin; the temperature distribution in the vertical direction was therefore almost constant.

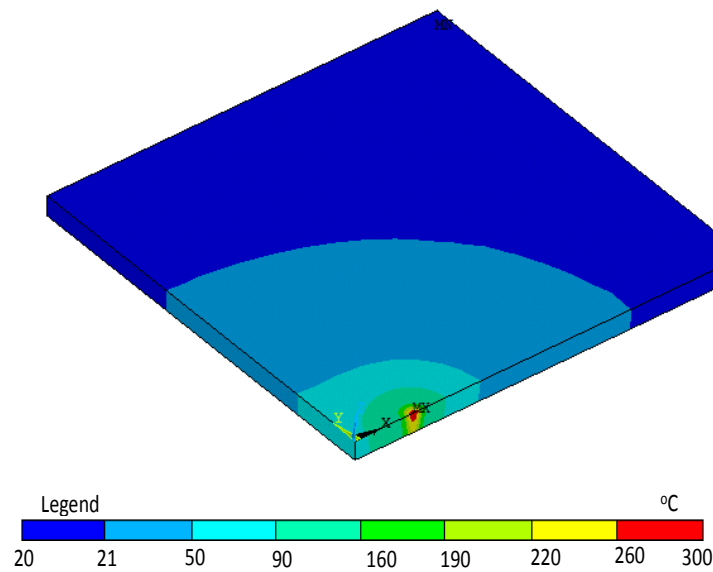


Fig. 5-17 Temperature distribution at  $P=70$  W and irradiation time of 50 ms



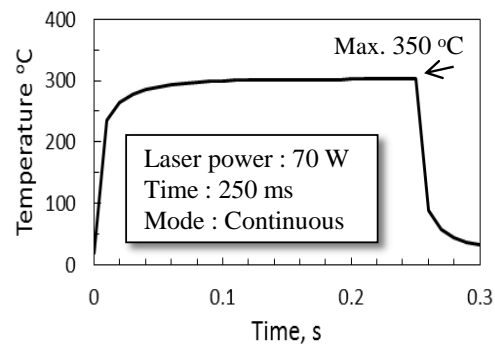


Fig. 5-18 Temperature history at the laser spot

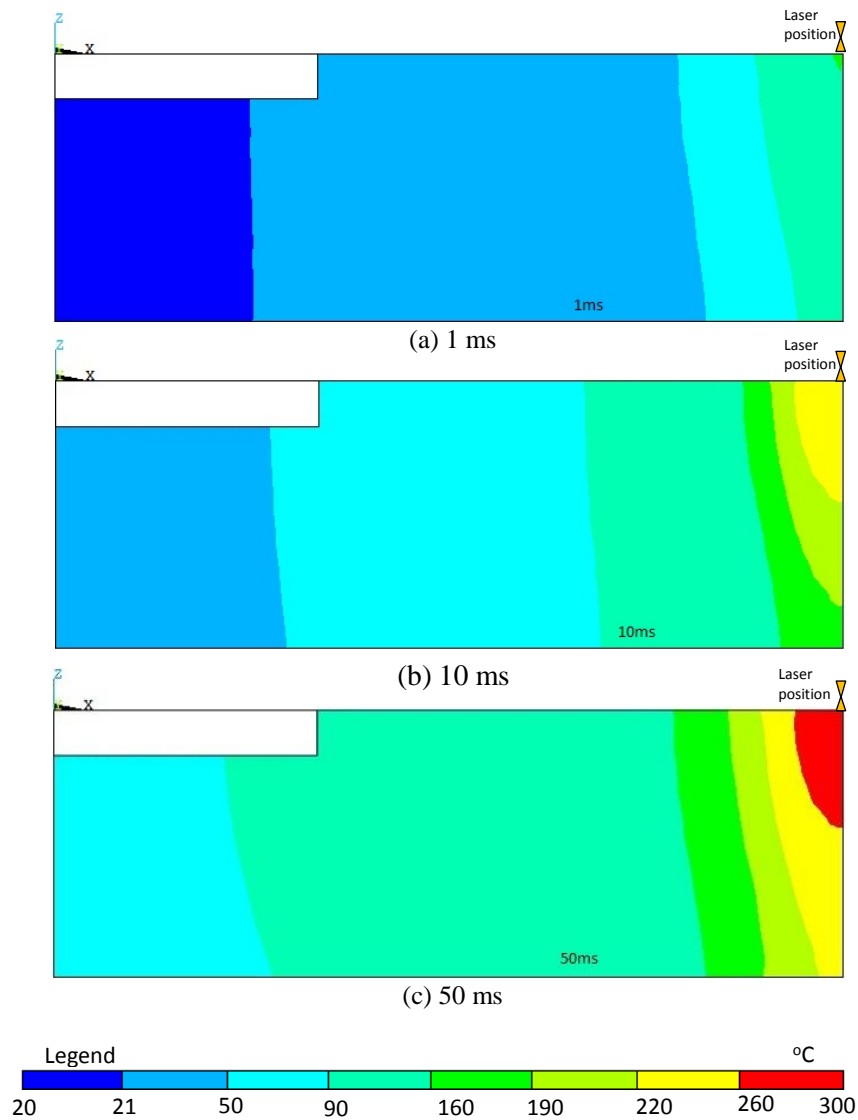


Fig. 5-19 Temperature distribution at different irradiation times along the  $x$ - $y$  plane ( $x=0$  to  $x=1.5$  mm)

**(b) Thermal-stress analysis result**

The thermal-stress ( $\sigma_{yy}$ ) distribution on the specimen is illustrated in Fig. 5-20. The stress was measured in the y-y direction. Compressive stress resulted at the point of laser-beam irradiation, while tensile stress was found around the compressive-stress region and showed higher magnitude in the area of the micro-groove. The details of the thermal-stress ( $\sigma_{yy}$ ) distribution on the x-z plane from  $x=0$  mm to  $x=1.5$  mm at the irradiation times of 1 ms, 10 ms and 50 ms are shown in Fig. 5-21. The results show that compressive thermal stress was centered in the laser-beam spot area. Tensile stress, meanwhile, was produced in the area close to the micro-groove, with two positions having high thermal-stress intensities. These positions were the groove end and the groove edge tip (as shown in Fig. 5-21(a)).

The relationships between thermal stress ( $\sigma_{yy}$ ) and irradiation time at both positions are illustrated in Fig. 5-22(a); Fig. 5-22(b) shows an enlarged view focusing the transition of the maximum-thermal-stress position between groove end and groove edge tip. The tensile stress ( $\sigma_{yy}$ ) was found to be advanced at the beginning of laser irradiation at the groove end. However, as the irradiation time was increased, the maximum-tensile-stress position changed to the groove edge tip. This change occurred at about 1.5 ms. Before 1.5 ms, the tensile stress is too small for fracture occurrence. Fracture starts at the groove edge tip once the tensile stress attains the fracture strength of the material.

The change of thermal-stress ( $\sigma_{yy}$ ) distribution during laser irradiation is illustrated in Fig. 5-23. At the beginning of the irradiation time, the thermal-stress region develops into a small area so that the tensile region reaches the groove end. However, after a few milliseconds, the tensile-stress region is developed further, and tensile stress is advanced at the groove edge tip. The maximum tensile stress is concentrated at this position and the fracture may start from this point.

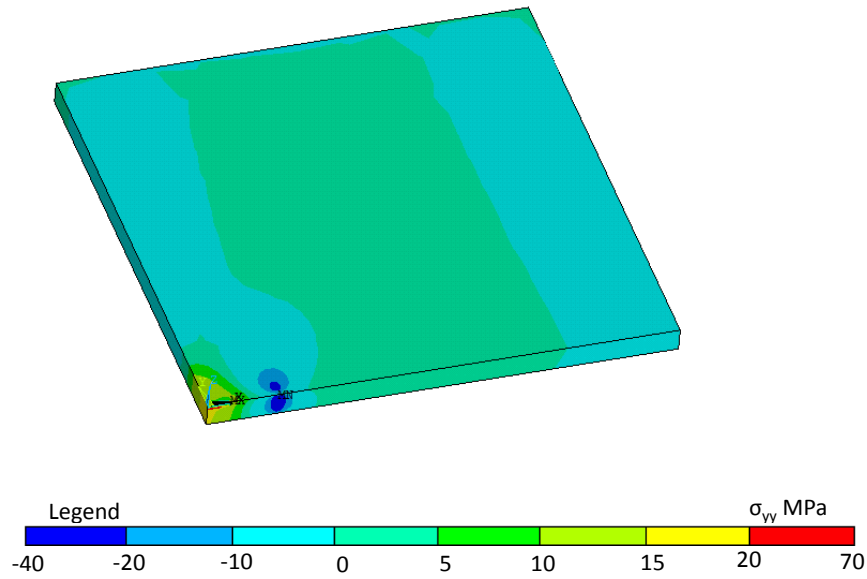


Fig. 5-20 Thermal-stress region at  $P=70$  W and irradiation time of 50 ms

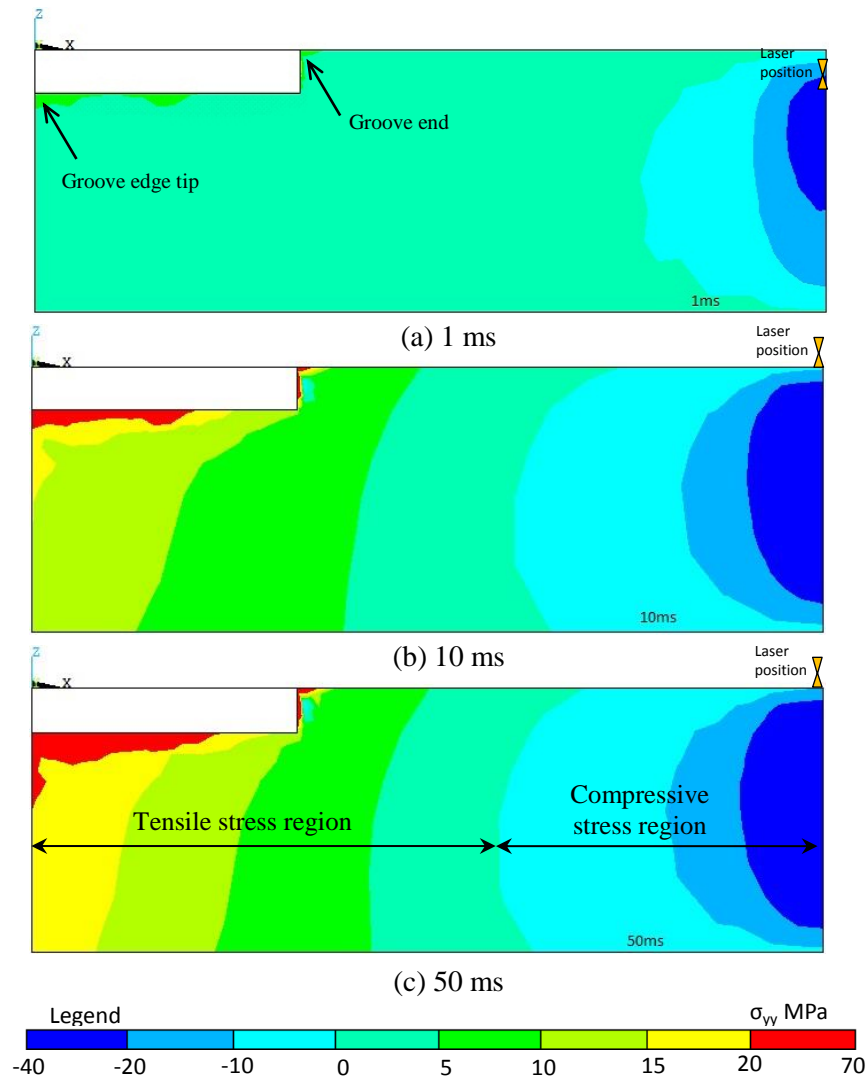


Fig. 5-21 Thermal-stress ( $\sigma_{yy}$ ) distribution at different irradiation times along the  $x$ - $y$  plane ( $x=0$  to  $x=1.5$  mm)

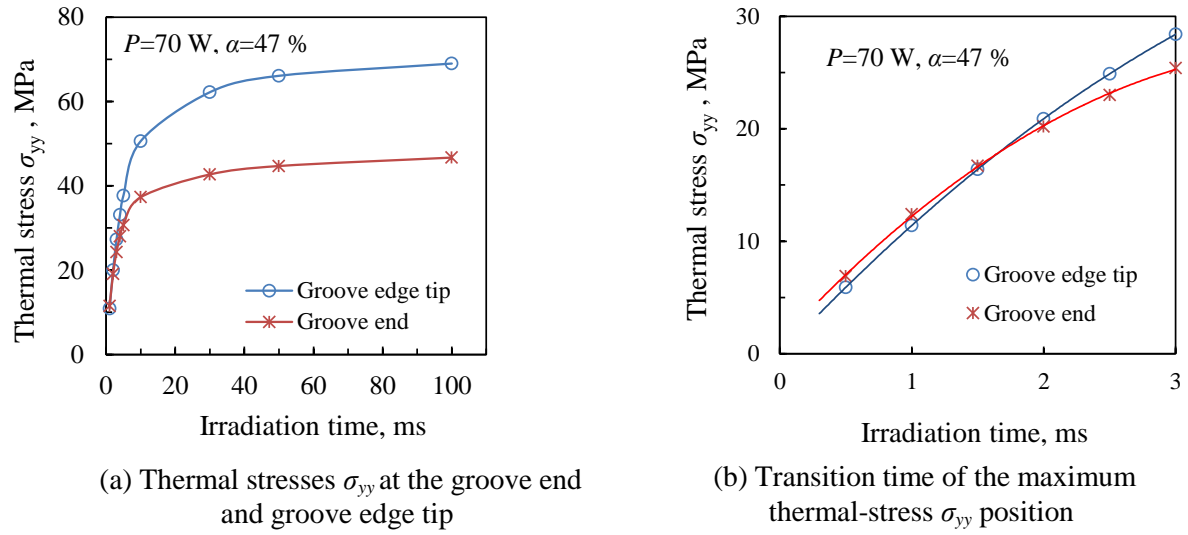


Fig. 5-22 Relationships between thermal stresses ( $\sigma_{yy}$ ) and irradiation time

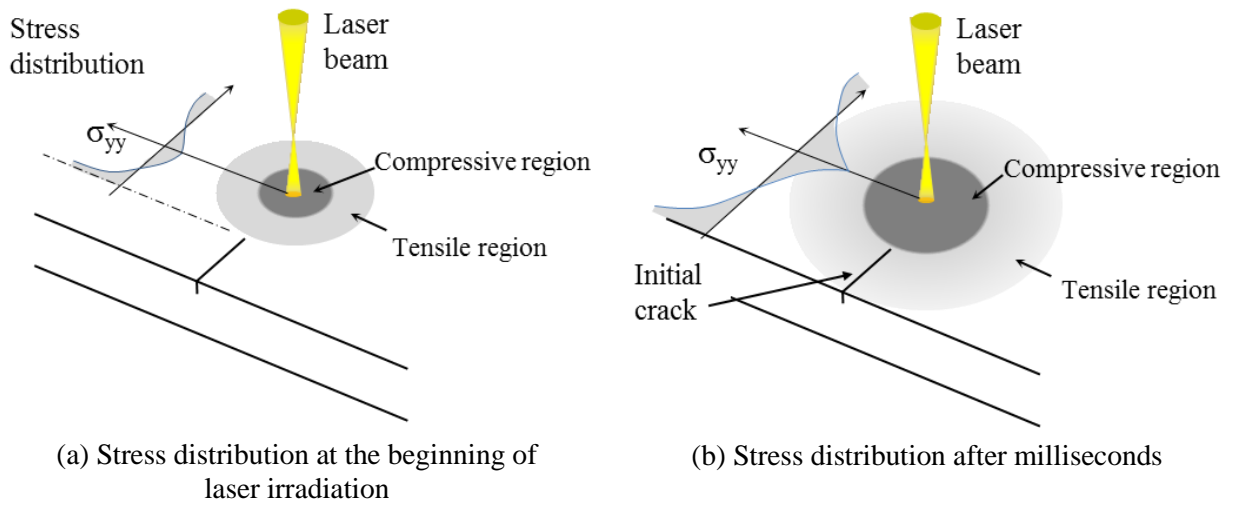


Fig. 5-23 Change of thermal stress ( $\sigma_{yy}$ ) distribution on the wafer with initial crack (micro-groove)

## 5.5 CONCLUSIONS

An investigation into the separation of a silicon-wafer specimen by applying a single-point laser has been carried out experimentally and computationally. A wafer was evaluated in terms of separation performance with different types of initial cracks by observing the temperature and time for fracture occurrences. The laser irradiation temperature was measured by a two-color pyrometer with an optical fiber, and fracture occurrence was observed by an acoustic emission sensor.

Based on the experimental results, it can be concluded that separating performance of the silicon wafer can be distinguished between different methods of initial crack. Both methods were able to initiate the fracture for cleaving execution. Fracture occurred when the temperature of the laser irradiation spot was higher than the critical temperature. Higher tensile stress became concentrated on the sharper crack tip, thus increasing the tendency for fracture initiation.

From the finite-element method analysis, the results showed how the specimen responded to the heat supplied by the laser beam. Thermal stress was generated by a laser beam that caused tensile stress accumulated in the area of the micro-groove. From the thermal-stress distribution results, the position of the fracture initiation was identified.

## REFERENCES

- [1] T. Ishikawa, T. Ueda, T. Furumoto, Hosokawa, A., Tanaka, R. “Pre-Groove Development for Laser Cleaving of Brittle Materials by Using Micro-Lens,” *Journal of Advanced Mechanical Design, Systems, and Manufacturing*, 6(6), pp. 841-848, 2012.
- [2] T. Ueda, K. Yamada, K. Nakayama, , “Temperature of work materials irradiated with CO2 laser,” *CIRP Annals - Manufacturing Technology*, 46(1), pp. 117-122T, 1997.
- [3] C. Fischer, C. Anthony, *Introduction to Contact Mechanics*, second edition, Springer Science, New York, pp. 31-48, 2007.
- [4] K. A. Elijah, *Principles of Laser Materials Processing*, John Wiley & Sons Inc., New Jersey, pp. 14-17, 2009.
- [5] S. Nisar, L. Li, M. Sheikh, and A. Pinkerton, “The effect of continuous and pulsed beam modes on cut path deviation in diode laser cutting of glass,” *Int. J. Adv. Manuf. Technol.*, vol. 49, no. 1, pp. 167-175, 2009.
- [6] J. Liu, J. Lu, Xi. Ni, G. Dai, L. Zhang, and Y. Chen, “Numerical study on thermal stress cutting of silicon wafer using two-point pulsed laser,” *Opt. Appl.*, vol. 41, no. 1, pp. 247-255, 2011.

## **CHAPTER 6: INVESTIGATION OF THERMAL-STRESS CLEAVING WITH MOVING LASER**

### **6.1 INTRODUCTION**

In this chapter, the separating characteristics of a silicon wafer with a moving laser beam using the thermal-stress cleaving process are investigated experimentally and computationally. The investigation of thermal-stress cleaving with a single-point laser has been reported in the previous chapter. In typical laser-cleaving practice, the laser is moved along the cutting path, either in continuous- or pulse-wave mode. In this study, a continuous-wave Nd:YAG laser was used to irradiate the silicon-wafer specimen.

The silicon-wafer specimen is initially prepared with micro-groove at the leading edge to facilitate the material separation. The temperature of the moving laser spot is measured by using a two-color pyrometer with an optical fiber, and the AE signal is assessed to observe the mechanism of crack propagation. The effect of laser energy on the cleaving mechanism is analyzed, and the influence of the parameters of groove length and depth is also studied. The cleaved surface is observed using a scanning electron microscope (SEM). Further, the relationships between laser power, temperature, fracture initiation, crack propagation, cleaved surface features and groove parameters are investigated.

In order to explain the three-dimensional thermal-stress distribution, the finite-element method (FEM) software, ANSYS, is applied considering the temperature ascertained from the experimental result. Stress condition at the laser irradiation area is estimated quantitatively by determining the stress intensity factor. To estimate the material failures or fracture initiation, fracture toughness of the wafer is determined by using the Vickers indentation technique. Additionally, the influence of the micro-groove parameters is evaluated by using the stress intensity results, and is compared to the experimental results. Finally, the silicon-wafer separating mechanism by laser cleaving is evaluated.

## **6.2 EXPERIMENTAL METHODOLOGY**

### **6.2.1 Silicon-wafer specimen**

The specimen used in the experiments was a silicon wafer of crystal (100) orientation and thickness 0.5 mm. A schematic illustration of the silicon wafer specimen of size 20 mm x 10 mm x 0.5 mm is shown in Fig. 6-1. The specimen was prepared by scribing and snapping procedures. The specifications of the silicon wafer used in this experiment are summarized in Table 6-1.

The micro-groove was created initially by focusing the pulsed laser beam through the micro-lens at the edge of the silicon wafer [1]. A second-harmonic-generation (SHG) Nd:YAG laser with a wavelength of 532 nm, frequency of 10 Hz and 5 nsec pulse width was used in the specimen preparation. The laser beam was focused on the specimen to cause material heating and evaporating, hence forming the groove. By using this technique, the groove size can be controlled, and the area of damage can be minimized.



The depth of the groove is adjusted by varying the number of laser pulses, while the groove length is controlled by focusing the laser beam only on the required exposed area. Fig. 6-2 shows the relationship between the groove depth and number of laser pulses. In this study, the groove dimensions were fixed to  $80\text{ }\mu\text{m}$  in depth and  $500\text{ }\mu\text{m}$  in length. Therefore, the laser pulse number used was approximately 450. The pre-prepared micro-groove is illustrated in Fig. 6-3. The groove with a blunt tip was produced with dimensions of  $80\text{ }\mu\text{m}$  in depth and  $500\text{ }\mu\text{m}$  and length.

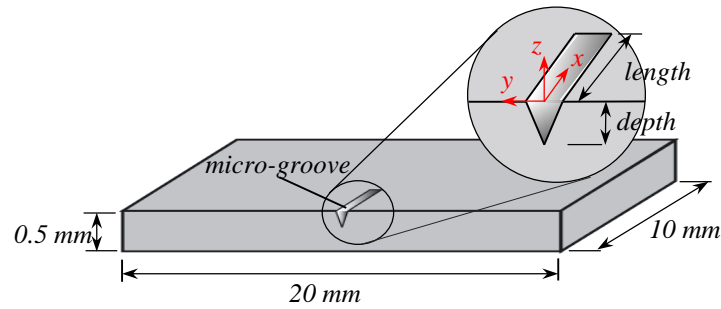


Fig. 6-1 Schematic illustration of silicon-wafer specimen with the micro-groove and  $x$ ,  $y$  and  $z$  reference axes

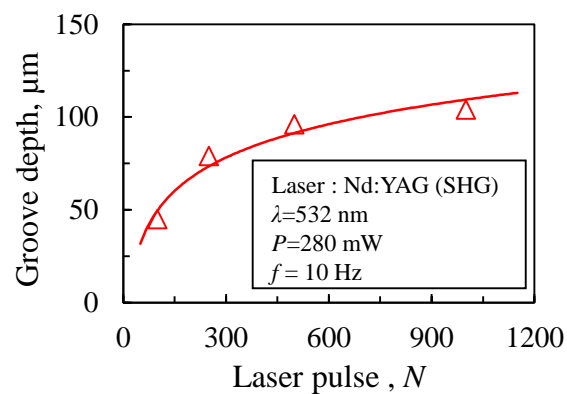


Fig. 6-2 Relationship between laser pulse number and groove depth

Table 6-1 Specifications of silicon wafer

Silicon wafer	P-type polished wafer	Units
Crystal plane	(100)	
Manufacturing method	Czochralski process	
Manufacturer	SUMCO	
Diameter, $D$	125	mm
Thickness, $t$	0.5	mm
Thermal conductivity, $K$	156	W/m·K
Specific heat, $C$	761	J/kg·K
Density, $\rho$	2340	kg/m <sup>3</sup>
Thermal expansion coef., $\alpha$	$2.62 \times 10^{-6}$	K <sup>-1</sup>
Young modulus, $E$	169	GPa
Poisson ratio, $\nu$	0.262	

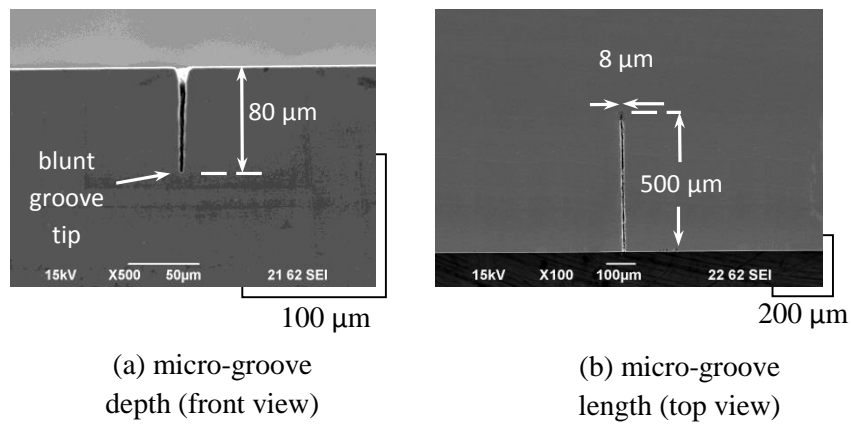


Fig. 6-3 SEM images of micro-groove with dimensions

### 6.2.2 Experimental procedure

This experiment investigated the temperature of the moving laser spot and the acoustic-emission (AE) signals. The temperature of the laser spot was measured by using a two-color pyrometer with optical fiber, developed by Ueda et al. [2]. The AE signals were measured by using the AE sensor to observe the formation of crack propagation during the laser irradiation process.

As illustrated in Fig. 6-4, the specimen was set on a moving table (X-Y stage). The moving table moved at a constant speed of 2 mm/s, and the laser beam relatively scanned the work material at the same speed. The laser beam and optical fiber remained in a static position while the AE sensor moved together with the work material.

The experimental arrangement is illustrated in Fig. 6-5. A continuous-wave Nd:YAG laser with a wavelength of 1.06  $\mu\text{m}$  was used as a heat source. The elliptical beam spot with a major axis length of 0.25 mm and minor axis length of 0.19 mm was defocused on the wafer's surface. The laser beam moved parallel to the major axis. A chalcogenide optical fiber was set at a distance of 3 mm from the laser spot and at an angle of  $45^\circ$  to the optical axis. The center of the laser spot was always on the center axis of the fiber. The infrared energy radiated from the object was captured by a chalcogenide optical fiber and transmitted to a two-color pyrometer consisting of InSb and MCT detectors. The infrared energy was converted to an amplified electric signal. By calculating the ratio of the output voltages from these two detectors, the temperature of an object can be obtained by using the calibration curve.

The AE signal was measured to monitor the characteristics of fracture initiation and crack propagation during the laser irradiation process along the cleaving path. An AE sensor

was fixed on the wafer's surface at a distance of 5 mm from the micro-groove, as shown in Fig. 6-5. Details of the AE signal measurements are summarized in Table 6-2.

Before the X-Y stage started moving, the laser beam was set at a position of 2 mm from the silicon wafer's leading edge. After the X-Y stage had been moving for one second, the center of the laser beam reached the wafer's leading edge. The voltage output of the pyrometer detectors and the AE signals in relation to the irradiation time can therefore be determined. Consequently, the temperature distribution and crack occurrence during laser irradiation along the laser beam's path on the work material can be verified.

The output voltages from the pyrometer detectors and AE sensor were recorded in a digital oscilloscope. The laser powers used for this experiment were varied between 50 W and 70 W, while the groove length and depth were maintained at 500  $\mu\text{m}$  and 80  $\mu\text{m}$ , respectively. The scan speed was set at 2 mm/s. After the specimen had been separated, the separating surface of the specimen was analyzed by using a scanning electron microscope (SEM). A summary of the experimental conditions is shown in Table 6-3.

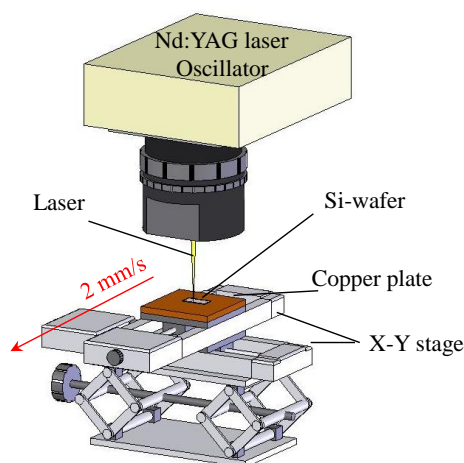


Fig. 6-4 Illustration of the specimen on a moving table (X-Y stage).

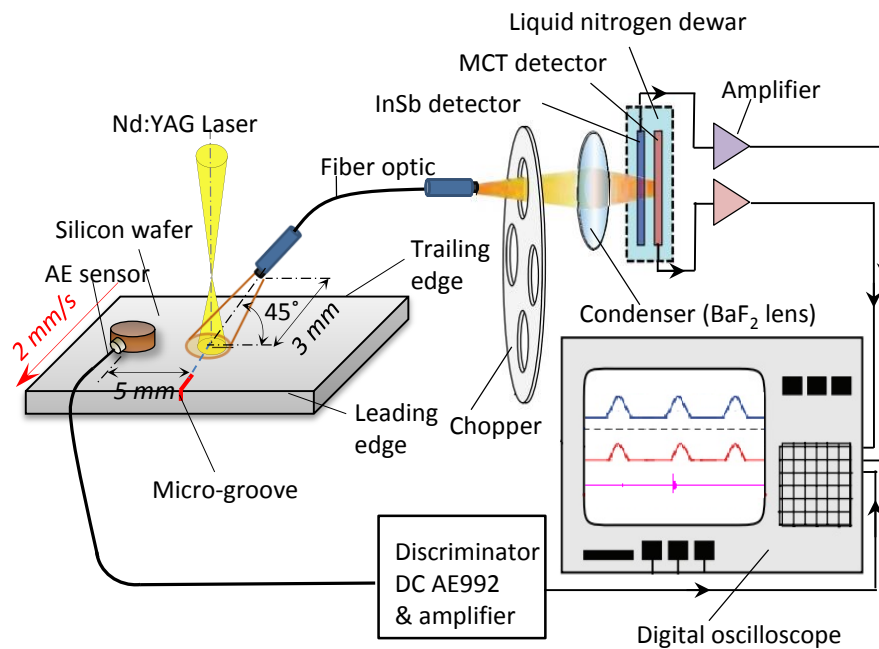


Fig. 6-5 Schematic illustration of experimental set-up with fundamental structure of two-color pyrometer and AE sensor

Table 6-2 Measuring system of AE signal

Acoustis Emission (AE) sensor		Units
Size	Ø5 x 3.2	mm
Frequency band (-10dB)	1 ~ 4	MHz
PreAmplifier		
Gain	40	dB
Frequency band (-10dB)	0.1 ~ 20	MHz

Table 6-3 Experimental condition

Laser	Nd:YAG	Units
Wavelength, $\lambda$	1064	
Irradiation mode	Continuous wave	
Laser power, $P$	50 ~ 70	W
Laser beam diameter, $D$	0.25x0.19	mm <sup>2</sup>
Moving speed, $v$	2	mm/s
Work piece	Silicon wafer	
Crystal orientation	<100>	
Size	10x20x0.5	mm <sup>3</sup>
Pyrometer	Two-color	
Optical fiber	NSEG Ø380 $\mu$ m	
Detector	InSb/ MCT	
Fiber core diameter, $\phi$	380	$\mu$ m

## 6.3 EXPERIMENTAL RESULTS AND DISCUSSION

### 6.3.1 Temperature measurement

Fig. 6-6 illustrates the moving-laser-beam irradiation during the experiment. The laser beam was moved along the  $x$ -axis ( $y=0$ ) with a scan speed of 2 mm/s. The time when the center of the laser beam reached the leading edge of the specimen ( $x=0$ ,  $y=0$ ,  $z=0$ ) was considered as  $t=0$  s.

Typical output profiles of the pyrometer and AE sensor are shown in Fig. 6-7. Fig. 6-7(a) and Fig. 6-7(b) represent the output voltages of the two detectors, InSb and MCT. The

signal from the pyrometer detectors shown was a result of chopped signals that were produced by using a chopper in the pyrometer set-up.

The InSb and MCT voltage signals were increased rapidly after the laser beam reached the wafer's leading edge, and later decreased proportionally until they attained a stable voltage output at the center area of the wafer. The laser beam was emitted on the wafer surface with Gaussian's intensity distribution [3]. Hence, the pyrometer detectors' signal was detected earlier, before the laser beam's center reached the wafer's leading edge. The output voltage signal increased smoothly when the laser beam was approaching the wafer's trailing edge, and declined quickly before the laser beam passed the wafer's trailing edge.

Fig. 6-7(c) shows the temperature history of the laser spot moving along the irradiation path. The temperature was obtained by calculating the ratio of the InSb over MCT output voltage signals. Higher temperature of the laser spot was recorded near to the edge of the silicon wafer. The maximum temperature of 385°C was recorded at approximately  $t=0.27$  s. The temperature at the center of the specimen was approximately 205°C, while the temperature of laser spot rose to 340°C at approximately  $t=4.73$  s. The laser beam reached the wafer's trailing edge at  $t=5$  s.

The results indicate that the laser spot was maintained at a constant lower temperature at the center of the laser path. Silicon wafer has a high thermal conductivity of 156 W/m.K [4,5]. Hence, the energy produced by laser irradiation was circumferentially diffused when the laser beam was at the center of the wafer.

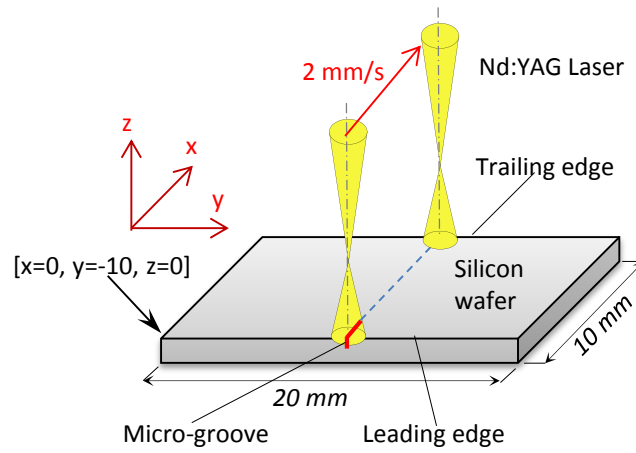


Fig. 6-6 Moving laser beam irradiation during the experiment

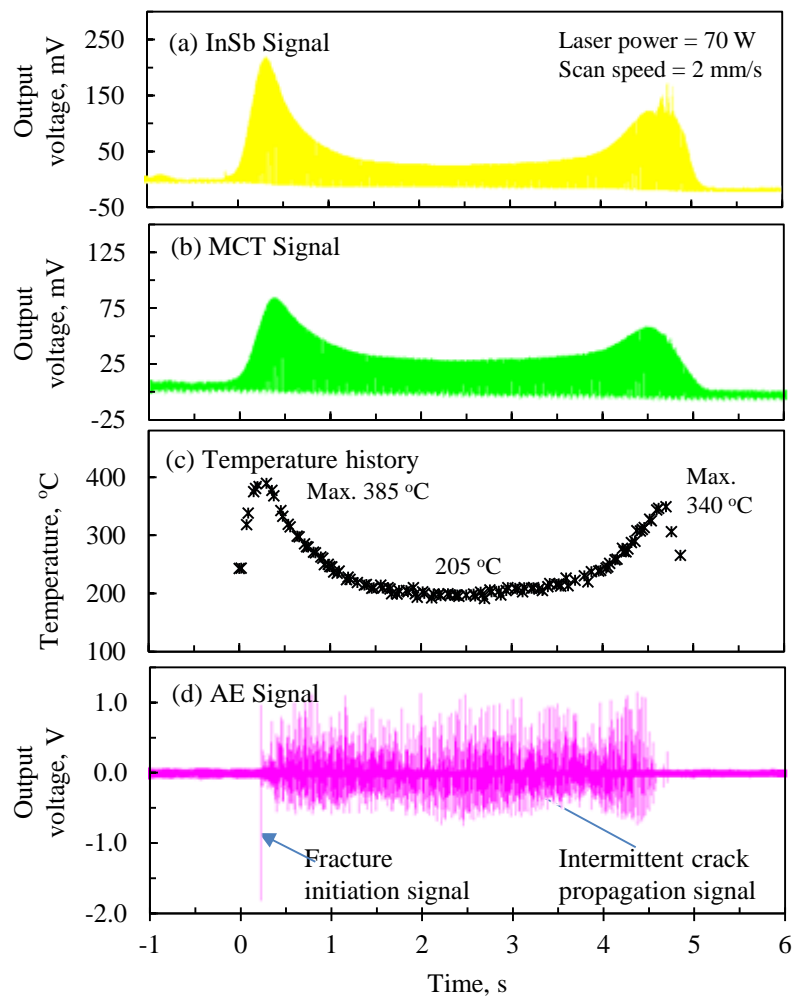


Fig. 6-7 Output wave of pyrometer and AE sensor



The variation of maximum temperatures at the leading edge and the trailing edge, and the average temperature at the center of the specimen with laser power are shown in Fig. 6-8. The temperature at all three positions increased with increasing laser power. From the results, it can clearly be seen that the temperature of the moving laser spot is dependent on the energy supplied by the laser beam. A higher laser power resulted in a higher temperature.

### 6.3.2 Acoustic-emission (AE) signal measurement

The signal from the AE sensor during laser-beam irradiation is displayed in Fig. 6.7(d). The AE signals show the characteristics of the thermal cleaving process during laser irradiation. As the fracture occurred, the AE sensor triggered the signals. A large signal was observed a few milliseconds after the laser beam reached the wafer's leading edge, continuing with the repeating signals.

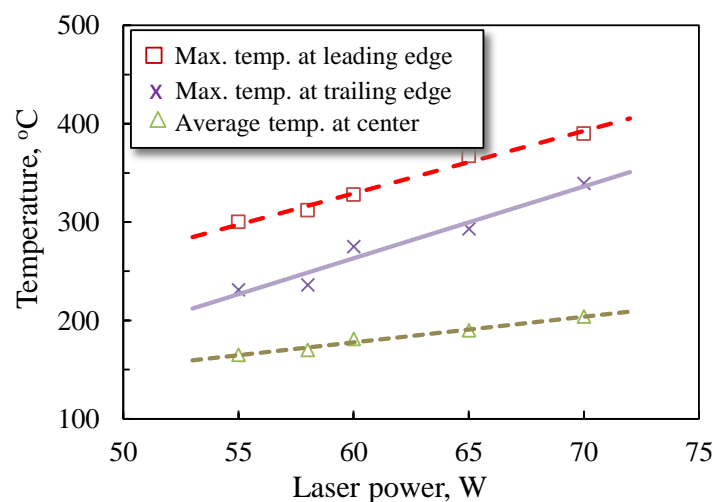


Fig. 6-8 Influence of laser power on temperature

Voltage output signals from the AE sensor demonstrated that the crack occurrences appeared in two stages, namely fracture initiation and intermittent crack propagation. AE signals were produced when a rapid release of energy from localized sources within the material occurred. Energy release happened as a result of crack extension due to the thermal stress generated by the laser beam. The first signal of the AE wave showed that the fracture initiation occurred with large signal size. Subsequently, a series of smaller AE signals indicate that crack propagation occurred intermittently.

A large signal indicates that greater energy was released during fracture initiation. It can be seen that the energy required to start the fracture was high in comparison with the energy required during the crack propagation. This was because the fracture initiation started at the groove tip with a blunt notch (Fig. 6-3(a)), and a sharp crack tip was produced after the first fracture occurred. Greater stress concentration developed at the sharper crack tip in comparison to the blunt groove. Therefore, more energy was required to increase the local stress at the blunt groove before reaching the fracture strength of the material.

#### **a. Fracture initiation**

The laser beam's energy generates a thermal gradient, which creates a compressive thermal stress in the area of the laser beam and the tensile-stress area around it. Once the laser beam reaches the leading edge, compressive stress is generated at this point due to the heat induced from the laser beam. When the laser beam moves forward, thermal stress at the leading edge of the silicon wafer changes into tensile stress and is concentrated at the groove tip ( $x=0$ ,  $y=0$ ,  $z=-80\text{ }\mu\text{m}$ ). After the tensile stress achieves the fracture strength of the material, the fracture will be initiated.

Fig. 6-9 shows the enlarged AE signal from Fig. 6-6(d), focused on the fracture initiation signal. The time taken for fracture initiation to occur was measured, and the relationships between different laser powers and fracture initiation times were recorded. Fig. 6-10 shows the influence of laser power on the fracture initiation time. The results indicate that the fracture initiation time decreased with an increase in laser power. The average fracture initiation times with the laser powers of 50 W and 70 W were approximately 0.42 s and 0.27 s, respectively. Greater stress force was generated at higher laser power, resulting in earlier fracture initiation.

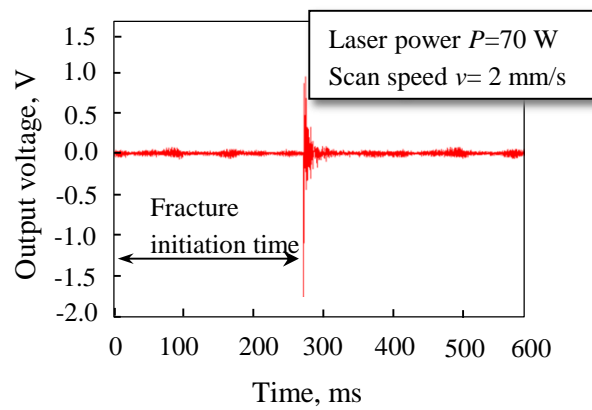


Fig. 6-9 Fracture initiation signal

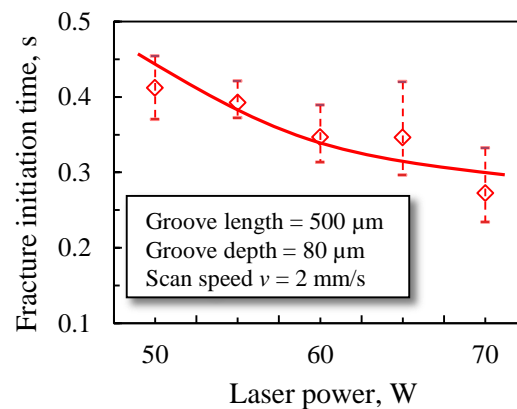


Fig. 6-10 Influence of laser power on crack initiation time

**b. Intermittent crack propagation**

Fig. 6-11 shows the typical output signals from an AE sensor measured in the middle of the laser path. The variation of laser power with the AE signal interval is shown in Fig. 6-12. It can be seen that a repetitive AE signal appeared with a starting and stopping phenomenon at regular intervals. This phenomenon reveals that the crack was extended and relaxed frequently at a distance as the laser beam moved along the laser path. The increase of laser power produced shorter intervals between the crack propagation signals. The intervals were found to be constant and comparable to the changes in laser power. For instance, the interval in signals found with a laser power of  $P=50$  W was about 16.2 ms, or 32.4  $\mu\text{m}$  in distance, while the signal interval for  $P=70$  W was about 10.5 ms, or 21  $\mu\text{m}$  in distance. The crack in the material grew with the relaxation of local stress, and developed again when sufficient stress was attained. The stress recovery rate was increased with the increase of laser power. Therefore, crack signals appeared rapidly.

**6.3.3 Cleaving surface observation**

After the irradiation of the laser beam, the specimen then separated into two pieces. The separating surface of the specimen was analyzed by using a scanning electron microscope (SEM). Observation of the cleaving were made at two positions, namely the starting and center sections, as shown in Fig. 6-13.

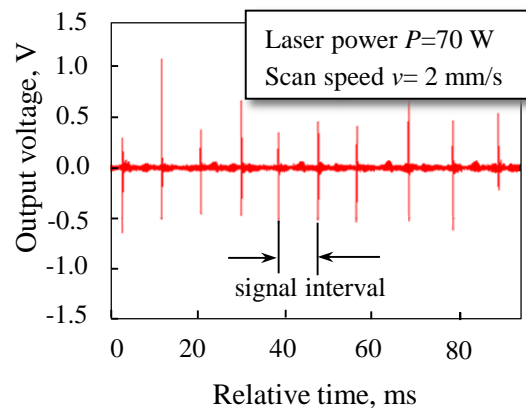


Fig. 6-11 AE signals in the middle of laser path

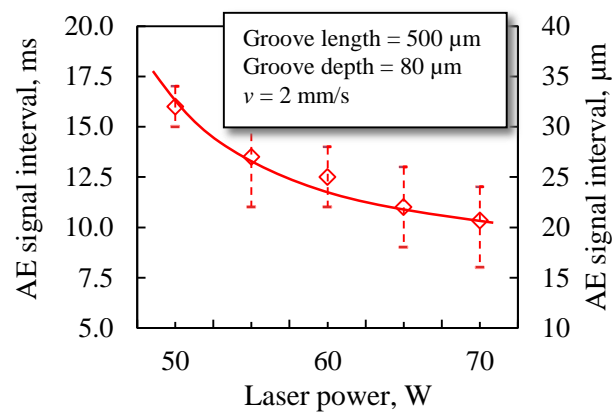


Fig. 6-12 Relationship between laser power and AE signal interval

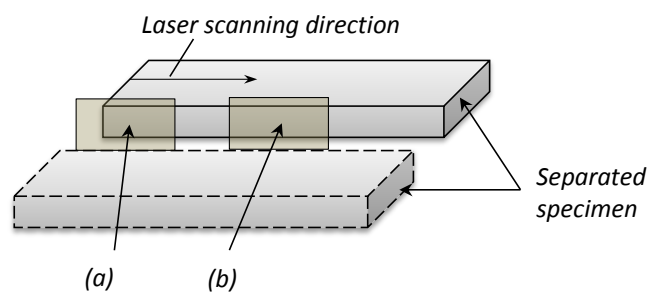


Fig. 6-13 Observation position on cleaving surface:  
a) starting section; b) center section

### a. Cleaving surface at starting section

Fig. 6-14 shows the SEM images of the separated plane as observed at the starting area of the silicon wafer. A smooth and flat surface was produced at a width of a few micrometers from the wafer's edge, followed by a periodic wave marking. This surface was produced due to the initial fracture occurrence at the beginning of the laser irradiation. The extent of the smooth surface decreased in length with the increase of laser power. The distance of the smooth surface was obtained as approximately 420  $\mu\text{m}$  at a laser power of 70 W; it was 390  $\mu\text{m}$ , 295  $\mu\text{m}$ , 238  $\mu\text{m}$  and 185  $\mu\text{m}$  for laser power of 65 W, 60 W, 55 W and 50 W, respectively. The variation of the extent of the smooth surface with the laser power is summarized in Fig. 6-15.

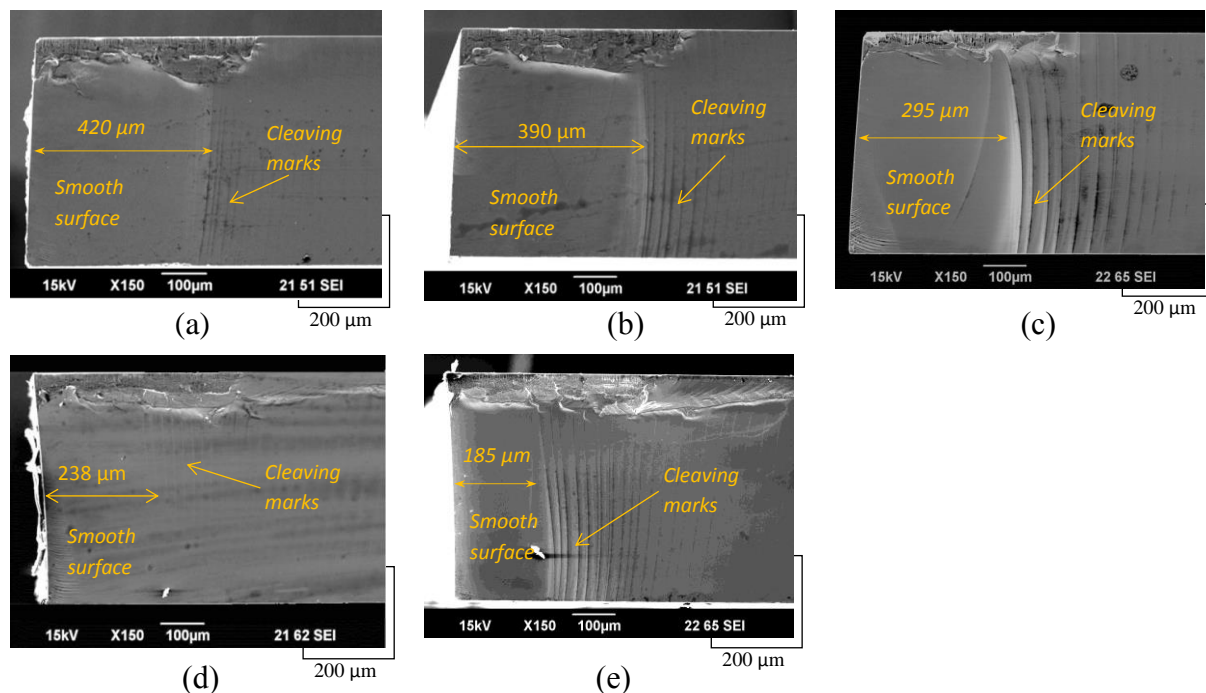


Fig. 6-14 SEM images at the starting section of cleaving surface: (a)  $P=50$  W; (b)  $P=55$  W; (c)  $P=60$  W; (d)  $P=65$  W; (e)  $P=70$  W

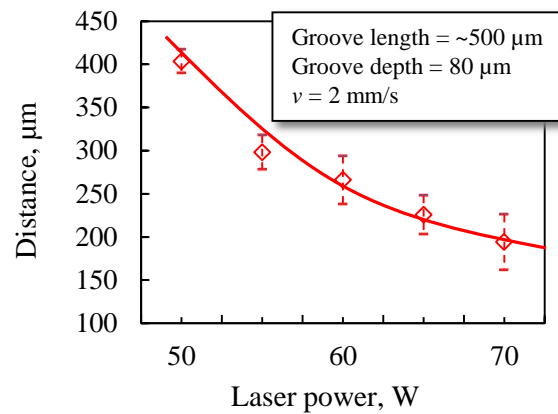


Fig. 6-15 Relationship between laser power and extent of smooth surface

**b. Cleaving surface at center section**

Fig. 6-16 shows the SEM images of the cleaving pattern marked on the center section of the cleaving surface. It is shown that constant intervals were developed between the cleaving marks. The distance between the marks decreased with the increase of laser power. The variation of the mark interval with the laser power is given in Fig. 6-17. The wave marks were developed due to occurrences of crack advancement during the intermittent crack propagation phenomena. The interval between the marks was approximately 32 μm with the laser power of 50 W, and 27 μm and 22 μm for 60 W and 70 W, respectively. The obtained intervals were comparable to the AE signals reported in Fig. 6-12. The increase of laser power caused higher repetition of the cleaving mark.

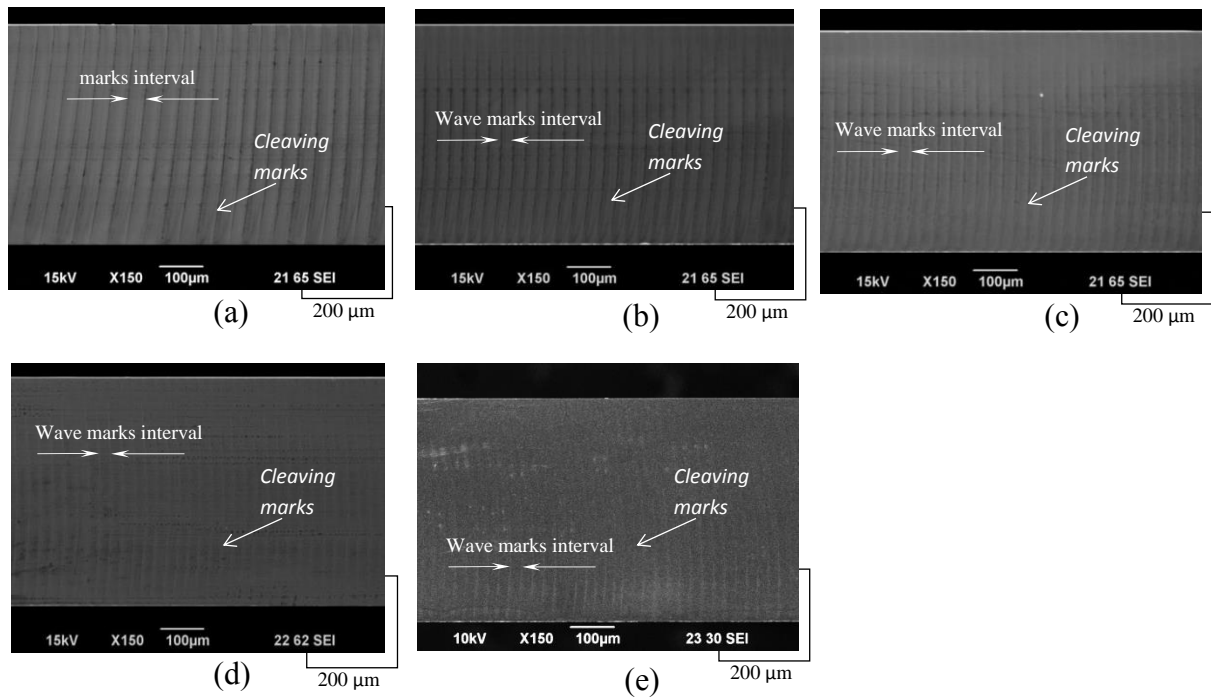


Fig. 6-16 SEM images at the center section of cleaving surface: (a)  $P=50$  W; (b)  $P=55$  W; (c)  $P=60$  W; (d)  $P=65$  W; (e)  $P=70$  W

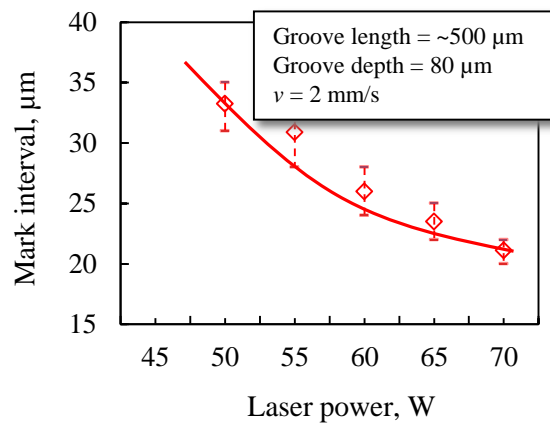


Fig. 6-17 Relationship between cleaving mark interval and laser power



#### 6.3.4 Influence of groove length and depth

To understand the influence of groove parameters such as groove length and groove depth on cleaving performance, experiments were performed irradiating with a constant laser power of 70 W and scan speed of 2 mm/s. In the case of varied groove lengths the depth was fixed at 80  $\mu\text{m}$ , and in the case of varied groove depths the length was fixed at 500 $\mu\text{m}$ . The AE signal was used to monitor the fracture initiation, followed by the procedure described in the previous section. Table 6.4 summarizes the experimental conditions for varied groove length and depth, accordingly.

Fig. 6-18 shows the effect of groove length on fracture initiation time. The result shows that the time for fracture initiation was decreased with enlarged groove length. For instance, the average fracture initiation time obtained with a groove length of 100  $\mu\text{m}$  was about 450 ms, and 270 ms with a groove length of 500  $\mu\text{m}$ .

The variation of groove depth with fracture initiation time is reported in Fig. 6-19. It was found that the fracture initiation time became shorter as the groove depth increased. The average fracture initiation time at a groove depth of 50  $\mu\text{m}$  reached approximately 340 ms, compared to 270 ms at a groove depth of 130  $\mu\text{m}$ . From the finite-element analysis results, it can be seen that higher tensile stress concentration resulted in longer groove length (Fig. 6-23) and deeper groove depth (Fig. 6-25). Fracture initiation time was reached earlier at a longer groove length and a deeper groove depth: it is apparent that the groove becomes the weakness point in the material. Local stress at the groove tip could rise to several times that of the applied stress, and the stress level increased with the increase of groove size.

Table 6-4 Experiment conditions of varied groove length and groove depth

Laser	Nd:YAG	Units
Wavelength, $\lambda$	1064	
Irradiation mode	Continuous wave	
Laser power, $P$	70	W
Laser beam diameter, $D$	0.25x0.19	mm <sup>2</sup>
Moving speed, $v$	2	mm/s
Experiment of varies groove length		
Groove length	100 ~ 500	$\mu\text{m}$
Groove depth	80	$\mu\text{m}$
Experiment of varies groove depth		
Groove length	500	$\mu\text{m}$
Groove depth	20 ~ 150	$\mu\text{m}$

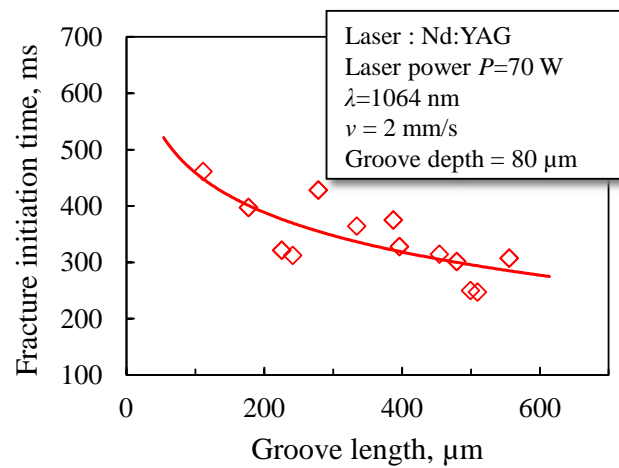


Fig. 6-18 Effect of groove length on fracture initiation time

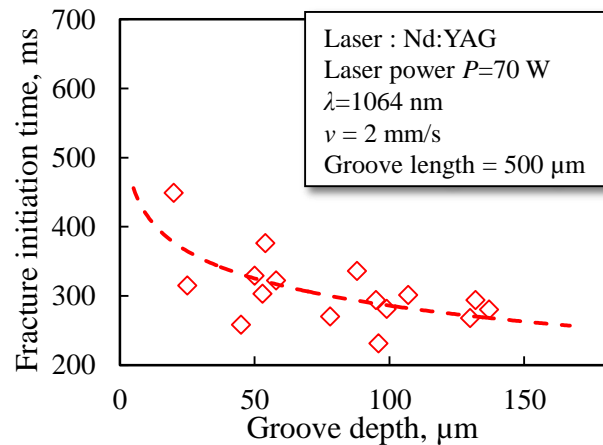


Fig. 6-19 Effect of groove depth on fracture initiation time

## 6.4 FINITE-ELEMENT ANALYSIS

The computational analysis was performed to understand the actual phenomenon of fracture during the thermal cleaving process. The temperature and AE signal of crack behavior have been already monitored during the experimental work. However, the mechanisms of fracture have not yet been clarified. This section presents analysis of thermal stress during fracture initiation.

Finite-element software (ANSYS) was used to analyze the behavior of thermal-stress cleaving during laser irradiation by considering the finite-boundary effect. The temperature and stress distribution adjacent to the laser spot vary along the thickness direction during the cleaving process; therefore, the calculation was considered as a three-dimensional problem. The specimen size used in this study was 20 mm x 10 mm x 0.5 mm. The half-part of the specimen with a coordinate system is shown in Fig. 6-20.

The following basic assumptions for the thermo-mechanical analysis were considered. The material properties, such as heat-transfer properties and mechanical properties, were assumed to be constant as the temperature range was not high. The stress-strain relationship of the silicon wafer was assumed to be perfectly elastic. Convection conditions were assumed to exist at all boundaries except on the surface  $x$ - $z$  plane ( $y=0$ ). This surface was considered to be in adiabatic condition. The energy absorbed by the silicon wafer during laser irradiation varies along the material thickness. The absorption characteristic is represented by the Beer-Lambert equation below [6]:

$$\beta = \frac{-\ln T}{x} \quad (1)$$

where  $T$  is the spectral transmittance ( $T=23\%$  as measured experimentally),  $\beta$  is the absorption coefficient and  $x$  is the thickness of the wafer. The boundary condition of the stress analysis was traction-free at all surfaces, and the  $x$ - $z$  surface was set as a fixed plane with zero displacement in the  $y$ -direction.

During the laser irradiation, a moving laser beam with power output of 70 W and laser-beam spot size of 0.25 mm x 0.19 mm was set on the wafer surface above the focal plane. When the center of the laser beam reached the wafer leading edge (i.e.,  $x=y=z=0$ ), the time was considered as  $t=0$  s, later moving in the  $x$ -direction at a constant speed of  $v=2$  mm/s. The initial temperature of the silicon-wafer substrate and the surrounding temperature were set to  $20^\circ\text{C}$ . The analysis was carried out in two phases. The transient temperature analysis was calculated when the moving laser beam was irradiated onto the silicon wafer. Then, the steady-state stress analysis was performed using the temperature distribution results at a specific point in time. The analysis condition and properties of the silicon wafer are summarized in Table 6-5.

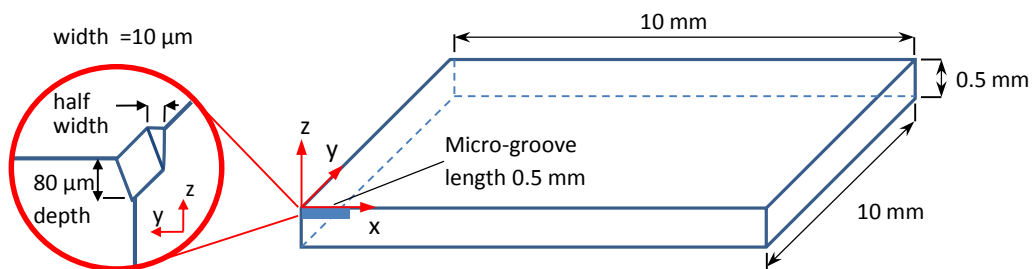


Fig. 6-20 Cross-section of the specimen with a coordinate system

Table 6-5 Analysis condition and properties of silicon wafer [7]

Analysis conditions		Units
Workpiece size	20×10×0.5	mm <sup>3</sup>
Laser beam diameter (oval)	0.25 x 0.19	mm/s
Heat transfer coefficient , $h$	8	Wm <sup>-2</sup> K <sup>-1</sup>
Initial temperature, $T_o$	20	C
Laser beam scan speed, $v$	2	mm/s
Laser power , $P$	70	W
Properties		
Thermal conductivity, $K$	156	W/m•K
Specific heat, $C$	761	J/kg•K
Thermal expansion coef., $\alpha$	2.62 x10 <sup>-6</sup>	K <sup>-1</sup>
Young modulus, $E$	169	GPa
Poisson ratio, $\nu$	0.262	
Density, $\rho$	2340	kg/m <sup>3</sup>

#### 6.4.1 Temperature and thermal-stress distributions

The transient temperature distributions were calculated at points in time from 0 to 0.495 seconds. The temperature distribution at various times is shown in Fig. 6-21. The temperature was measured on the surface of the material along the  $x$ -axis ( $y=0$ ,  $z=0$ ). The maximum temperatures at 0 s, 0.275 s and 0.495 s were 230°C, 380°C and 320°C, respectively. The calculated temperatures are consistent with those from the experimental results (Fig. 6-8).

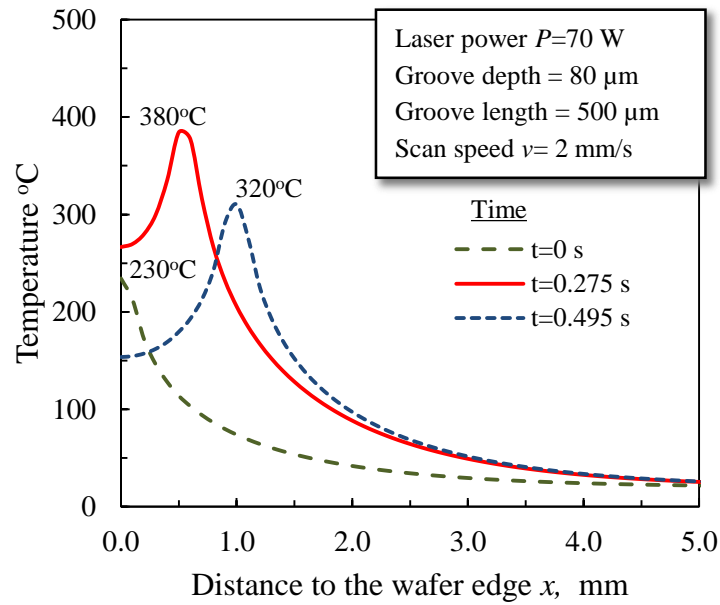


Fig. 6-21 Temperature distribution of moving laser spot at  $t=0$  s, 0.275 s and 0.495 s

The thermal-stress ( $\sigma_{yy}$ ) distribution along the cleaving plane at 0.01 s, 0.055 s, 0.165 s, 0.275 s, 0.385 s and 0.495 s is shown in Fig. 6-22. When the laser beam was at the position of  $x=0$  and the time of  $t=0$  s, the stress at the groove tip ( $z=-80$   $\mu\text{m}$ ) on the edge was a compressive stress. The thermal stress then changed from compression to tension in a short time when the laser beam moved forward in the  $x$ -axis direction. As the laser beam moved further, large tensile stress was accumulated at the groove tip ( $x=0$ ). This large tensile stress ( $\sigma_{yy}$ ) may induce a fracture when the stress reaches the fracture strength of the material. The fracture could be induced along the thickness direction ( $z$ -axis) and extended through the material. The tensile stress occurred after the laser beam passed through; thus, the fracture follows the laser spot with a short lagging distance.

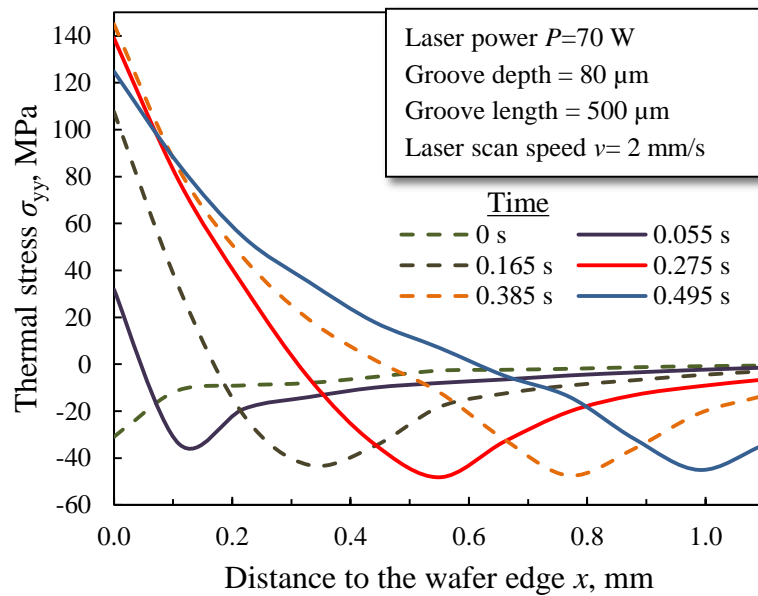


Fig. 6-22 Thermal stress ( $\sigma_{yy}$ ) distribution of moving laser beam at various times ( $z=-80 \mu\text{m}$ )

#### 6.4.2 The influence of groove length

The experimental result shown in Fig. 6-18 indicates that in the case of a wafer with a groove length of  $500 \mu\text{m}$ , the fracture initiation time was attained at approximately  $t=0.275 \text{ s}$ . At this time, the laser beam reached  $x=0.55 \text{ mm}$ . For the purpose of assessment, analysis of stress distribution for various cases of groove length was performed at the same time of  $0.275 \text{ s}$ .

Fig. 6-23 shows the thermal-stress ( $\sigma_{yy}$ ) distribution on the  $x$ - $z$  plane where  $y=0$  for groove length of  $100 \mu\text{m}$ ,  $300 \mu\text{m}$  and  $500 \mu\text{m}$  at  $t=0.275 \text{ s}$ . It can be seen that the thermal stress ( $\sigma_{yy}$ ) distributions in the  $x$ -direction for the three cases were almost similar, except for the area under the groove. Compressive stress was centered on the laser spot area, and tensile stress resulted in the area near to the edge of the material, where  $x=0 \text{ mm}$ . However, the maximum tensile stress was concentrated on the groove tip at the edge of the material ( $x=0$ ,

$z=-80\text{ }\mu\text{m}$ ) with more than 60 MPa tensile stress. The figures on the left of Figs. 6-23(a), (b) and (c) illustrate the thermal-stress distribution ( $\sigma_{yy}$ ) along the  $z$ -axis ( $x=0, y=0$ ). The results indicate that the thermal stress ( $\sigma_{yy}$ ) is at its maximum at the groove tip ( $z=-80\text{ }\mu\text{m}$ ) and reduces rapidly when it moves in the  $-z$  direction, before reaching approximately 40 MPa of constant tensile stress. The relationship between the maximum thermal stress and groove length is shown in Fig. 6-24. It was found that the proportion of the tensile stress concentrated on the groove tip was dependent on the groove length. Longer groove length resulted in a higher concentration of thermal stress ( $\sigma_{yy}$ ).

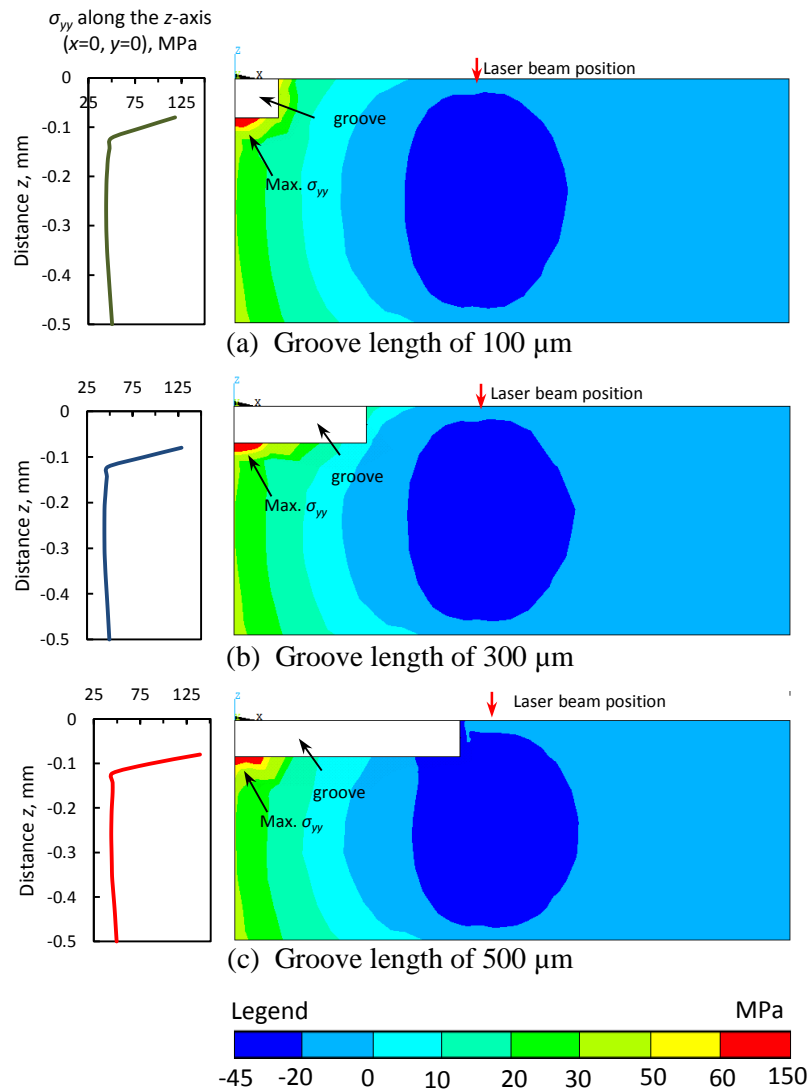


Fig. 6-23 Thermal stress ( $\sigma_{yy}$ ) distribution on  $x$ - $z$  plane at  $y=0$  and varied groove length ( $t=0.275\text{ s}$ )



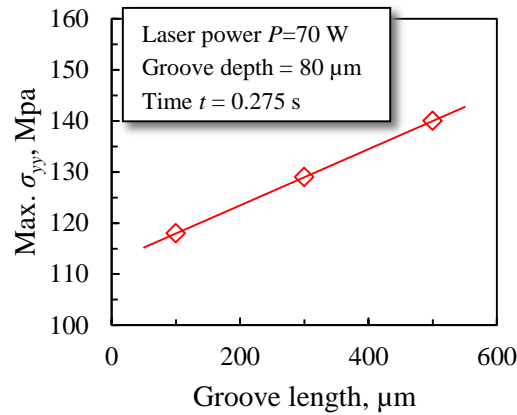


Fig. 6-24 Relationship between thermal stress ( $\sigma_{yy}$ ) and groove length

### 6.4.3 The influence of groove depth

Fig. 6-25 shows a comparison of thermal-stress ( $\sigma_{yy}$ ) distributions on the  $x$ - $z$  plane ( $y=0$ ) of the wafer with groove depth of 20  $\mu\text{m}$ , 50  $\mu\text{m}$ , and 120  $\mu\text{m}$  at 0.275 s. Fig. 6-23(a) illustrates that the thermal stress ( $\sigma_{yy}$ ) was distributed along the  $x$ -direction. Compressive stress was focused under the laser-beam position ( $x=0.55$  mm) and tensile stress resulted at the edge of the material ( $x=0$  mm). Large tensile stress of more than 60 MPa was concentrated on the groove tip ( $z=20$   $\mu\text{m}$ ,  $x=0$  mm). Moreover, this phenomenon was repeated for groove depth of 50  $\mu\text{m}$  and 120  $\mu\text{m}$ , as illustrated in Figs. 6-25(b) and (c), respectively. The maximum tensile stress was concentrated on the groove tip for both cases.

The figures on the left of Figs. 6-25(a), (b) and (c) illustrate the thermal-stress distribution ( $\sigma_{yy}$ ) along the  $z$ -axis ( $x=0$ ,  $y=0$ ). The results indicate that the thermal stress ( $\sigma_{yy}$ ) is highest at the groove tip and reduces rapidly to a constant tensile stress of approximately 40 MPa along the  $-z$  direction. The relationship between the maximum thermal stress at the groove tip and the groove depth is shown in Fig. 6-26. A deeper groove resulted in higher thermal-stress concentration.

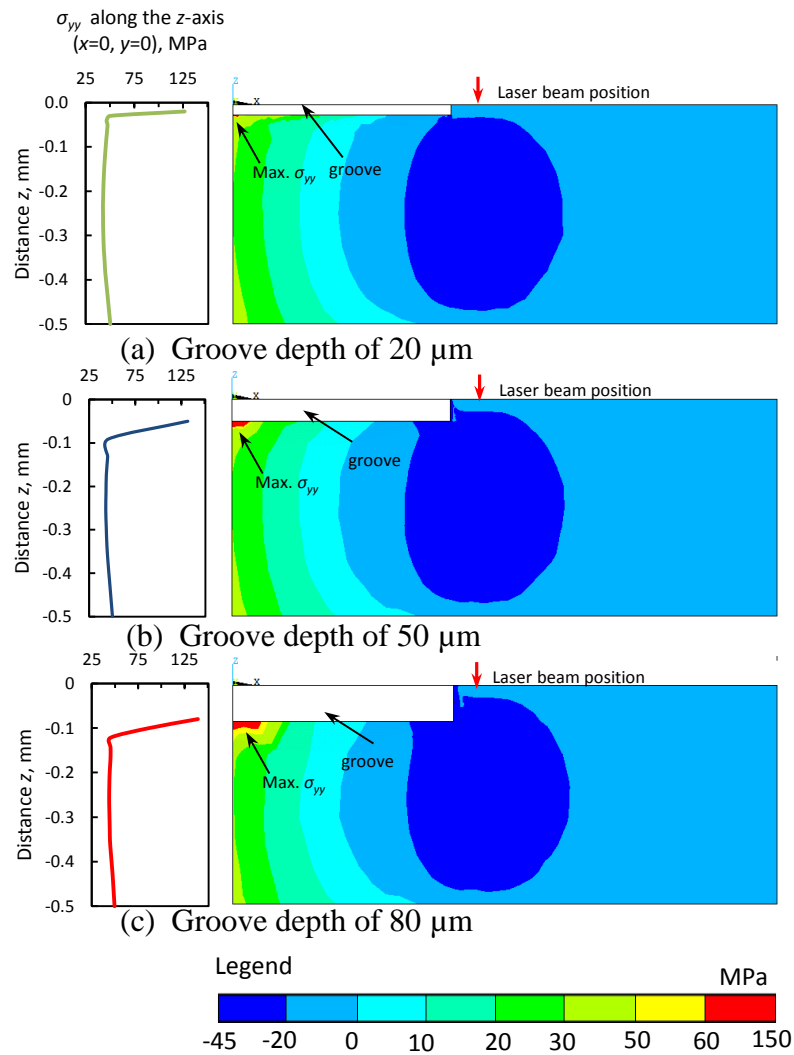


Fig. 6-25 Thermal-stress ( $\sigma_{yy}$ ) distribution on  $x$ - $z$  plane at  $y=0$  and varied groove depth ( $t=0.275$  s)

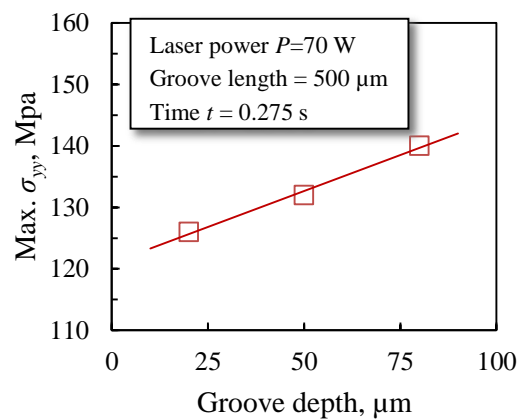


Fig. 6-26 Relationship between thermal stress ( $\sigma_{yy}$ ) and groove depth

## 6.5 STRESS INTENSITY FACTOR

The stress intensity factor,  $K_I$ , is used to estimate the stress condition at the area of the micro-groove caused by thermal stress induced via laser energy. When the stress condition reaches the fracture strength of the material, a fracture may grow. The stress intensity factor,  $K_I$ , is a parameter that clarifies the magnitude of the applied stress, including the geometrical parameter of load type. These load types are categorized as modes I, II, and III, representing the three basic modes of crack tip deformation, illustrated in Fig. 6-27. The most common type leading to brittle failure is type-I loading (opening mode) [8], which is considered in this study.

Irwin defined a polar coordinate axis with the origin at the crack tip, as shown in Fig. 6-28, and determined that the stress field  $\sigma(r, \theta)$  at the vicinity of a groove tip could be described mathematically as in equation 2 [9]. Considering that initial fracture occurs according to the crack mode I, and  $\theta = 0^\circ$ ,  $K_I$  can be determined by using equation 3:

$$\sigma_{yy} = \frac{K_I}{\sqrt{2\pi r}} \cos \frac{\theta}{2} \left( 1 - \sin \frac{\theta}{2} \sin \frac{3\theta}{2} \right) \quad (2)$$

$$K_I = \sigma_{yy} \sqrt{2\pi r} \quad (3)$$

where  $\sigma_{yy}$  is the magnitude of local stress at distance  $r$  from the groove tip.

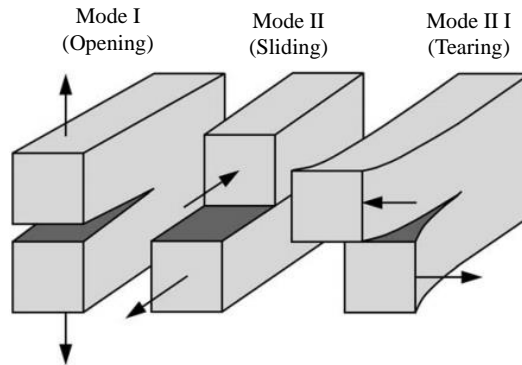


Fig. 6-27 Basic modes of crack tip deformation

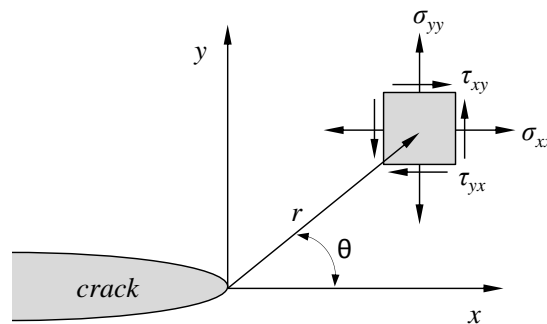


Fig. 6-28 Definition of coordinate axis ahead of a crack tip

### 6.5.1 Determining stress intensity factors using the finite-element method

In this study, the finite-element method is used for determining the state of stress at the crack tip. The finite-element solution uses the values for local stresses and the displacements at predetermined node coordinates. The local stress ( $\sigma_{yy}$ ) at coordinates  $(r, \theta)$  can be used to determine the stress intensity factor  $K_I$ . The stress at the node that corresponds to the location of the crack tip ( $r=0$ ) cannot be used because the stress is originated there. Therefore, the stress should be determined away from the crack tip, outside

the plastic zone, or, more correctly, the ‘nonlinear’ zone [8]. However, values relating to points too far from the crack tip cannot be used, since equation 3 applies only for small values of  $r$ . In this study ( $\sigma_{yy}$ ) is measured at a constant  $r=20\ \mu\text{m}$ .

Fig. 6-29 shows the thermal-stress distribution ( $\sigma_{yy}$ ) on the  $x$ - $z$  plane at the time  $t=0.275\ \text{s}$ , while the figure on the left displays  $\sigma_{yy}$  along the  $-z$  direction ( $x=0$ ). During laser irradiation, tensile stress was accumulated at the edge of the silicon wafer and concentrated at the position  $x=0, z=-80\ \mu\text{m}$ . The tensile stress was increased with the increase of irradiation time. The variation of thermal stress ( $\sigma_{yy}$ ) distribution with time is shown in Fig. 6-30. Initial fracture occurs when the stress condition reaches the fracture toughness of the material, and the fracture begins in the  $-z$  direction due to the tensile-stress gradient. The stress intensity factor,  $K_I$ , was calculated based on the measurement of thermal stress ( $\sigma_{yy}$ ) at constant distance  $r=20\ \mu\text{m}$  from the figure. This calculation was repeated for various groove lengths and depths.

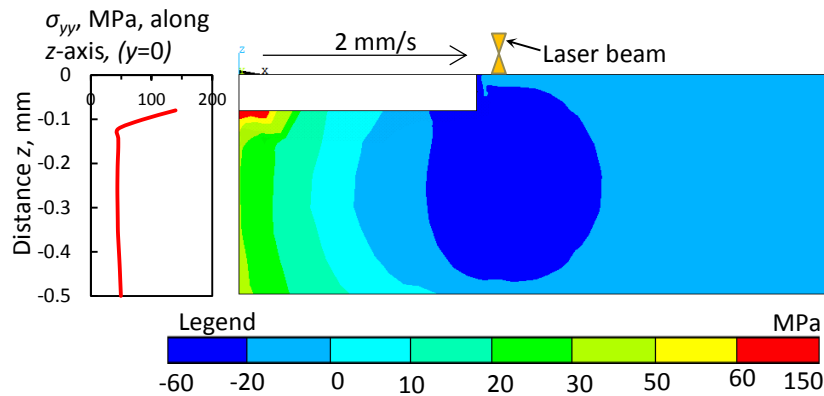


Fig. 6-29 Thermal stress ( $\sigma_{yy}$ ) distribution on  $x$ - $z$  plane at  $t=0.275\ \text{s}$  (groove length  $500\ \mu\text{m}$ , depth  $80\ \mu\text{m}$ )

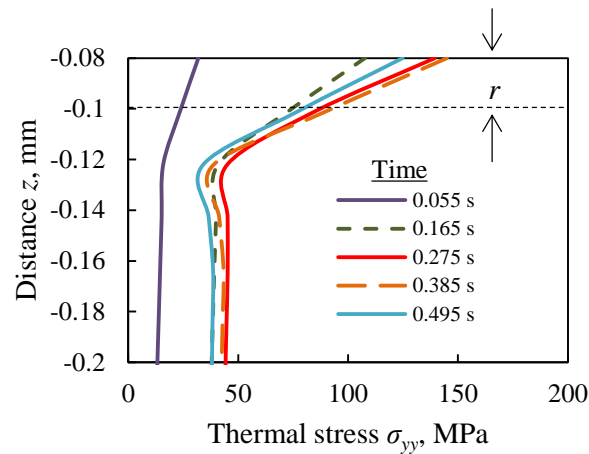


Fig. 6-30 Variation of thermal stress ( $\sigma_{yy}$ ) with time along  $z$  direction ( $x=0$ )

Fig. 6-31 and Fig. 6-32 illustrate the relationship between  $K_I$  and laser irradiation time for various groove lengths and groove depths, respectively. It was found that  $K_I$  increased relatively with time until reaching its maximum at approximately  $t=0.34$  s. When the fracture toughness,  $K_{IC}$ , was achieved, fracture was initiated. The fracture toughness value,  $K_{IC}$ , was experimentally determined and this is discussed in the next section.

From Fig. 6-31, it can be seen that  $K_I$  increased with the irradiation time and slowly decreased after the irradiation temperature was reduced. This was because the amount of thermal stress employed on the groove was dependent on the temperature supplied by the laser beam. It was shown that when longer grooves were used,  $K_{IC}$  was achieved earlier. A similar phenomenon was shown for the groove depth results, shown in Fig. 6-32. If the groove length or depth is too small, material fracture cannot occur.

The results showed that the groove parameters had a significant influence on the fracture initiation time. Fracture initiation time decreased with the increase of groove size.

The minimum groove size for fracture initiation was found to be 100  $\mu\text{m}$  and 20  $\mu\text{m}$  for length and depth, respectively.

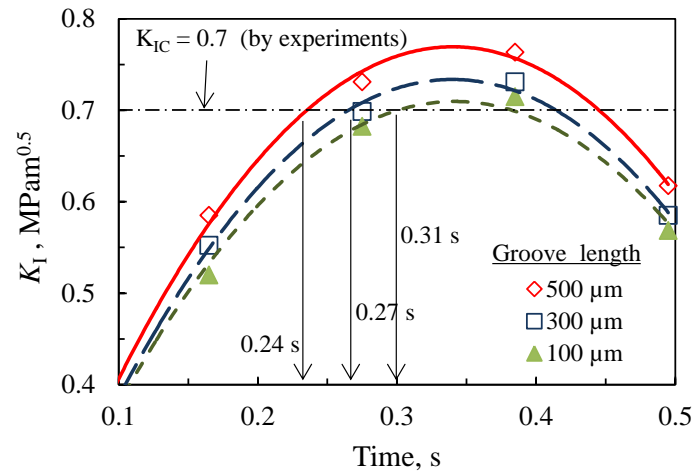


Fig. 6-31 Stress intensity factor,  $K_I$ , vs. time at different groove lengths (depth=80  $\mu\text{m}$ )

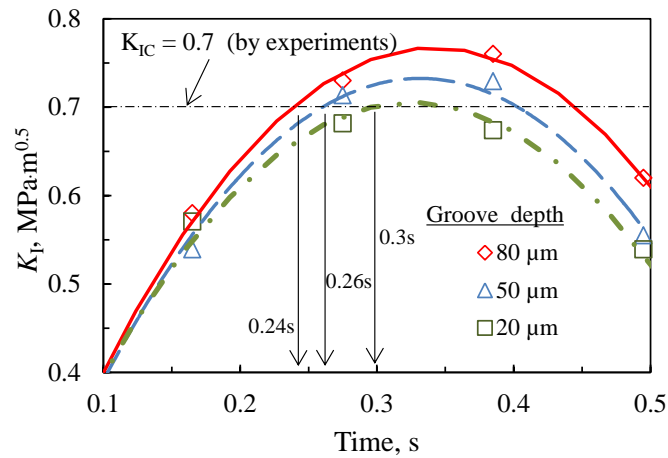


Fig. 6-32 Stress intensity factor,  $K_I$ , vs. time for different groove depths (length=500  $\mu\text{m}$ )

## **6.6 COMPARISON BETWEEN THE FRACTURE INITIATION TIMES OF FEM AND EXPERIMENTAL RESULTS**

The variation of fracture initiation times with groove length and depth based on the FEM and experimental analysis are shown in Fig. 6-33(a) and Fig. 6-33(b), respectively. The experimental results are taken from the previous section. The FEM results show correlation with the experimental results. Fracture initiation time decreased with increased groove length and depth. However, fracture initiation was achieved faster in the FEM results compared to the results from the experiments. For instance, in Fig. 6-33(a), at the groove length of 200  $\mu\text{m}$ , the fracture initiation time obtained from the FEM result is 280 ms, compared to 380 ms from the experimental result. From Fig. 6-33(b), the fracture initiation times achieved at a groove depth of 50  $\mu\text{m}$  are about 250 ms and 350 ms for the FEM and the experimental results, respectively.

In the FEM analysis, ideal conditions were considered in contrast to the actual situation during experimental work. During FEM analysis, material properties such as heat-transfer properties and mechanical properties were assumed to be constant. The stress-strain relationship of the silicon wafer was assumed to be perfectly elastic. Moreover, the FEM model of the micro-groove was created with a sharp micro-groove tip. In the real situation, the micro-groove was produced with a blunt or round groove tip; a sharp groove could not be produced. The fracture is easier to initiate with a sharper groove tip due to the higher stress concentration; this is why fracture initiation was achieved earlier in the FEM analysis.



Even though different fracture initiation times resulted from FEM and experimental analysis, the relationship between fracture initiation and groove parameters was clearly evidenced by the FEM results.

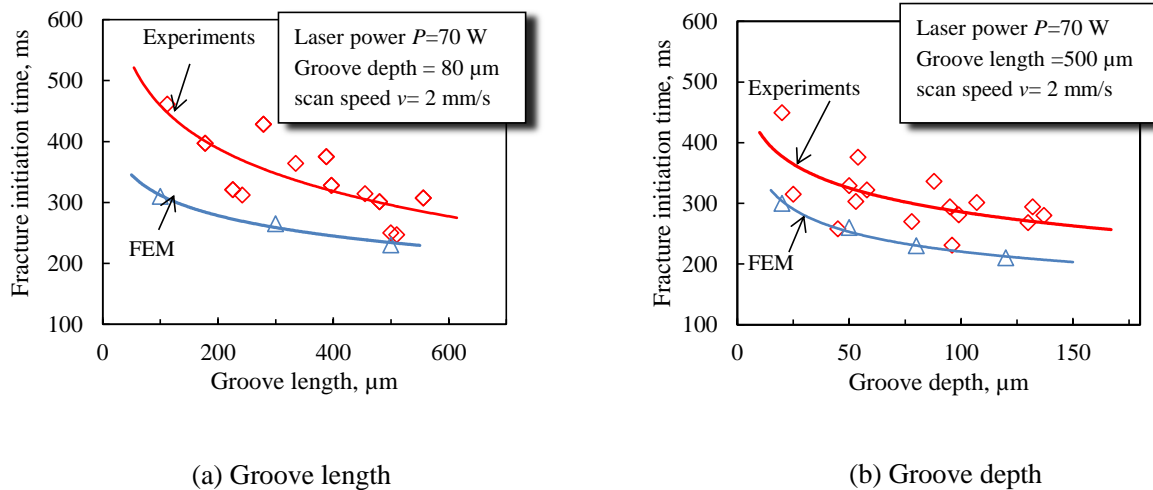


Fig. 6-33 Fracture initiation time from FEM results:  
(a) groove length; (b) groove depth

## 6.7 DETERMINATION OF FRACTURE TOUGHNESS

The fracture toughness,  $K_{IC}$ , describes the ease of propagation of a fracture or defect in a material. The linear-elastic fracture toughness of a material is determined from the stress intensity factor ( $K_I$ ) at which a crack in the material begins to grow. Fracture toughness is a quantitative way of expressing a material's resistance to brittle fracture when a crack is present.

In this study, fracture toughness,  $K_{IC}$ , of the Si-wafer is estimated by using the Vickers indentation technique. The technique is simple and cost effective. The analysis relies on the evaluation of the indenter's effect in the material. Small surface cracks with controlled size and shape are created by the Vickers indenter. Fig. 6-34 shows an optical micrograph of a 0.3 kgf Vickers indentation in a P-type Si wafer (100) indicating the contact features.

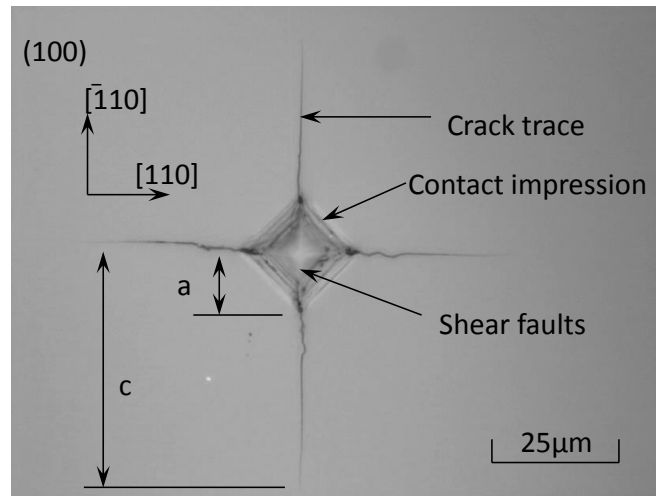


Fig. 6-34 Optical micrograph of a Vickers indentation

The relationship between  $K_{IC}$  and Vickers impression has been described by Evan and Charles [10] as shown in equation 4, with hardness ( $H_v$ ) expressed as in equation 5.

$$K_{IC} = 0.13 H_v \sqrt{a} \left[ \frac{c}{a} \right]^{-3/2} \quad (4)$$

$$H_v = 4.5465 \times 10^{-3} \frac{W}{a^2} \quad (5)$$

where  $K_{IC}$  is fracture toughness ( $\text{MPa}\cdot\text{m}^{0.5}$ ),  $H_V$  is Vickers hardness (GPa),  $a$  is the half-diameter of the sample's indentation section (m),  $c$  is the crack length (m) and  $W$  is the indentation load (kgf). The experiment was performed according to ASTM C1327-08. Indentation was performed using a micro-Vickers-hardness-testing machine (Akashi HM-101) with a dwell time of 15 s; indentation was repeated 10 times as stated in the ASTM measurement standard.

The loading used in this experiment was varied between 0.1, 0.2 and 0.3 kgf. The measurement of the half-diameter of the sample's indentation section and crack length on the wafer was performed by using Scanning Electron Microscopy (SEM). Fig. 6-35 shows the result of hardness,  $H_V$  (8.9 GPa), while Fig. 6-36 shows the average results of fracture toughness,  $K_{IC}$  (about  $0.7 \text{ MPa}\cdot\text{m}^{0.5}$ ).

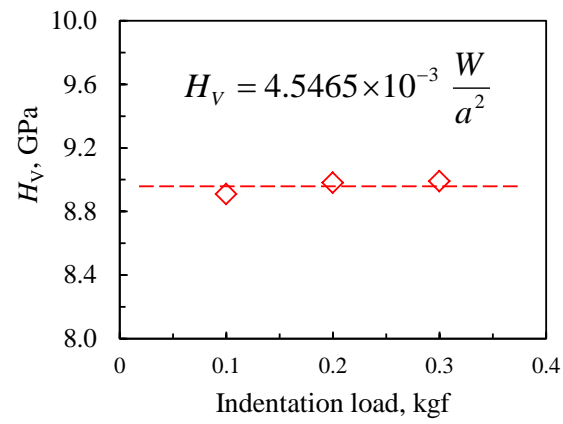


Fig. 6-35 Hardness,  $H_V$ , of Si wafer.

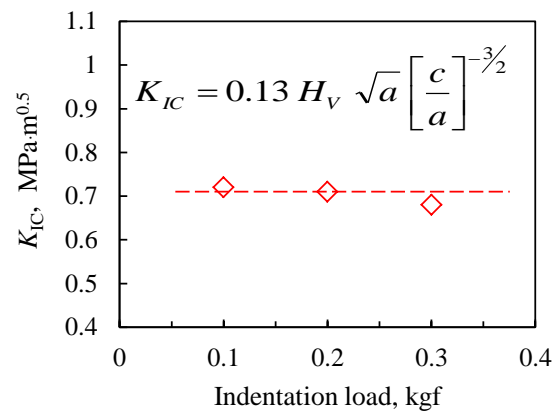


Fig. 6-36 Fracture toughness,  $K_{IC}$ , of Si wafer.

## 6.8 SEPARATING MECHANISM OF SILICON WAFER

Based on the results of the experimental and computational analysis, the mechanism for separating a silicon wafer by applying a laser beam using the thermal-stress cleaving process can be understood clearly. Fig. 6-37 illustrates the separating mechanism of the silicon wafer with a pre-prepared micro-groove utilizing the moving laser beam. The cleaving process can be divided into two stages, namely, fracture initiation and intermittent crack propagation.

As shown in Fig. 6-37(a), fracture does not occur when the laser reaches the edge of the wafer. This is due to the fact that the laser beam induces heat in the laser spot area; hence, a compressive stress is generated at this point. After the laser beam moves further, the compressive stress changes into tensile stress. The tensile stress is concentrated at the groove tip, and it increases with the increase in temperature at the laser spot and the distance relative to the leading edge of the wafer. As the intense stress at the groove tip reached the material fracture strength, fracture was initiated throughout the material thickness and extended towards the laser spot in a very short time. As illustrated in Fig. 6-37(b), the fracture stopped before the laser-beam spot created a new crack tip. Continuous heat supplied by the laser beam caused the tensile stress to increase on the newly created crack tip, and the crack propagated and stopped again before the laser spot. As shown in Fig. 6-37(c), the cleaving mark was created as the crack stopped. This process was replicated again and again until the laser beam reached the end of the wafer.

It is demonstrated that fracture initiation and intermittent crack propagation occurrence are influenced by the heat supplied from the laser beam during the irradiation process. An increase in laser power improved the fracture initiation time and increased crack propagation

recurrence. However, the laser power should be controlled to avoid any thermal damage to the silicon wafer.

Fracture initiation and crack propagation produced cleaving mark waves on the separating surface. The cleaving mark wave was consistent with the AE signals. The groove parameters had a significant influence on the fracture initiation times. The increase of groove size shortened the fracture initiation time. However, larger groove size required more energy and caused more damage to the cleaving surface. Therefore, a minimum size of groove is preferred.

The application of a micro-groove therefore aimed to facilitate the cleaving process of the wafer material. Material separation was achieved similarly to crack extension, the crack being extended from the micro-groove tip. By introducing the micro-groove, damage at the starting edge of the wafer material can be minimized. Without the micro-groove, fracture initiation is difficult to achieve, as there is no weak point in the material. For this reason, higher laser energy is required to start the fracture from the edge of the wafer material. The fracture happens due to the unstable condition and cannot be controlled.

In this study, the mechanism of fracture initiation of the silicon wafer with micro-groove has been discovered. Fracture initiation is important in separating the wafer material because it determines aspects such as minimum laser power needed, practical size of micro-groove and cleaving-surface finish. The fracture extension was evidenced by the AE signals and the cleaving-surface features. The FEM results showed the heat and thermal-stress conditions during the laser irradiation. The findings are important for industrial practitioners and researchers and can be used in improving current silicon-wafer processing and further investigations in the future.

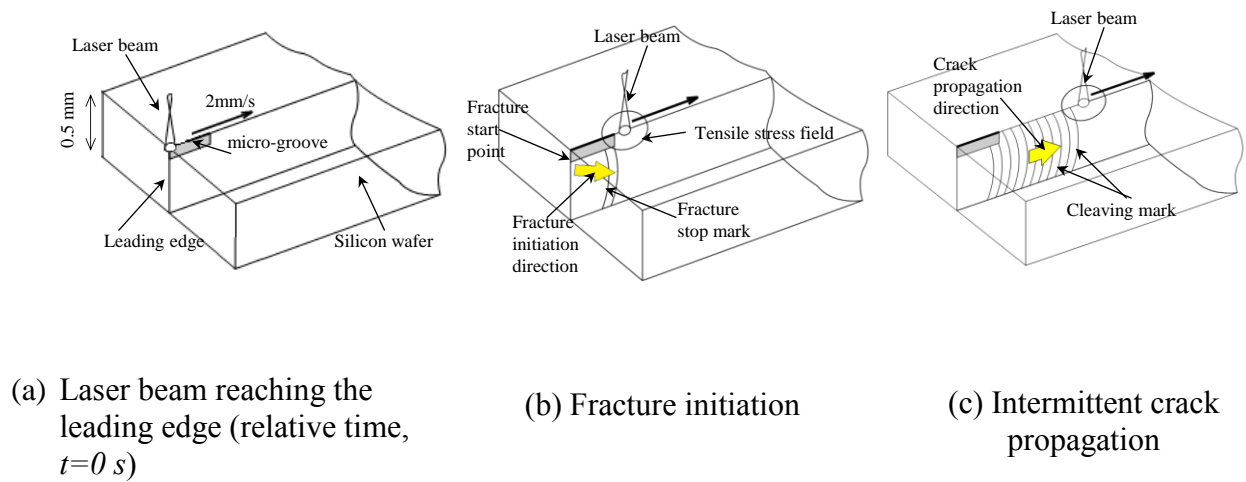


Fig. 6-37 Thermal-stress cleaving mechanism of silicon wafer with micro-groove

## 6.8 CONCLUSION

The separating characteristics of a silicon wafer with a moving Nd:YAG laser using the thermal-stress cleaving technique were successfully monitored and analyzed by the utilization of a two-color pyrometer with an optical fiber and AE sensor. Computational analysis by the finite-element method explained the phenomenon of stress distribution during the process. Based on the results obtained, the mechanism of the thermal-stress cleaving of a silicon wafer with a laser beam was explained.

The separating process of the silicon wafer occurs in two stages. The first stage is the fracture initiation, where the fracture occurs due to tensile stress concentrated at the groove tip on the edge of the specimen. The second is intermittent crack propagation, which occurs at constant intervals in time.

Temperature at the laser irradiation area was related to the cleaving technique and shown to influence the cleaving achievement and cleaving-surface quality. Fracture initiation and crack propagation produced cleaving mark waves on the separating surface. The cleaving mark wave was consistent with the AE signals.

The finite-element (FEM) analysis results explained the stress distribution during laser irradiation. By using FEM, the stress condition was determined quantitatively by identifying the stress intensity factor,  $K_I$ . The fracture toughness,  $K_{IC}$ , of the material was determined experimentally using the Vickers indentation technique.

In thermal-stress cleaving, a pre-prepared micro-groove is important to control the start of the fracture. Groove size was shown to have a significant influence on the fracture initiation time. By estimating the stress intensity factor at the groove, the minimum effective dimensions of the micro-groove were suggested.



**REFERENCES**

- [1] T. Ishikawa, T. Ueda, T. Furumoto, Hosokawa, A., Tanaka, R. “Pre-groove development for laser cleaving of brittle materials by using micro-lens,” *Journal of Advanced Mechanical Design, Systems, and Manufacturing*, 6(6), pp. 841-848, 2012.
- [2] T. Ueda, K. Yamada, and K. Nakayama, “Temperature of work materials irradiated with CO<sub>2</sub> laser,” *CIRP Ann. - Manuf. Technol.*, vol. 46, no. 1, pp. 117-122, 1997.
- [3] T. Ueda, K. Yamada, K. Oiso, A. Hosokawa, “Thermal stress cleaving of brittle materials by laser beam,” *CIRP Annals - Manufacturing Technology*, 51(1), pp. 149-152, 2002.
- [4] K. Yamada, T. Ueda, A. Hosokawa, Y. Yamane, K. Sekiya, “Thermal damage of silicon wafer in thermal cleaving process with pulsed laser and CW laser,” *Proc. SPIE Laser-based Micro packaging*, 6107, pp. 61070H-61070H-10, 2006.
- [5] J. Liu, J. Lu, X. Ni, G. Dai, L. Zhang, Y. Chen, “Numerical study on thermal stress cutting of silicon wafer using two-point pulsed laser,” *Optica Applicata*, 41(1), pp. 247-255, 2011.
- [6] K. A. Elijah, “*Principles of laser materials processing*,” John Wiley & Sons Inc., New Jersey, pp. 14-17, 2009.
- [7] A. Masolin, P. Bouchard, R. Martini and M. Bernacki, “Thermo-mechanical and fracture properties in single-crystal silicon,” *J. Material Science*, 48, pp. 979-988, 2013.
- [8] C. Fischer, C. Anthony, *Introduction to contact mechanics*, second edition, Springer Science, pp.31-48, 2007.
- [9] G. R. Irwin, “Analysis of stresses and strains near the end of a crack traversing in a plate,” *J. Appl. Mech.*, 24, pp. 361-364, 1957.
- [10] A. G. Evans, E. A. Charles, “Fracture toughness determinations by indentation,” *J. American Ceramic Society*, 59: 371-372, 1976.

## **CHAPTER 7: INVESTIGATION OF LASER CLEAVING OF SAPPHIRE WAFER BY CO<sub>2</sub> LASER**

### **7.1 INTRODUCTION**

Single-crystal sapphire in general possesses excellent properties of high strength, high rigidity, good electrical insulation, good thermal conductivity and excellent optical transparency to visible light. It has been used in a wide range of industries due to its unique features. In particular, sapphire substrates are being used to produce the new generation of LED lighting, which offers lower power consumption and longer lifespan. Sapphire crystal has also been applied in cell-phone camera lenses and premium-watch covers to give shatterproof and scratch-resistant characteristics.

With the increase in demand for sapphire substrate applications, informed selection of processing techniques is necessary to ensure product quality and process efficiency. Thermal-stress cleaving with a laser beam is one technique that has been applied in sapphire processing [1,2]. In this technique, material is divided by extending the fracture via thermal stress generated by a laser beam; material separation is similar to crack extension. The process produces an excellent surface finish, does not produce machining chips and does not require a machining liquid.

Several investigations of thermal-stress cleaving using a CO<sub>2</sub> laser have already been performed on sapphire wafer [3,4,5,6], providing analysis of experimental works. It has been reported that heat damage can be avoided by establishing appropriate laser irradiation conditions. However, the thermal-stress condition inside the material during laser irradiation is yet to be verified.

In this chapter, the finite-element method (FEM) is used to analyze the thermal-stress conditions during irradiation of a sapphire wafer with a CO<sub>2</sub> laser. The thermal-stress distribution during laser-beam irradiation is different when compared to the case of the silicon wafer irradiated with the Nd:YAG laser presented in the previous chapter, due to different laser energy-absorption characteristics. Furthermore, the material properties and laser energy absorption of these two materials are different. This chapter reports a temperature transient analysis simulating the laser irradiation on the sapphire wafer. Then, a steady-state stress analysis is executed and evaluated using the temperature distribution results for a particular point in time.

### 7.2 MATERIAL PROPERTIES

Table 7-1 shows the physical properties of the sapphire used in this study, as compared to the silicon wafer used in the previous chapter. Sapphire is a superior material compared to silicon: it has about twice the hardness and density and about three times the fracture toughness and Young's modulus. In terms of thermal properties, the expansion coefficient of sapphire is almost two times that of silicon. However, the thermal conductivity and thermal diffusivity of silicon is higher, by approximately four and six times, respectively. The linear expansion coefficient indicates the magnitude of the material expansion generated by heat.

Thermal conductivity indicates the extent to which the heat is distributed in the material and fracture toughness indicates the required stress for the crack growth.

The governing equation that describes the thermal stress resulting from the temperature difference,  $\Delta T$ , is given by equation 1 [7].  $E$  is the Young's modulus, and  $\beta$  and  $\nu$  are the coefficient of linear expansion and Poisson ratio, respectively. The magnitude of thermal stress is caused by the temperature difference, and is dependent on Young's modulus, thermal expansion coefficient and Poisson ratio of the material.

$$\sigma_{therm} = \frac{E\beta\Delta T}{1-\nu} \quad \dots (1)$$

The heat generated by laser irradiation on sapphire is easily accumulated at the point of irradiation, and thus produces a greater temperature difference due to the lower thermal diffusivity properties of the sapphire material; in the case of silicon, the heat is defused to the area around the irradiation point. Therefore, the thermal stress generated on sapphire could be higher. Nevertheless, since sapphire has higher fracture toughness, fracture development is difficult.

Table 7-1 Thermal physical properties of sapphire and silicon

Thermal physical property	Sapphire	Si-wafer	Units
Density, $\rho$	$3.97 \times 10^3$	$2.34 \times 10^3$	kg/m <sup>3</sup>
Young modulus, $E$	470	169	GPa
Vickers hardness, $H_v$	19	8.9	GPa
Fracture toughness, $K_{IC}$	1.96	0.7	MPa · m <sup>1/2</sup>
Thermal expansion coef., $\alpha$	$5.3 \times 10^{-6}$	$2.6 \times 10^{-6}$	K <sup>-1</sup>
Thermal conductivity, $K$	42	156	W/m · K
Thermal diffusivity, $k$	$141 \times 10^{-7}$	$800 \times 10^{-7}$	m <sup>2</sup> /s
Specific heat, $C$	0.75	0.76	J/g · K
Poisson ratio, $\nu$	0.3	0.26	

### 7.3 LASER ENERGY ABSORPTION CHARACTERISTIC

In the previous chapter, it was found that the energy absorption of the Nd:YAG laser used with silicon material was absorbed into a volumetric form of absorption, with some of the laser intensity being transmitted through the medium. However, for the sapphire wafer, almost all the energy of the CO<sub>2</sub> laser is absorbed on the material's surface. Spectral transmittance through the material is nearly zero.

The spectral transmittance of the medium is related to laser wavelength and material type. The measurement of spectral transmittance was carried out by using two types of spectrometer for different wavelength ranges. The infrared spectrophotometer (Perkin Elmer Corp.: Spectrum One NTS) was used to measure the wavelength between 0.68 to 4.3  $\mu\text{m}$ ; FTIR imaging apparatus (VARIAN, Inc.: 3100FT- IR) was used between 2.5 to 25  $\mu\text{m}$ . Measurements were made on polished surface of sapphire wafer (0 0 0 1) of thickness 150  $\mu\text{m}$ .

Fig. 7-1 shows the spectral transmittance of the sapphire wafer (0 0 0 1) and silicon wafer (1 0 0). With the use of a CO<sub>2</sub> laser with a wavelength of 10.64  $\mu\text{m}$ , the transmittance is almost zero, indicating that the laser energy is absorbed fully by the material. However, when Nd:YAG laser (1.064  $\mu\text{m}$  wavelength) is used to irradiate the sapphire wafer, almost 90 percent of the laser energy is transmitted through the material. In contrast, when irradiating the silicon wafer with the Nd:YAG laser, the transmittance is only about 23 percent.

The absorption characteristic is represented by the Beer-Lambert equation (equation 2, below) [4].  $T$  is the spectral transmittance,  $\beta$  is the absorption coefficient and  $x$  is the thickness of the wafer. Equation 2 indicates that the laser intensity varies exponentially as it

propagates in the medium. By using the equation, the laser energy absorption relative to the thickness of the material can be found.

$$\beta = \frac{-\ln T}{x} \quad \dots\dots (2)$$

Fig. 7-2 illustrates the absorption characteristic of laser energy. Full laser energy absorption occurred when a CO<sub>2</sub> laser was used to irradiate the sapphire wafer. In contrast, when an Nd:YAG laser was used, only slight absorption took place. The variations of laser energy absorption along the thickness direction of sapphire and silicon materials are shown in Fig. 7-3. It is shown that the energy from the CO<sub>2</sub> laser is absorbed mainly on the surface of the sapphire material. In contrast, the laser energy of the Nd:YAG laser is absorbed through the silicon material. The laser absorption ratio shown in the figure for each layer of material thickness is used to assign the heat source during the finite-element analysis in the next section.

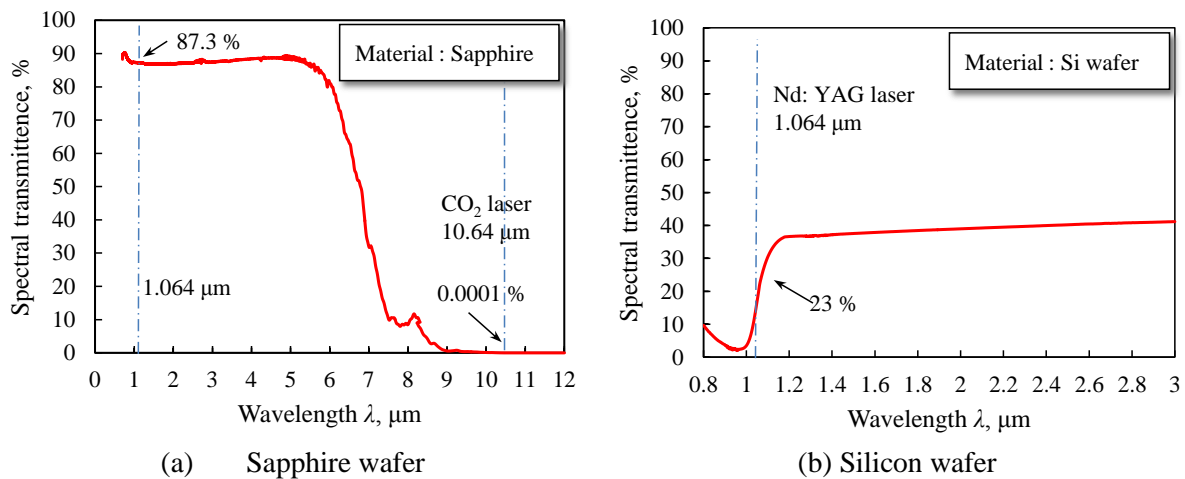


Fig. 7-1 Spectral transmittances of the sapphire wafer (0 0 0 1) and silicon wafer (1 0 0)

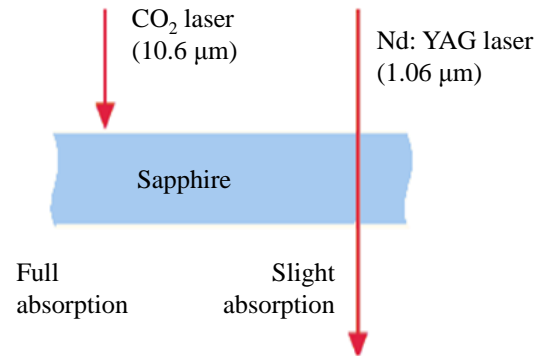


Fig. 7-2 Absorption of laser energy in sapphire material

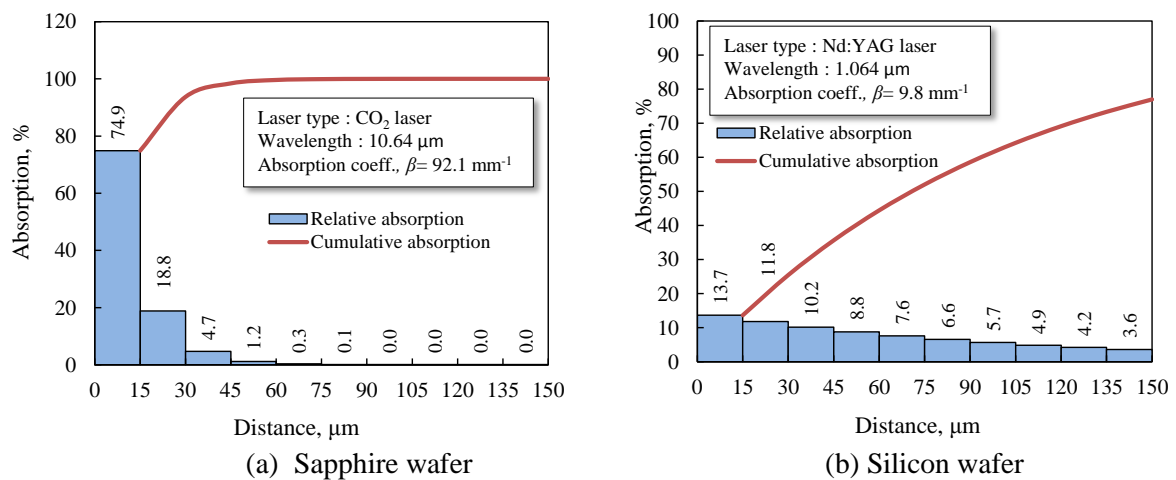


Fig. 7-3 Relationship between laser energy absorption and distance from the material surface

## 7.4 FINITE-ELEMENT ANALYSIS

Finite-element software (ANSYS) was used to analyze the behavior of thermal-stress cleaving during laser irradiation by considering the finite-boundary effect. The temperature and thermal-stress distribution around the laser spot diverged along the thickness direction of the substrate. Therefore, the finite-element model should be considered as a three-dimensional problem.

The specimen size used in this study was 6 mm x 6 mm x 0.15 mm. The half-part of the analysis model with a coordinate system is shown in Fig. 7-4. A groove of 15  $\mu\text{m}$  in depth and 5  $\mu\text{m}$  in width was created along the  $x$ -axis. The analysis model was formed as a symmetric model, so that the analysis element number could be minimized.

The following basic assumptions for the thermo-mechanical analysis were considered. The material properties such as the heat-transfer properties and mechanical properties were assumed to be constant as the temperature range was low. The stress-strain relationship of the silicon wafer was assumed to be perfectly elastic. Convection conditions were assumed to exist on all boundaries except at the surface of the  $x$ - $z$  plane ( $y=0$ ). This surface was considered to be in adiabatic condition.

During the laser irradiation simulation, a laser beam was moved along the  $x$ -axis with a scan speed of 5 mm/s. At  $t=0$  s, the laser beam was at the leading edge of the wafer (i.e.,  $x=y=z=0$ ). The initial temperature of the sapphire wafer and the surrounding temperature were both set to 20°C. The analysis was carried out in two phases. The transient temperature analysis was calculated during the movement of the laser beam irradiation on the wafer material. Then, the steady-state stress analysis was performed using the temperature distribution results at a specific point in time.



The analysis conditions of sapphire and silicon wafer are summarized in Table 7.2, while the thermal physical properties are given in Table 7.1. The laser-beam spot diameter used in the analysis was 0.3 mm. The heat-transfer coefficient used was  $8 \text{ Wm}^{-2}\text{K}^{-1}$  and the initial temperature was set to  $20^\circ\text{C}$ . During the laser irradiation process, reflection of laser energy was assumed not to occur. Meanwhile, the boundary condition during the steady-state stress analysis was set as traction-force-free on all surfaces except the  $x$ - $z$  surface; this surface was set as a fixed plane, indicating that the displacement in the  $y$ -direction was zero.

The effects of laser-energy-absorption coefficient  $\beta$  on sapphire and silicon were analyzed and compared. CO<sub>2</sub> lasers with a power of 3 and 6 W are used in cleaving the sapphire while an Nd:YAG laser of power 20 W is applied in cleaving the silicon material. The temperature and thermal-stress distribution for both materials are evaluated, and the mechanism of fracture initiation of each material is described in the next section.

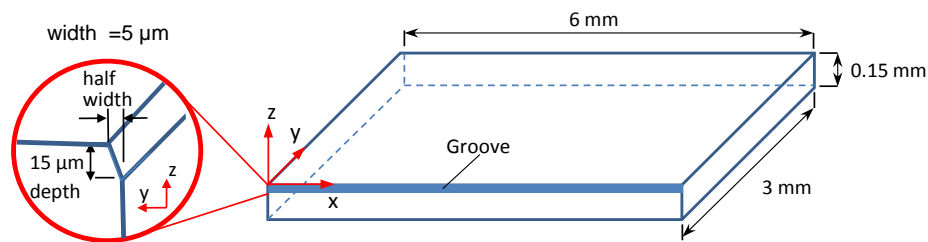


Fig. 7-4 Half-part of the analysis model with a coordinate system

Table 7-2 Analysis conditions of sapphire and silicon wafer

## CHAPTER 7: INVESTIGATION OF LASER CLEAVING OF SAPPHIRE WAFER BY CO<sub>2</sub> LASER

Analysis condition of Sapphire			Units			Analysis condition of Silicon			Units		
Laser type (continuous wave)	CO <sub>2</sub>					Laser type (continuous wave)	Nd:YAG				
Laser power, $P$	3, 6		W			Laser power, $P$	20		W		
Laser beam scan speed, $v$	5		mm/s			Laser beam scan speed, $v$	5		mm/s		
Workpiece size, $(a \times b \times d)$	6 x 6 x 0.15		mm			Workpiece size, $(a \times b \times d)$	6 x 6 x 0.15		mm		
Laser beam diameter, $D$	0.3		mm			Laser beam diameter, $D$	0.3		mm		
Heat transfer coefficient, $h$	8		Wm <sup>-2</sup> K <sup>-1</sup>			Heat transfer coefficient, $h$	8		Wm <sup>-2</sup> K <sup>-1</sup>		
Initial temperature, $T_0$	20		°C			Initial temperature, $T_0$	20		°C		

### 7.4.1 Temperature distribution

The transient temperature was calculated from the edge of the specimen at  $t=0$  s. The temperature distributions on the  $x$ - $z$  plane at  $t=0.02$  s and  $t=0.09$  s for sapphire and silicon wafer are shown in Fig. 7-5 and Fig. 7-6, respectively. It can be seen that for sapphire wafer the higher temperature range is concentrated in the area close to the surface of the specimen. This is because the energy of the CO<sub>2</sub> laser was fully absorbed in the area close to the surface of the material, as illustrated in Fig. 7.3. In contrast, the energy of the Nd:YAG laser was absorbed throughout the thickness of the silicon, resulting in a constant temperature across the thickness of material.

The temperature histories of the laser spot on the sapphire and silicon wafer are summarized in Fig. 7-7. The values refer to the simulated temperature on the surface of the material along the  $x$ -axis. The temperature was increased rapidly at the beginning of the laser-beam irradiation on the sapphire wafer until it reached the maximum temperature of about 350°C and 680°C for laser power of 3 W and 6 W, respectively. The maximum temperature recorded on silicon wafer irradiated with 20 W of laser power was approximately 560°C. Then, the temperature was decreased gradually until it reached the constant temperature. The results of the temperature analysis in this section are used to execute the thermal-stress analysis in the next section.

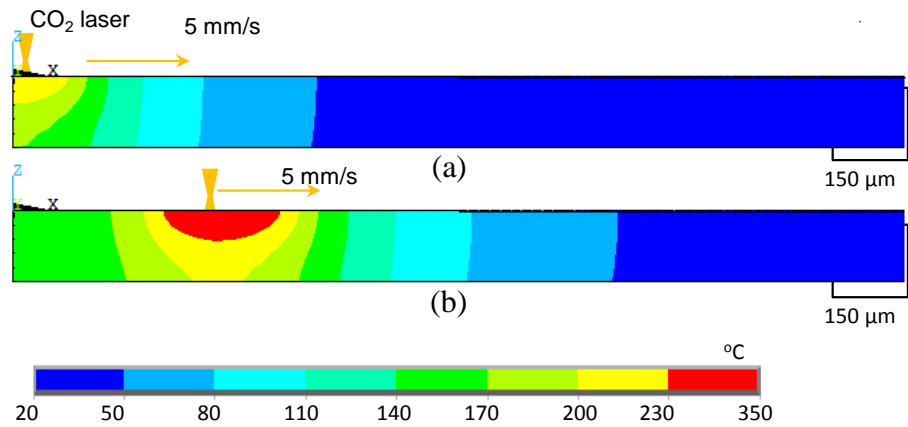


Fig. 7-5 Temperature distribution of sapphire wafer (on  $x$ - $z$  plane,  $P=3$  W): (a)  $t=0.02$  s; (b)  $t=0.09$  s

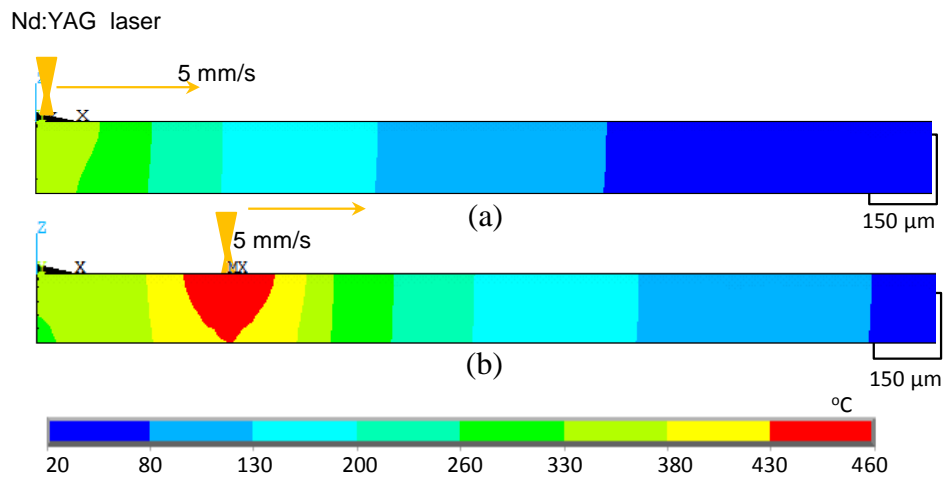


Fig. 7-6 Temperature distribution of silicon wafer (on  $x$ - $z$  plane,  $P=20$  W): (a)  $t=0.02$  s; (b)  $t=0.09$  s

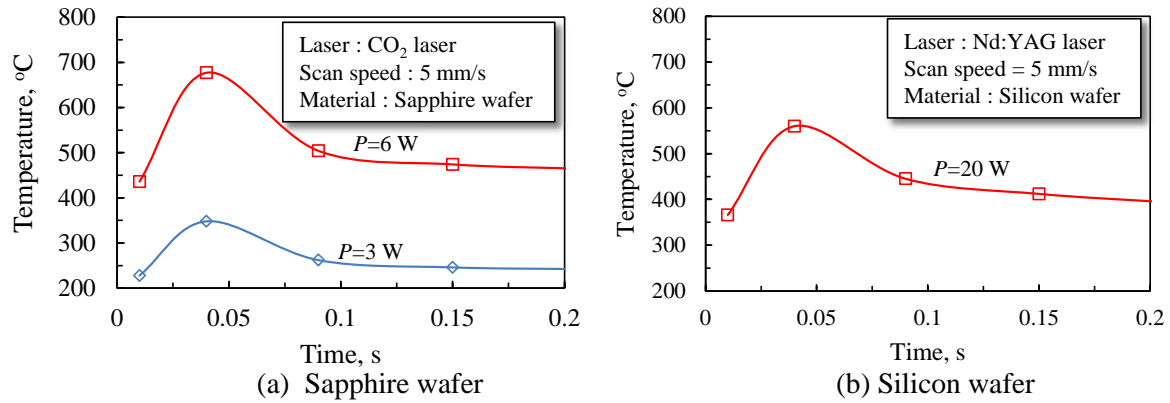


Fig. 7-7 Temperature histories of the laser spot

#### 7.4.2 Thermal-stress distribution

The thermal-stress ( $\sigma_{yy}$ ) distributions on the  $x$ - $z$  plane for sapphire and silicon wafer at  $t=0.02$  s and  $t=0.09$  s are shown in Fig. 7-8 and Fig. 7-9, respectively. Compressive stress was found to be concentrated in the area close to the positions of the laser spot. In the case of sapphire wafer, the compressive stress was larger in the area closest to the irradiating surface. However, the compressive stress was almost uniform across the thickness of the silicon material. This phenomenon occurred due to the laser absorption characteristics of each material. Meanwhile, as the laser beam moved forward in the  $x$ -axis direction, the maximum tensile stress accumulated at the groove tip ( $x=0$ ,  $z=-0.015$  mm) of the specimen.

The relationships between thermal stress ( $\sigma_{yy}$ ) and time for sapphire and silicon materials are summarized in Fig. 7-10 and Fig. 7-11, respectively. The thermal-stress profile was measured at the groove tip ( $z=-0.015$  mm), along the  $x$ -axis. The results show that, at the beginning of laser irradiation, the thermal stress ( $\sigma_{yy}$ ) at the specimen starting edge ( $x=0$ ) was a compressive stress. The thermal stress then changed from compression to tension in a short time when the laser beam moved in the  $x$ -axis direction. As the laser beam moved further,

large tensile stress was accumulated at the groove tip ( $x=0$ ,  $z=-0.015$  mm). This significant tensile stress ( $\sigma_{yy}$ ) may induce a fracture when the stress reaches the fracture strength of the material. The fracture could be induced along the thickness direction ( $z$ -axis) and extended throughout the material. The magnitude of the thermal stress in the sapphire wafer was much bigger than in the silicon wafer. Therefore, fracture would be able to occur at lower laser power.

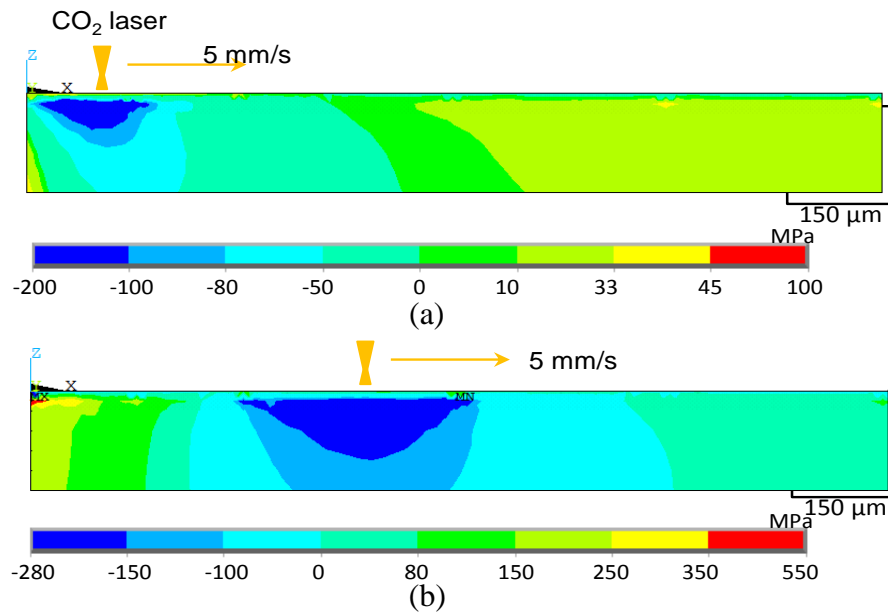


Fig. 7-8 Thermal-stress distribution for sapphire wafer (on  $x$ - $z$  plane): (a)  $t=0.02$  s; (b)  $t=0.09$  s

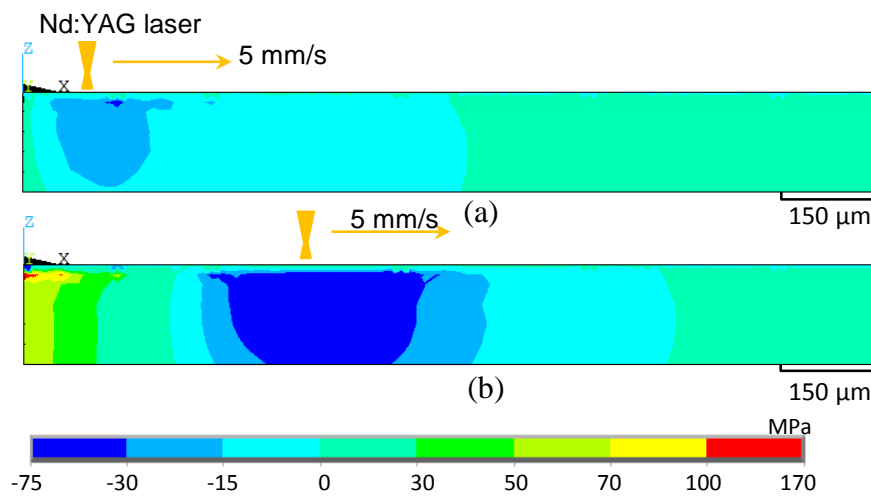


Fig. 7-9 Thermal-stress distribution for silicon wafer (on  $x$ - $z$  plane): (a)  $t=0.02$  s; (b)  $t=0.09$  s

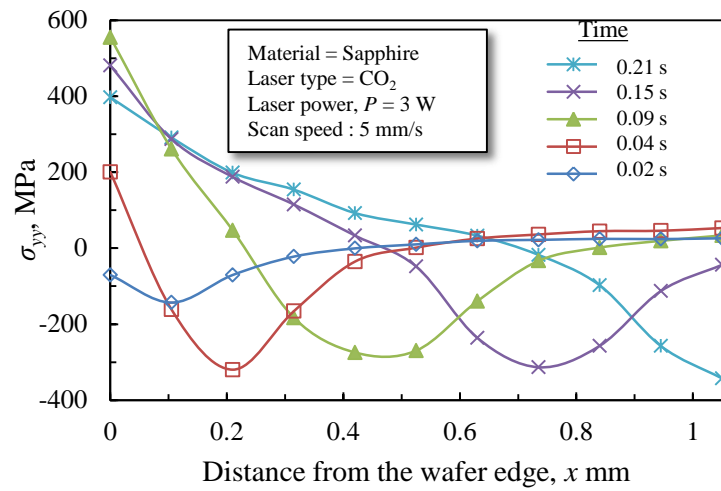


Fig. 7-10 Thermal-stress ( $\sigma_{yy}$ ) distribution of sapphire at various times ( $z=-0.015$  mm)

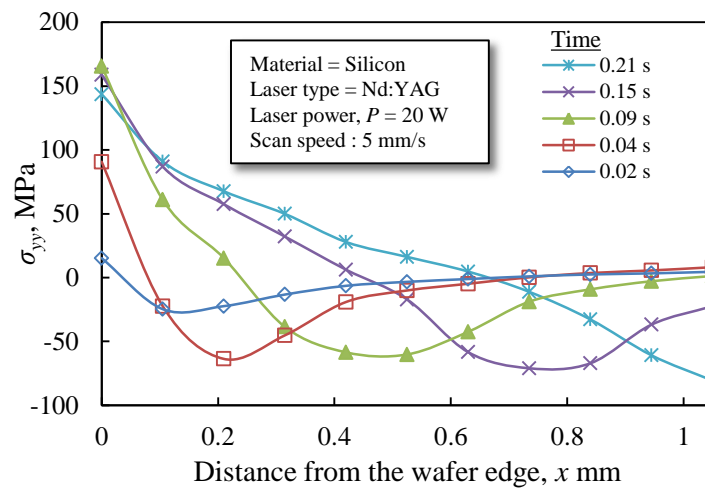


Fig. 7-11 Thermal-stress ( $\sigma_{yy}$ ) distribution of silicon at various times ( $z=-0.015$  mm)

Fig. 7-12 and Fig. 7-13 show the thermal stress ( $\sigma_{yy}$ ) measured along the  $z$ -axis at the edge of the specimen ( $x=0$  mm) for the sapphire and silicon wafer, respectively. From Fig. 7-12, it can be seen that at the beginning of laser irradiation,  $t=0.02$  s, the thermal stress ( $\sigma_{yy}$ ) on the groove tip ( $z=-0.015$  mm) was compressive, and tensile stress resulted on the bottom surface of the specimen ( $z=-0.15$  mm). However, as displayed in Fig. 7-13, the thermal stress ( $\sigma_{yy}$ ) in the silicon wafer at these positions was tensile.

The relationship between maximum thermal stress ( $\sigma_{yy}$ ) and laser irradiation time for sapphire wafer is shown in Fig. 7-14. The results indicate that, at the beginning of irradiation, compressive stress was produced at the positions  $z=-0.015$  and  $z=-0.15$  mm. Greater magnitude of compressive stress was effected at the groove tip ( $z=-0.015$  mm) because the heat from the laser beam was concentrated on the surface area of the specimen. Therefore, higher compressive stress was achieved. As the time increases, the thermal stress at both positions changed from compressive to tensile stress. The stress level was increased rapidly at the groove tip ( $z=-0.015$  mm) compared to the stress on the bottom surface of the specimen. For laser power of  $P=6$  W, the phenomenon of stress conditions was repeated, but with noticeable  $\sigma_{yy}$  value, as shown in Fig. 7-14(b).

Fig. 7-15 shows the relationship between maximum thermal stress ( $\sigma_{yy}$ ) and laser irradiation time for silicon wafer. At  $t=0.02$  s, tensile stresses resulted at positions  $z=-0.015$  and  $z=-0.15$  mm, with a small difference in stress value. As the laser beam moved forward, the tensile stress increased at both positions, with higher stress magnitude concentrated on the groove tip ( $z=-0.015$  mm).

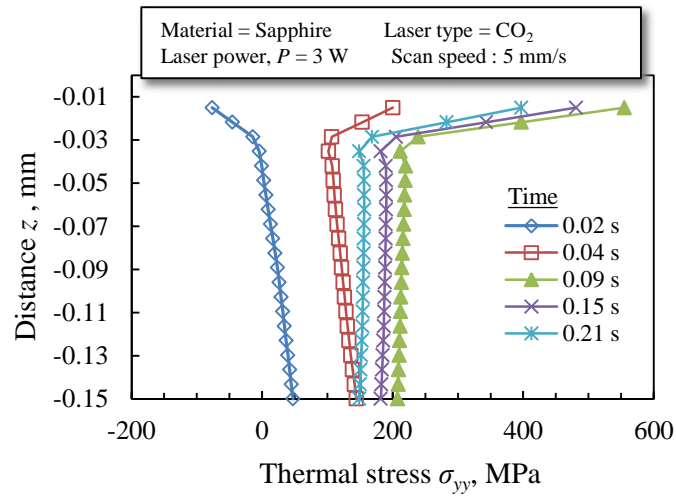


Fig. 7-12 Thermal-stress profile at various times for sapphire (along  $z$ -axis direction,  $x=0$  mm)

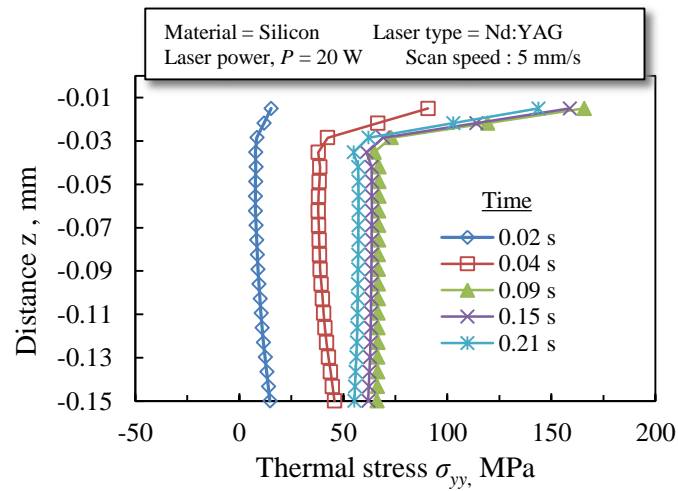


Fig. 7-13 Thermal-stress profile at various times for silicon (along  $z$ -axis direction,  $x=0$  mm)



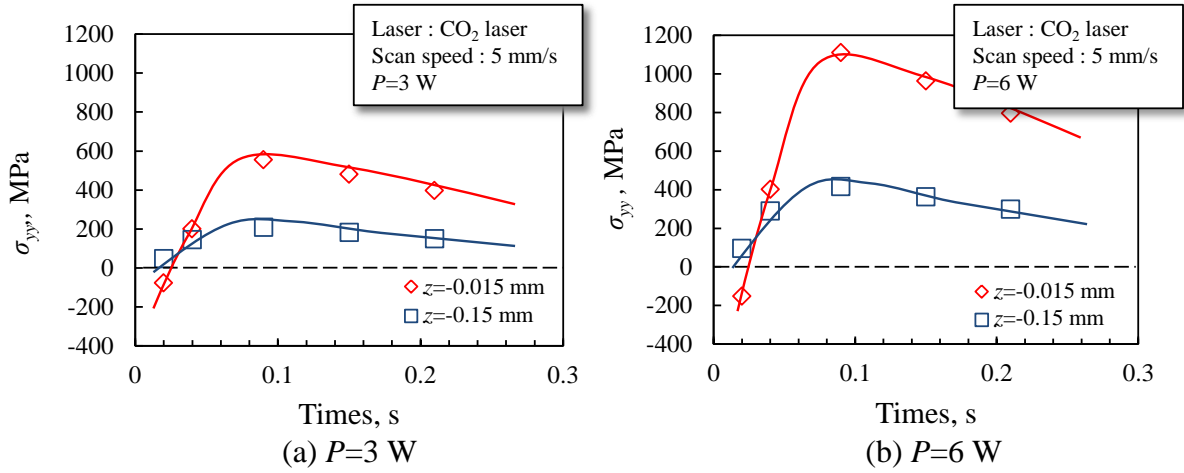


Fig. 7-14 Maximum thermal stress on sapphire wafer ( $x=0$ )

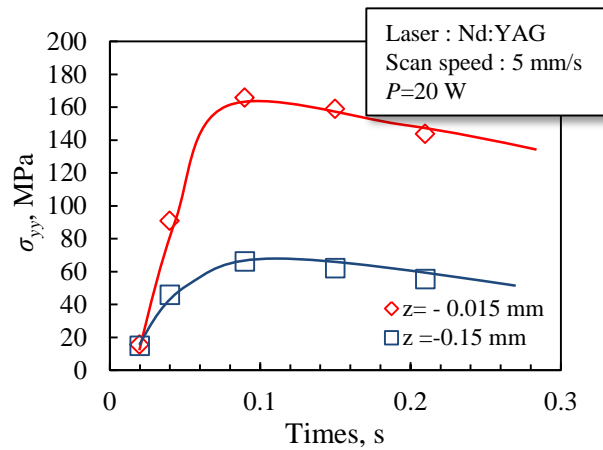


Fig. 7-15 Maximum thermal stress on silicon wafer ( $x=0$ )

### 7.4.3 Stress intensity factor, $K_I$

In this section, the stress intensity factor,  $K_I$ , is used to estimate the stress condition at the positions  $z=-0.015$  and  $z=-0.15$  mm ( $x=0$ ). When  $K_I$  reaches the critical value (fracture toughness), a fracture may occur. Irwin found that the stress field  $\sigma(r, \theta)$  in the vicinity of a groove tip could be described mathematically as in equation 3 [9]. Considering that initial fracture occurs according to opening mode I, and  $\theta=0^\circ$ , the stress intensity factor can be

determined by using equation 4.  $\sigma_{yy}$  is defined as the magnitude of local stress at a distance  $r$  from the groove tip. In this study,  $K_I$  was calculated by considering  $\sigma_{yy}$  at a constant distance,  $r=0.15 \mu\text{m}$ .

$$\sigma_{yy} = \frac{K_I}{\sqrt{2\pi r}} \cos \frac{\theta}{2} \left( 1 - \sin \frac{\theta}{2} \sin \frac{3\theta}{2} \right) \quad \dots (3)$$

$$K_I = \sigma_{yy} \sqrt{2\pi r} \quad \dots (4)$$

Fig. 7-16 illustrates the relationship between the stress intensity factor,  $K_I$ , and laser irradiation time at the two positions  $z=-0.015 \text{ mm}$  and  $z=-0.15 \text{ mm}$  for the sapphire wafer, at laser power of 3 W and 6 W, respectively. For the laser power of 3 W,  $K_I$  at the positions of  $z=-0.15 \text{ mm}$  is high at the beginning, and increases relatively with time. However,  $K_I$  at the groove tip position ( $x=0$ ,  $z=-0.015 \text{ mm}$ ) increases rapidly and reaches the critical stress intensity,  $K_{IC}$  (fracture toughness), first.

However, when the higher laser power of  $P=6 \text{ W}$  was used,  $K_I$  at the position of  $z=-0.15 \text{ mm}$  achieved fracture toughness,  $K_{IC}$ , earlier. This was because the stress magnitude exceeded  $K_{IC}$ . The result indicates that it is possible for the fracture to initiate from a bottom-surface position when higher laser power is used. However, this may lead to a poor separating surface as the fracture cannot be controlled.

The relationship between the stress intensity factor,  $K_I$ , and laser irradiation time at the two positions  $z=-0.015 \text{ mm}$  and  $z=-0.15 \text{ mm}$  for silicon wafer is illustrated in Fig. 7-17. Stress intensity factor,  $K_I$ , increased at these positions in time, where greater increments resulted at the groove tip ( $x=0$ ,  $z=-0.015 \text{ mm}$ ). The results suggest that the fracture may start at the groove tip position ( $x=0$ ,  $z=-0.015 \text{ mm}$ ), as the  $K_{IC}$  of silicon was reached earlier.

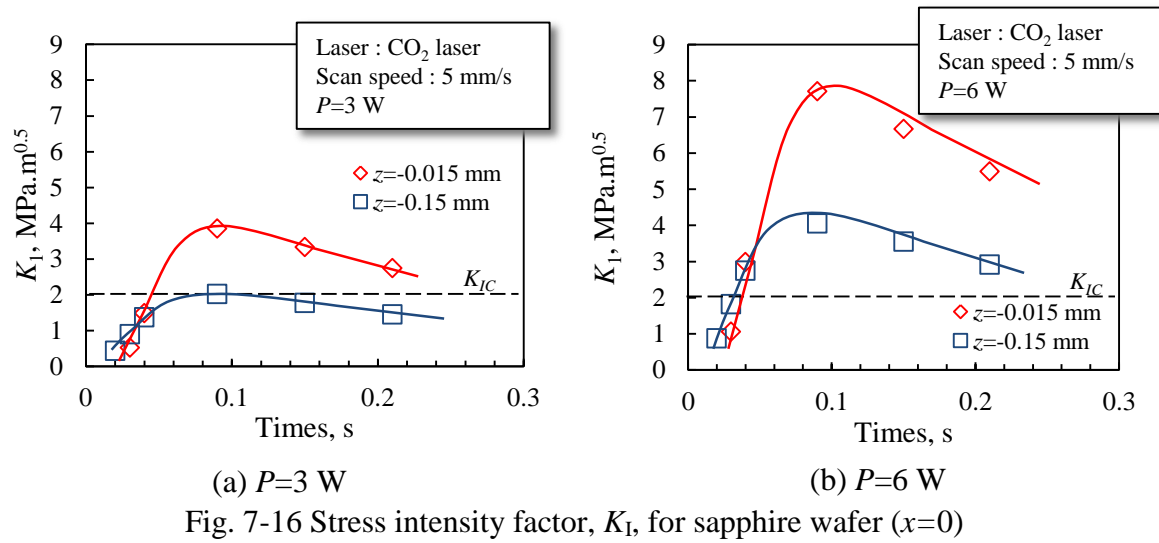


Fig. 7-16 Stress intensity factor,  $K_I$ , for sapphire wafer ( $x=0$ )

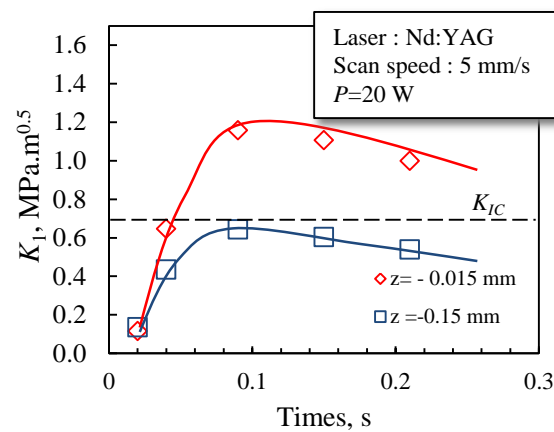


Fig. 7-17 Stress intensity factor,  $K_I$ , for silicon wafer ( $x=0$ )

## 7.5 COMPARISON BETWEEN THE LASER CLEAVING MECHANISMS OF SAPPHIRE AND SILICON WAFER

Based on the FEM analysis results, the mechanisms of laser cleaving on sapphire and silicon wafers can be distinguished clearly. The analysis was performed by considering the use of a CO<sub>2</sub> laser for cleaving the sapphire and an Nd:YAG laser for the silicon wafer. The lasers have different wavelengths, and the absorption of laser energy of these two materials is also different.

As shown in Fig. 7-18, as the laser beam moves along the cutting path on the pre-prepared groove, the tensile stress was accumulated on the edge of the wafer ( $x=0$ ). The critical positions were at the groove tip ( $z=-0.015$  mm) and on the bottom surface ( $z=-0.15$  mm). If the magnitude of the tensile stress is high enough, the fracture will initiate.

As indicated in Fig. 7-8, the laser energy was absorbed on the surface in the case of the sapphire material. In Fig. 7-14, it was shown that at the beginning of laser irradiation compressive stress occurred at the edge ( $x=0$ ) of the sapphire material. Higher magnitude of compressive stress resulted at the groove tip position ( $x=0$ ,  $z=-0.015$  mm) in contrast with the bottom-surface position ( $x=0$ ,  $z=-0.15$  mm). As the laser beam moves forward, the compressive stress changes to the tensile stress. It was found that the thermal stress changed from compression to tension first on the bottom surface ( $x=0$ ,  $z=-0.15$  mm). This is because the groove tip position ( $x=0$ ,  $z=-0.015$  mm) is close to the heat source. Therefore, the compressive condition remains for longer while the laser beam spot moves in the  $x$ -direction.

Fracture initiation will occur if the stress intensity factor,  $K_I$ , of the material reaches the fracture toughness,  $K_{IC}$ . Fig. 7-16 indicated that when higher laser power is used ( $P=6$  W),

$K_I$  on the bottom surface ( $x=0$ ,  $z=-0.15$  mm) reaches the fracture toughness first. Therefore, fracture may initiate at this position.

In the case of silicon wafer, the laser energy was absorbed throughout the thickness of material. This can be seen in Fig. 7-9. As a result, a comparable magnitude of compressive stress occurred at the groove tip ( $x=0$ ,  $z=-0.015$  mm) and on the bottom surface ( $x=0$ ,  $z=-0.15$  mm), as shown in Fig. 7-17. When the laser beam moves forward, the compressive stress at the edge ( $x=0$  mm) of the silicon wafer changes to tensile stress. The stress intensity factor,  $K_I$ , at the groove tip ( $x=0$ ,  $z=-0.015$  mm) achieved the fracture toughness earlier. Therefore, fracture starts at this position.

Based on the analysis results, it is understood that in separating the brittle materials using the laser cleaving process, the laser energy-absorption characteristic has a significant effect in fracture initiation. The laser energy absorption relative to the thickness of the material can be referred to as an absorption coefficient value,  $\beta$ . Higher values of  $\beta$  result in high absorption of laser energy in the area close to the irradiated surface of the material.

When the laser energy is absorbed on the material surface, fracture may start from the bottom surface ( $x=0$ ,  $z=-0.15$  mm). However, if the laser energy is absorbed throughout the material thickness, fracture may be initiated at the groove tip ( $x=0$ ,  $z=-0.015$  mm).

Therefore, the laser energy-absorption characteristic should be considered as a significant factor in deciding groove arrangement on the specimen. For cleaving the sapphire with the CO<sub>2</sub> laser, the groove position should be placed opposite the irradiation surface; the advantages of thermal-stress distribution may thus be exploited.

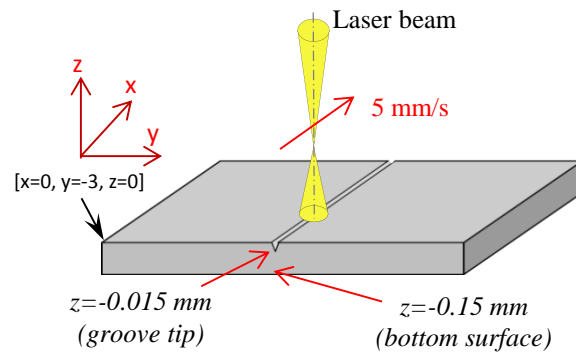


Fig. 7-18 Illustration of laser irradiation with two critical positions during fracture initiation

## 7.6 CONCLUSION

The thermal-stress condition during laser-beam irradiation on sapphire wafer has been investigated by using the finite-element method (FEM). The laser energy absorption of sapphire wafer has been evaluated and applied in assigning heat-source configuration in FEM analysis. The temperature distribution condition was analyzed by thermal transient analysis, and steady-state thermal stress analysis was executed by using the temperature distribution results at a particular point in time. The thermal-stress condition in the sapphire material was estimated and compared with silicon wafer.

Based on the FEM analysis, it can be concluded that energy from the CO<sub>2</sub> laser was absorbed mostly on the surface of the sapphire material. Consequently, the heat was accumulated on the surface of the material during laser-beam irradiation. As a result, a huge temperature gradient was created in the direction of the material's thickness. Thermal stress was generated and tensile stress developed on the bottom surface of the sapphire wafer.

From the stress-intensity-factor analysis, the results clarify that a fracture can start from the bottom surface of the material, instead of from the pre-prepared micro-groove on the irradiation surface. The fracture cannot be controlled and may lead to a poor cleaving surface. Therefore, the orientation of micro-groove on the specimen should be established based on the laser absorption characteristics of the material, so that the advantages of the thermal-stress cleaving technique can be benefited.

## REFERENCES

- [1] T. Okiyama, "Cleavage-Cutting of Brittle Materials by Laser Heating," *Journal of the Japan Society for Precision Engineering*, 60(2), pp. 196-199, 1994. (In Japanese.)
- [2] R. M. Lumley, "Controlled Separation of Brittle Materials Using a Laser," *The American Ceramic Society Bulletin*, 48(9), pp. 850-854, 1969.
- [3] Y. Imai, H. Morita, T. Takase, H. Koga, "Possibility of Employing Thermal Stresses as a Cutting Device for Brittle Materials," *Transaction of the Japan Society of Mechanical Engineers*, 55(509), pp. 147-151, 1989.
- [4] T. Kurobe, K. Ichikawa, H. Nagai, "Breaking of Silicon Wafer by Irradiation of YAG Laser," *Journal of the Society of Materials Science*, 44(497), pp. 159-163, 1995. (In Japanese.)
- [5] T. Ueda, K. Yamada, K. Oiso, A. Hosokawa, "Thermal Stress Cleaving of Brittle Materials by Laser Beam," *CIRP Annals - Manufacturing Technology*, 51(1), pp. 149-152, 2002.
- [6] T. Ueda, T. Mino, T. Furumoto, A. Hosokawa, S. Nagatomo, "Laser cleaving of sapphire wafer with pulsed wafer," *Journal of the Japan Society of Grinding Engineers*, 55(7), pp. 424-426, 2011. (In Japanese.)
- [7] D. Triantafyllidis, J. R. Bernstein, L. Li, and F. H. Stott, "Dual laser beam modification of high alumina ceramic," *Journal of Laser Applications*, 15(1), pp. 49-54, 2003.

## CHAPTER 8 : CONCLUSIONS

Thermal-stress cleaving by laser-beam irradiation is a prospective technique for separating thin substrates from brittle materials such as silicon and sapphire. The process utilizes a temperature differential within the substrate by providing energy via the laser beam, causing a hot area to expand, developing a stress force leading to fracture. The process offers significant advantages over other methods: the contamination of coolant and chips can be eliminated, tool wear does not occur, and machining kerf can be avoided. As it is a non-contact process it is also possible to fix the work piece on the machining table using a simple method. Moreover, the method has the capability to produce an extremely smooth surface, as compared to the poor surface finish and large material deformation caused by conventional mechanical cutting.

To exploit these advantages, the mechanism of thermal-stress cleaving by a laser beam needs to be fully understood. On this basis, the present study of the laser cleaving mechanism of brittle materials such as silicon and sapphire was carried out using experimental and computational analysis. The influences of laser power, temperature and initial groove parameters on fracture initiation, crack propagation and separating-surface features were established by using an experimental approach, and the thermal-stress situation during the irradiation process was clarified by finite-element-method (FEM) analysis.

The material separation in the laser cleaving process is similar to crack extension. However, the process requires an initial groove to facilitate and control the fracture during



laser-beam irradiation. Hence, a new method of preparing an initial groove was proposed to eliminate the problems of micro-cracks, secondary cracks and processing inaccuracy. In this research, silicon and sapphire were used as materials for investigation using an Nd:YAG and a CO<sub>2</sub> laser, respectively. The thermal-stress condition during laser-beam irradiation is dependent on the laser energy absorption in the material. The energy absorption is related to the laser wavelength and type of material used. Therefore, the influence of the laser absorption characteristic on the thermal-stress distribution was also evaluated by FEM analysis. Based on the research, the following conclusions can be made in relation to the respective chapters.

In Chapter 2, the application of lasers in material cutting was described briefly. The current methods used in separating wafer material were compared with thermal-stress cleaving by a laser beam. The problems with current approaches were discussed in detail, and the advantages of laser cleaving of wafer material were emphasized. The chapter also explained the principle of thermal-stress cleaving.

In Chapter 3, the fabrication of a micro-groove by using a cylindrical micro-lens was reported. The micro-lens was developed by applying the heat supplied by the laser beam on the acrylic material; the heated part of the material then expanded and was transformed into a rubber-like state before solidifying to a stable curved-lens shape. The micro-groove was successfully produced by a material-removal process via melting and vaporizing due to the high energy density on the specimen surface. The processing of the micro-groove was mainly influenced by two parameters: the laser power, and the irradiation pulse number. The width of the micro-groove increased with increases in laser power, while the depth increased with increased laser irradiation pulse. These results were essential in preparing the micro-groove on the specimens for the experiments in the next chapters.

In Chapter 4, the two-color-pyrometer system and its fundamental principles were introduced. In this pyrometer, infrared rays emitted from the object are accepted and transmitted to the detectors by using an optical fiber. The detector consists of InSb and MCT components, mounted in a sandwich configuration. Temperatures are obtained by calculating the ratio of the output voltage from these detectors. The calibration curve showed that the two-color pyrometer has a good degree of accuracy in measuring temperature.

In Chapter 5, an investigation of thermal-stress cleaving was performed using a single-point laser. A silicon wafer with different types of initial crack was evaluated in terms of separating performance by observing the temperature at the time of separation, i.e., cleaving temperature and cleaving time. The temperature of the laser spot was measured by using a two-color pyrometer with an optical fiber, and the AE signal was assessed to observe the time taken for fracture. The finite-element method (FEM) computational analysis was used to investigate the thermal-stress condition inside the wafer. The separating performance of the silicon wafer was analyzed on the basis of micro-groove and micro-crack. Both methods were able to initiate the fracture for cleaving execution. Fracture occurred when the temperature of the laser irradiation spot was higher than the critical temperature. Higher tensile stress was concentrated on the sharper crack tip; therefore, specimens with micro-cracks have a strong tendency towards fracture initiation. From the FEM analysis, the results explained the specimens' response to the heat supplied by the laser beam. Thermal stress generated by the laser beam caused tensile stress which accumulated in the area of the micro-groove. By using the thermal-stress distribution results, the position of fracture initiation was investigated.

In Chapter 6, the separating mechanism of a silicon wafer with moving laser beam using the thermal-stress cleaving method was examined experimentally and computationally.

The micro-groove was prepared at the leading edge of the silicon wafer specimen. The temperature of the moving laser spot was measured by using a two-color pyrometer with an optical fiber, and the AE signal was assessed to observe the mechanism of propagations. The effect of laser energy on the cleaving mechanism was analyzed, and the influence of the parameters of groove length and depth were studied. The cleaved surface was observed using a scanning electron microscope (SEM). In order to explain the thermal-stress distribution, the finite-element method (FEM) software ANSYS was applied by considering the temperature ascertained from the experimental result. The fracture toughness of the silicon wafer was also measured, and the stress intensity factor of the material was analyzed. The separating process of the silicon wafer occurred in two stages: the fracture initiation, where the fracture occurs due to tensile stress concentrated at the groove tip on the edge of the specimen, and intermittent crack propagation, which occurs at constant intervals in time. Temperature at the laser irradiation area was related to the separating characteristics of a silicon wafer by the cleaving technique. The temperature influenced cleaving achievement and cleaving-surface quality. Fracture initiation and crack propagation produced cleaving mark waves on the separating surface. The cleaving mark wave was consistent with the AE signals. The finite-element method (FEM) analysis results explained the stress distribution during laser irradiation. By using FEM, the stress condition was determined quantitatively by identifying the stress intensity factor,  $K_I$ . Fracture toughness,  $K_{IC}$ , of the material was determined experimentally using the Vickers indentation technique.

In Chapter 7, the finite-element method (FEM) was used to analyze the thermal-stress conditions during laser-beam irradiation on a sapphire wafer using a CO<sub>2</sub> laser. The thermal-stress distribution during laser-beam irradiation was different to that shown by the silicon wafer irradiated with the Nd:YAG laser; this was due to variation in material properties and absorption characteristics. The energy from the CO<sub>2</sub> laser was absorbed mostly on the surface

of the sapphire material and a large temperature gradient was created in the material thickness direction. As a result, thermal stress was generated, and tensile stress developed on the bottom surface of the sapphire wafer. The results from the stress-intensity-factor ( $K_I$ ) analysis showed that it is possible to start a fracture from the bottom surface of the material, instead of from the pre-prepared micro-groove on the irradiation surface. However, the fracture cannot be controlled and leads to a poor cleaving-surface result. Therefore, the orientation of the micro-groove on the specimen should be considered based on laser absorption characteristics in order to profit from the advantages of the thermal-stress cleaving technique.

## LIST OF PUBLICATIONS

1. Alias Mohd Saman, Tatsuaki Furumoto, Akira Hosokawa and Takashi Ueda, “Thermal Stress Cleaving of Si-Wafer: Investigation of Fracture Initiation during Laser Beam Irradiation”, *Advanced Material Research*, Vol.1101, pp. 412-418, 2015.
2. Alias Mohd Saman, Tatsuaki Furumoto, Takashi Ueda and Akira Hosokawa, “A Study on Separating of a Silicon Wafer with Moving Laser Beam by Using Thermal Stress Cleaving Technique”, *Journal of Materials Processing Technology*, Submitted July 2014 (Under review), 25 pages.
3. Alias Mohd Saman, Takashi Ueda, Kazuto Fujisawa, Tatsuaki Furumoto, Akira Hosokawa and Tomohiro Koyano, “Temperature and Acoustic Emission Monitoring in Thermal Stress Cleaving Process”, *Japan Society of Mechanical Engineer(JSME) 51<sup>st</sup> General Assembly and Conference, Hokuriku Shin-Etsu, Japan*, No.509, 2014.

## **ACKNOWLEDGEMENTS**

I would like to express my special appreciation and thanks to my advisor, Assoc. Prof. Tatsuaki Furumoto, for the guidance, encouragement and advice he has provided throughout my research. I also would like to express my gratitude to my co-advisors, Prof. Takashi Ueda and Prof. Akira Hosokawa for their deep involvement in the research. I would also like to thank my committee members, Prof. Ryoichi Monzen and Prof. Naoki Asakawa for their guidance, help and insightful comments. Thank are also due to Dr. Tomohiro Koyano and all the members of Manufacturing System Laboratory for their advices and immense help during the experimental works.

I would like to express my deepest appreciation to all of my family members, especially to my wife, Nor Azlinah Md Lazam and my son for the unconditional love, patience and support throughout this work. Appreciation and gratitude are extending to Malaysian students in Kanazawa and all friends for their friendship and hospitality.

It is an honor for me to acknowledge the scholarships from Malaysian Government through Ministry of Education, Malaysia and Universiti Teknologi MARA (UiTM) for their financial support during my studies at Kanazawa University.